UNIVERSIDAD POLITECNICA DE VALENCIA

DEPARTAMENTO DE COMUNICACIONES

Doctorado Telecomunicación

# Beam Position Monitoring in the CLIC Drive Beam Decelerator Using Stripline Technology


*Author:* Alfonso Benot Morell

*Directors:* Dr. Angeles Faus Golfe
Dr. Vicente Enrique Boria Esbert



*Submission:* June 2015



*Institutions:* European Organization for Nuclear Research (CERN)
Instituto de Física Corpuscular (IFIC)

# Acknowledgements

I would like to start by expressing my gratitude for the opportunity to carry out this research to my IFIC supervisor, Dr. Angeles Faus Golfe, my CERN supervisors, Lars Søby and Manfred Wendt and to my UPV supervisor, Dr. Vicente Enrique Boria Esbert. Without their constant guidance and support, this work would not have been possible.

It is also my wish to extend this gratitude to my colleagues of the CERN Beam Instrumentation Group, the IFIC Particle Accelerator Group and the CLIC collaboration. It is a pleasure and a very enriching experience to work with all of them.

# Contents

# Abstract

CLIC, a Compact electron-positron LInear Collider proposed for the study of High-Energy Physics (HEP) in the TeV energy scale, is based on a two-beam scheme. Radio-Frequency (RF) power, required to accelerate a high energy luminosity beam is extracted from a high current Drive Beam (DB), whose decelerator requires more than 40000 quadrupoles, each holding a BPM. These BPMs face several challenges, as they will be operated in close proximity to the Power Extraction and Transfer Structures (PETS), emitting 130 MW RF power at 12 GHz. The accuracy and resolution requirements are also demanding (20 $\mu$m and 2 $\mu$m, respectively). They have to be compact, inexpensive and operate below the waveguide (WG) cut-off frequency of the beam pipe to ensure locality of the position signals, which rules out the signal processing at the 12 GHz bunch frequency. Also wake-fields, and hence the longitudinal impedance, must be kept low.

The first proposed solution is a compact, conventional stripline BPM , developed at CERN in collaboration with SLAC, LAPP and IFIC, utilizing a signal processing scheme operating below 40 MHz. This thesis focuses on the electromagnetic and mechanical design of the compact stripline BPM, the design of the electronic acquisition system, the laboratory characterization tests of the complete system and its resolution and linearity tests with beam currents of up to 22 A, corresponding to PETS RF interference of up to 60 MW power, in the Test Beam Line (TBL) of the CLIC Test Facility 3 (CTF3). The results of both laboratory and beam tests are discussed and several modifications and guidelines are provided for further stripline BPM designs.

# Summary

The Compact Linear Collider (CLIC) is an electron-positron collider conceived for the study of High-Energy Physics in the TeV center of mass energy region, is based on a two-beam operation principle: instead of using active elements (klystrons), the necessary RF power to accelerate the Main Beam (MB) is obtained from the deceleration of a high-current, moderate energy Drive Beam (DB) in the so-called Power Extraction and Transfer Structures (PETS). These structures emit an RF signal of about 130 MW power at 12 GHz. As this frequency is above the cut-off frequency of the fundamental mode for the specified beam vacuum pipe dimensions (7.6 GHz), the inference propagates from the PETS to the neighboring devices, including the Beam Position Monitors (BPM).

According to the CLIC Conceptual Design Report (CDR), an efficient beam position monitoring system for the CLIC DB decelerator needs to meet the following requirements:

- It should be as simple and economic as possible, as 41580 units are required, amounting to 75% of all CLIC BPMs.
- The signal processing scheme should not be affected by the PETS interferece. This rules out processing the signals at the beam bunching frequency (12 GHz in this case).
- The resulting position signal should detect changes in the beam position whose duration is 10 ns or longer (time resolution)
- The required spatial resolution is 2 $\mu$m for a 23 mm diameter vacuum pipe.
- Wide dynamic range: the electronic acquisition system must be able to process signals with extreme levels, induced by either very high (100 A) or very low (3 A) current beams.

This PhD thesis describes the electromagnetic and mechanical design of the first prototype BPM developed for the CLIC Drive Beam and its characterization tests in laboratory and with beam. The first two chapters introduce the CLIC project and review the state-of-the-art beam position monitoring techniques.

Chapter 3 presents the design of the BPM. The stripline technology has been selected, as it is the only one among the most commonly used BPM techniques to present a suitable frequency response to filter out the RF interference caused by the PETS. Choosing an appropriate length for the electrodes, it is possible to tune one the periodic notches in the stripline frequency response to 12 GHz. The influence of different electromagnetic and geometrical aspects is also studied, such as beam coupling impedance or the ratio between longitudinal and transverse dimensions.

The design of the electronic acquisition system is presented in Chapter 4, considering the project requirements in terms of resolution (2 $\mu$m), accuracy (20 $\mu$m) and time resolution (10 ns). Due to the high amount of units required, the number of electronics components has been minimized. As the designed signal processing scheme is based on charge integration, it can be adapted to different stripline pick-ups by simply modifying the attenuator settings according to the required output signal levels.

The laboratory characterization tests of the prototype stripline BPM, in the low and the high frequency ranges, performed with a thin wire and a coaxial waveguide, respectively, are described in Chapter 5. The measurement results are compared with the theoretical estimation and the electromagnetic field simulation results. In addition, the high-frequency test reveals that the first prototype stripline BPM does not provide sufficient suppression of the 12 GHz PETS RF interference. An additional study proposed several modifications and guidelines to be followed in the design of a second prototype stripline BPM.

Finally, Chapter 6 presents the installation of the prototype stripline BPM at the CLIC Test Facility 3 (CTF3) in the Test Beam Line (TBL), a scaled version, in dimensions and current, of the CLIC Drive Beam decelerator. Two types of tests were performed: linearity/sensivity and resolution. A comparison is made between the measured parameters with beam and the ones obtained in the laboratory characterization tests. A Singular Value Decomposition analysis (SVD) has also been performed on the beam data, in order to estimate an upper boundary of the spatial resolution of the prototype.

# Resumen

El Colisionador Lineal Compacto (Compact Linear Collider, CLIC), un colisionador de electrones y positrones concebido para el estudio de la Física de Altas Energías en la región de los TeV de energía de centro de masas, se basa en un principio de funcionamiento de doble haz: en lugar de emplear elementos activos (klystrons) para proporcionar la potencia RF requerida para acelerar el haz principal (Main Beam, MB), ésta se obtiene de la deceleración de un haz secundario (Drive Beam, DB), de alta corriente y energía moderada, en las llamadas estructuras de extracción y transferencia de potencia (Power Extraction and Transfer Structures, PETS). Estas estructuras emiten una señal RF de más de 130 MW de potencia a 12 GHz, que, por estar localizada en una frecuencia superior a la de corte del modo fundamental en el tubo de vacío del haz (7.6 GHz), se propaga por éste hacia los dispositivos adyacentes, entre los cuales se encuentran los sistemas de monitorización de la posición (Beam Position Monitor, BPM).

De acuerdo con el informe conceptual de diseño de CLIC (Conceptual Design Report, CDR), un sistema eficiente de monitorización de la posición del haz en el decelerador del haz secundario deberá cumplir los siguientes requisitos:

- Debe ser lo más sencillo y económico posible, ya que se precisan 41580 unidades: el 75% de todos los BPMs de CLIC.
- El procesado de señal en el sistema de adquisición deberá ser inmune a la interferencia generada en las PETS. Esto excluye la solución habitual de procesar las señales del BPM a la frecuencia de pulsado del haz (12 GHz en este caso).
- La señal de posición resultante del procesado debe ser capaz de detectar cambios en la posición del haz de duración igual o mayor a 10 ns (resolución temporal).
- La resolución espacial requerida es de 2 $\mu$m para un tubo de vacío de 23 mm de diámetro.
- Amplio rango dinámico: el sistema electrónico de adquisición del BPM debe poder procesar señales cuyos niveles serán extremos, inducidas por haces de muy alta (100 A) y muy baja (3 A) corriente.

Esta tesis doctoral describe el diseño electromagnético y mecánico y los tests de caracterización en laboratorio y con haz del primer prototipo de BPM desarrollado para el decelerador del haz secundario del CLIC. En los dos primeros capítulos se realiza una introducción al CLIC y una revisión del estado del arte en la monitorización de la posición de haz.

El capítulo 3 presenta el diseño del BPM. Se ha optado por la tecnología *stripline*, ya que, entre las tecnologías habituales de monitorización de la posición, es la única que

presenta una respuesta en frecuencia capaz de filtrar la interferencia procedente de las PETS. Eligiendo una longitud apropiada para sus electrodos, es posible sintonizar uno de los ceros periódicos de la respuesta en frecuencia *stripline* a 12 GHz. Se estudia también la influencia de diferentes aspectos eléctromagnéticos y geométricos en el diseño, como la adaptación de la impedancia de acoplamiento del haz o la relación entre las dimensiones longitudinales y transversales del dispositivo.

Posteriormente se describe, en el capítulo 4, el diseño de un sistema electrónico de adquisición teniendo en cuenta los requisitos del proyecto en términos de resolución (2 $\mu$m), precisión/exactitud (20 $\mu$m) y resolución temporal (10 ns). Debido a la alta cantidad de unidades que se precisa, el número de componentes electrónicos se ha minimizado. Como el esquema de procesamiento de señal adoptado se basa sólo en la integración de la carga presente en la señal de entrada, es posible reutilizarlo en otros BPM *stripline* modificando la configuración del atenuador de acuerdo con los niveles de salida necesarios.

Los tests de caracterización en laboratorio del prototipo *stripline* BPM, a baja y a alta frecuencia, realizados con un cable fino y una guía de ondas coaxial, respectivamente, se detallan en el capítulo 5, comparando los resultados medidos con la estimación teórica y con los resultados obtenidos mediante simulación del campo electromagnético. Además, se comprueba en el test de alta frecuencia que este primer diseño no cumple los requisitos de filtrado de la interferencia emitida por las PETS a 12 GHz, realizándose un estudio que propone las modificaciones necesarias a realizar en un segundo prototipo *stripline*.

Finalmente, en el capítulo 6 se presenta el emplazamiento seleccionado para instalar el prototipo *stripline* BPM en la instalación de pruebas de CLIC (CLIC Test Facility, CTF3) en la línea de test con haz (Test Beam Line, TBL), una versión a escala, tanto en dimensiones como en corriente, del decelerador del haz secundario. Se han llevado a cabo dos tipos de tests: linealidad/sensibilidad y resolución, comparándose los resultados de linealidad/sensibilidad con los obtenidos en los tests de caracterización en el laboratorio. Se ha realizado también un análisis de datos por descomposición de valores singulares (Singular Value Decomposition, SVD) para estimar una cota superior de la resolución espacial del prototipo.

# Resum

El Col·lisionador Lineal Compacte (Compact Linear Collider, CLIC), un col·lisionador d'electrons i positrons concebut per l'estudi de la Física d'Altes Energies a la regió dels TeV (energía del centre de massa), es basa en un principi de funcionament de doble feix: en lloc de fer servir elements actius (klystrons) per proporcionar la potència RF requerida per accelerar el feix principal (Main Beam, MB), aquesta s'obtè de la desacceleració d'un feix secundari (Drive Beam, DB), d'alt corrent i energia moderada, a les anomenades estructures d'extracció i transferència de potència (Power Extraction and Transfer Structures, PETS). Aquestes estructures emeten una senyal interferent RF de més de 130 MW de potència a 12 GHz, que, pel fet d'estar localitzada a una freqüència superior a la de tall del mode fonamental al tub de buit del feix (7.6 GHz), es propaga a través d'aquest fins els dispositius adjacents, entre els quals trobem els sistemes de monitorització de la posició (Beam Position Monitor, BPM).

D'acord amb l'informe conceptual de disseny de CLIC (Conceptual Design Report, CDR), un sistema eficient de monitorització de la posició del feix al desaccelerador del feix secundari haurà de complir els següents requisits:

- Ha de ser el més senzill i econòmic possible, ja que es necessiten 41580 unitats: el 75% de tots els BPMs de CLIC.
- El processat de la senyal al sistema d'adquisició haurà de ser inmune a la interferència generada als PETS. Això exclou la solució habitual de processar les senyals del BPM a la freqüència de pulsacions del feix (12 GHz en aquest cas).
- La senyal de posició resultant del processat ha de ser capaç de detectar canvis a la posició del feix de durada igual o més gran que 10 ns (resolució temporal).
- La resolució espaial necessària és de 2 $\mu$m per a un tub de buit de 23 mm de diàmetre.
- Ampli rang dinàmic: el sistema electrònic d'adquisició del BPM ha de poder processar senyals amb nivells extrems, induïdes per feixos de molt alt (100 A) i molt baix (3 A) corrent.

Aquesta tesi doctoral descriu el disseny electromagnètic i mecànic i els tests de caracterització al laboratori i amb feix del primer prototip de BPM desenvolupat per al desaccelerador del feix secundari de CLIC. Als dos primers capítols es realitza una introducció a CLIC i una revisió de l'estat de l'art a la monitorització de la posició del feix.

El capítol 3 presenta el disseny del BPM. S'ha optat per la tecnologia *stripline*, ja que, entre les tecnologies habituals de monitorització de la posició, és la única que presenta una resposta en freqüència capaç de filtrar la interferència procedent de les PETS.

Escollint una longitud apropiada per als seus electrodes, és possible sintonitzar un dels zeros periòdics de la resposta en freqüència *stripline* a 12 GHz. S'estudia també la influència de diferents aspectes electromagnètics i geomètrics al disseny, com l'adaptació de la impedància d'acoblament del feix o la relació entre les dimensions longitudinals i transversals del dispositiu.

Posteriorment es descriu, al capítol 4, el disseny d'un sistema electrònic d'adquisició tenint en compte els requisits del projecte en termes de resolució (2 $\mu$m), precisió/exactitut (20 $\mu$m) i resolució temporal (10 ns). Degut a la gran quantitat d'unitats que es necessiten, el nombre de components electrònics s'ha minimitzat. Com l'esquema de processament de senyal adoptat es basa només en la integració de la càrrega present a la senyal d'entrada, és possible reutilitzar-ho en d'altres BPM *stripline* modificant la configuració de l'atenuador d'acord amb els nivells de sortida necessaris.

Els tests de caracterització al laboratori del prototip *stripline* BPM, a baixa i altra freqüència, realitzats amb un cable prim i una guia d'ones coaxial, respectivament, s'expliquen amb detall al capítol 5, comparant els resultats mesurats amb l'estimació teòrica i amb els resultats obtinguts mitjançant simulació del camp electromagnètic. A més, es comprova al test d'alta freqüència que aquest primer disseny no cumpleix els requisits de filtrat de la interferència emessa pels PETS a 12 GHz, realitzant-se un estudi que proposa les modificacions necessàries a realitzar en un segon prototip *stripline*.

Finalment, al capítol 6 es presenta l'emplaçament seleccionat per instal·lar el prototip *stripline* BPM a la instal·lació de proves de CLIC (CLIC Test Facility, CTF3) a la línea de test amb feix (Test Beam Line, TBL), una versió feta a escal·la, tant en dimensions com en corrent, del desaccelerador del feix secundari. S'han portat a terme dos tipus de tests: linealitat/sensibilitat i resolució, comparant els resultats de linealitat/sensibilitat amb els obtinguts als tests de caracterització al laboratori. S'ha realitzat també un anàlisi de dades per descomposició de valors singulars (Singular Value Decomposition, SVD) per estimar una cota superior de la resolució espaial del prototip.

# List of Acronyms

**ADC** Analog-to-Digital Converter

**ATF** Accelerator Test Facility

**BBU** Beam Break-Up

**BCD** Baseline Configuration Document

**BDS** Beam Delivery Section

**BPM** Beam Position Monitor

**BPR** Beam Profile Radio-frequency monitor

**CDR** Conceptual Design Report

**CERN** European Organization for Nuclear Research

**CESR** Cornell Electron-positron Storage Ring

**CesrTA** CESR Test Accelerator

**CF** ConFlat flange

**CLEX** CLIC Experimental Area

**CLIC** Compact Linear Collider

**CR** Combiner Ring

**CTF3** CLIC Test Facility 3

**DB** Drive Beam

**DC** Direct Current

**DESY** Deutsches Elektronen-SYnchrotron

**DL** Delay Loop

**DR** Damping Ring

**DUT** Device Under Test

**EM** Electro-Magnetic

**ENOB** Effective Number Of Bits

**EOS** Electrical OffSet

**FEL** Free-Electron Laser

**FFT** Fast Fourier Transform

**FIFO** First In, First Out

**FLASH** Free-electron LASer Hamburg

**FLCs** Future Linear Colliders

**FODO** Focusing-Defocusing quadrupole cell

**FPGA** Field-Programmable Gate Array

**GBT** GigaBit Transceiver

**GDE** Global Design Effort

**HOMs** High-Order Modes

**HP** High-Pass filter

**HP** High extracted PETS power test configuration

**HSMC** High Speed Mezzanine Card

**ICFA** International Committee for Future Accelerators

**IFIC** Instituto de Física Corpuscular

**ILC** International Linear Collider

**IP** Interaction Point

**ITRP** International Technology Recommendation Panel

**KEK** High-Energy Accelerator Research Organization

**LAPP** Laboratoire d'Annecy-le-Vieux de Physique des Particules

**LEP** Large Electron-positron Collider

**LHC** Large Hadron Collider

**LNA** Low Noise Amplifier

**LVDS** Low Voltage Differential Signaling

**MB** Main Beam

**OTR** Optical Transition Radiation

**PCIex** Peripheral Component Interconnect Express

**PETS** Power Extraction and Transfer Structures

**PIC** Particle-In-Cell solver

**PU** Pick-Up

**RDR** Reference Design Report

**RF** Radio Frequency

**SCRF** SuperConducting Radio Frequency

**SER-DES** Serialization and Deserialization

**SiC** Silicon Carbide

**SINAD** SIgnal to Noise and Distortion Ratio

**SLAC** Stanford Linear Accelerator Center

**SMA** SubMiniature Version A

**SNR** Signal to Noise Ratio

**SVD** Single Value Decomposition

**TBL** Test Beam Line

**TBM** Two-Beam Module

**TBTS** Two-Beam Test Stand

**TDR** Technical Design Report

**TDR** Time Domain Reflectometry

**TEM** Transverse Electro-Magnetic

**TM** Transverse Magnetic

**UPV** Universidad Politécnica de Valencia

**VNA** Vector Network Analyzer

**WCM** Wall Current Monitor

**XFEL** European X-Ray Free-Electron Laser

# Chapter 1

# Introduction

The field of Particle Physics has made impressive progress in the pursuit of its core mission, elucidating the laws of nature at the most fundamental level. A giant leap, the discovery of the Higgs boson, has been accompanied by many experimental results confirming the Standard Model beyond the previously explored energy scales. These results raise further questions on the origin of elementary particle masses and on the role of the Higgs boson in the more fundamental theory underlying the Standard Model, which may involve additional particles to be discovered around the TeV scale.

The discovery of the Higgs boson is the start of a major programme of work to measure this particle's properties with the highest possible precision for testing the validity of the Standard Model and to search for further new physics at the energy frontier, addressing key open questions ranging from the mechanism of electroweak symmetry breaking to the discovery of possible new symmetries, deeper understanding of Dark Matter and further possible phenomena beyond the Standard Model. The Large Hadron Collider (LHC) is in a unique position to pursue these objectives. The exploitation of the full potential of the LHC, including the high-luminosity upgrade of the machine and detectors, with a view to collecting ten times more data than in the initial design, by around 2030, is one of the highest priorities.

However, due to the large background present at hadron collisions, which impairs the detection of numerous events, a consensus has been reached in the particle physics community, supported by the International Committee for Future Accelerators (ICFA), that it is necessary to complement the results of the LHC with those of a lepton collider in the TeV energy range.

The highest energy lepton collisions so far, 209 GeV, have been achieved with electron-positron ($e^-e^+$) colliding beams in the Large Electron-Positron collider (LEP) at CERN. At this energy, the synchrotron radiation losses, inherent to circular accelerators, were already significant, amounting to 3% of the beam energy for a 27 km-long circumference, yet compensable by a powerful superconducting Radio-Frequency (RF) system providing up to 3640 MV per turn. Since synchrotron radiation losses are inversely proportional to the bending radius and to the fourth power of the particle mass, the RF power needed to compensate them in an $e^-e^+$ circular collider working in the Terascale would make this option infeasible.

An alternative in order to build a Terascale lepton collider would be to avoid the bending of particle trajectories by using $e^-e^+$ linear colliders where two opposing linear

accelerators (*linacs*) accelerate the particles to their final energy in one pass before focusing and colliding them in a central Interaction Point (IP). The fact that the particles must acquire their final energy in one single pass and the need to keep the overall collider length within reasonable limits require extremely high electric fields for acceleration and bunched beam operation. Another important aspect to consider is the much lower repetition frequency of linear machines compared to circular ones: typically in a range of 5-100 Hz instead of, for instance, LEP's 44 kHz. This implies that the required luminosity (rate of collision events) for particle physics experiments can only be reached with extremely small transverse beam dimensions at the IP and the highest possible number of charged particles per beam bunch. As luminosity is directly proportional to beam power, the overall acceleration power efficiency becomes a key parameter in the design of linear colliders.

There is, therefore, a strong scientific case for an $e^-e^+$ collider, complementary to the LHC, that can study the properties of the Higgs boson and other particles with unprecedented precision and whose energy can be upgraded. The Technical Design Report (TDR) of the International Linear Collider (ILC) has been completed, with large European participation. The initiative from the Japanese particle physics community to host the ILC in Japan is most welcome, and European groups are eager to participate. Europe looks forward to a proposal from Japan to discuss a possible participation.

To stay at the forefront of Particle Physics, these design studies driven by High Energy Physics projects should be coupled to a vigorous accelerator R&D programme, including high-field magnets and high-gradient accelerating structures, in collaboration with national and international institutes, laboratories and universities [1].

## 1.1 The Future Linear Colliders (FLCs)

During the last twenty years, dedicated and successful work by research groups worldwide has demonstrated that a linear collider can be built and reliably operated. Two $e^-e^+$ linear collider projects have been proposed: The International Linear Collider (ILC) in the range of 1 TeV and the Compact Linear Collider (CLIC) in the range of 10 TeV.

The ILC is a 200-500 GeV, upgradeable to 1 TeV, center-of-mass high-luminosity $e^-e^+$ linear collider, based on 1.3 GHz Superconducting Radio-Frequency (SCRF) accelerating cavities (Figure 1.1) at 31.5 MV/m. The use of SCRF technology was recommended by the International Technology Recommendation Panel (ITRP) in August 2004, and shortly thereafter endorsed by the International Committee for Future Acceleratos (ICFA). In an unprecedented milestone in high-energy physics, the many institutes around the world involved in linear collider R&D join in a common effort to produce a global design for the ILC. As a result the ILC Global Design Effort (GDE) was formed. The GDE membership reflects the global nature of the collaboration, with accelerator experts from all three regions (Americas, Asia and Europe). The first major goal of the GDE was to define the basic parameters and layout of the machine (Figure 1.2). During nearly a year the Baseline Configuration Document (BCD) was used as the basis for the detailed design work and cost estimate culminating in the completion of the second major milestone, the publication of the ILC Reference Design Report (RDR) [2]. With the completion of the RDR the GDE has begun an engineering design study, closely coupled with a prioritized R&D program. The goal was to produce the Technical Design Report (TDR). The TDR

was published in June 2013, presenting the matured technology design and construction plan for the ILC [3].

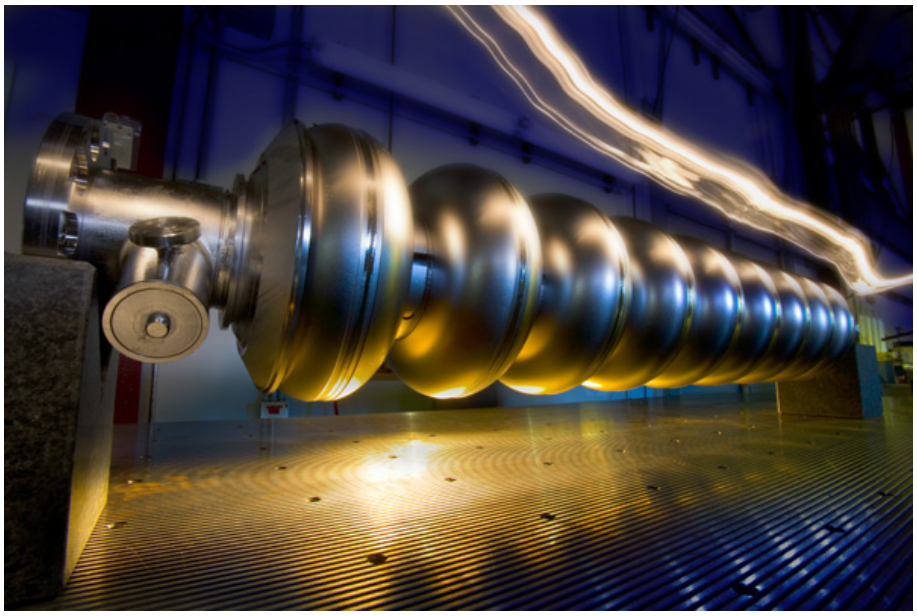

Figure 1.1: A 1.3 GHz superconducting niobium nine-cell cavity designed for the ILC.

Beam Test Facilities are required for critical technical demonstrations, including accelerating gradient, precision beam handling and beam dynamics. In each case, the test Overview of Critical R&D facility is used to mitigate critical technical risks as assessed during the development of the RDR. Test facilities also serve to train scientific and engineering staff and regional industry. In each case, design and construction of the test facility has been done by a collaboration of several institutes. To demonstrate the industrialization of the Superconducting RF technology and its application in a linac, the European X-Ray Laser Project (XFEL) is under construction in DESY Hamburg since 2007 and has to be finished in 2015. In this complex the pilot facility: Free-Electron Laser in Hamburg (FLASH), is the only operating electron linac where it is possible to run close to reference design gradients with nominal ILC beams. The primary goals of the 9 mA beam loading experiment are: the demonstration of the bunch-to-bunch energy uniformity and stability, characterization of the limits at high-gradient, quantification of the klystron power overhead required for control and measurement of the cryogenics loads. This facility provides important information on several goals of the “cryomodule string test”, and is the only source of data for this kind of experiments.

An important technical challenge of ILC is the collision of extremely small beams of a few nanometers in size. The latter challenge has three distinct issues: creating small emittance beams, preserving the emittance during acceleration and transport, focusing the beams to nanometers and colliding them. Accelerator Test Facility (ATF) at High Energy Accelerator Research Organization (KEK) was built to create small emittance beams, and succeeded in obtaining an emittance that almost satisfies the ILC requirements. The ATF2 facility, which uses the beam extracted from ATF damping ring, was constructed to addresses two major challenges of ILC: focusing the beams to nanometer scale using an ILC-like final focus and providing nanometer stability. The two ATF2 goals, first one

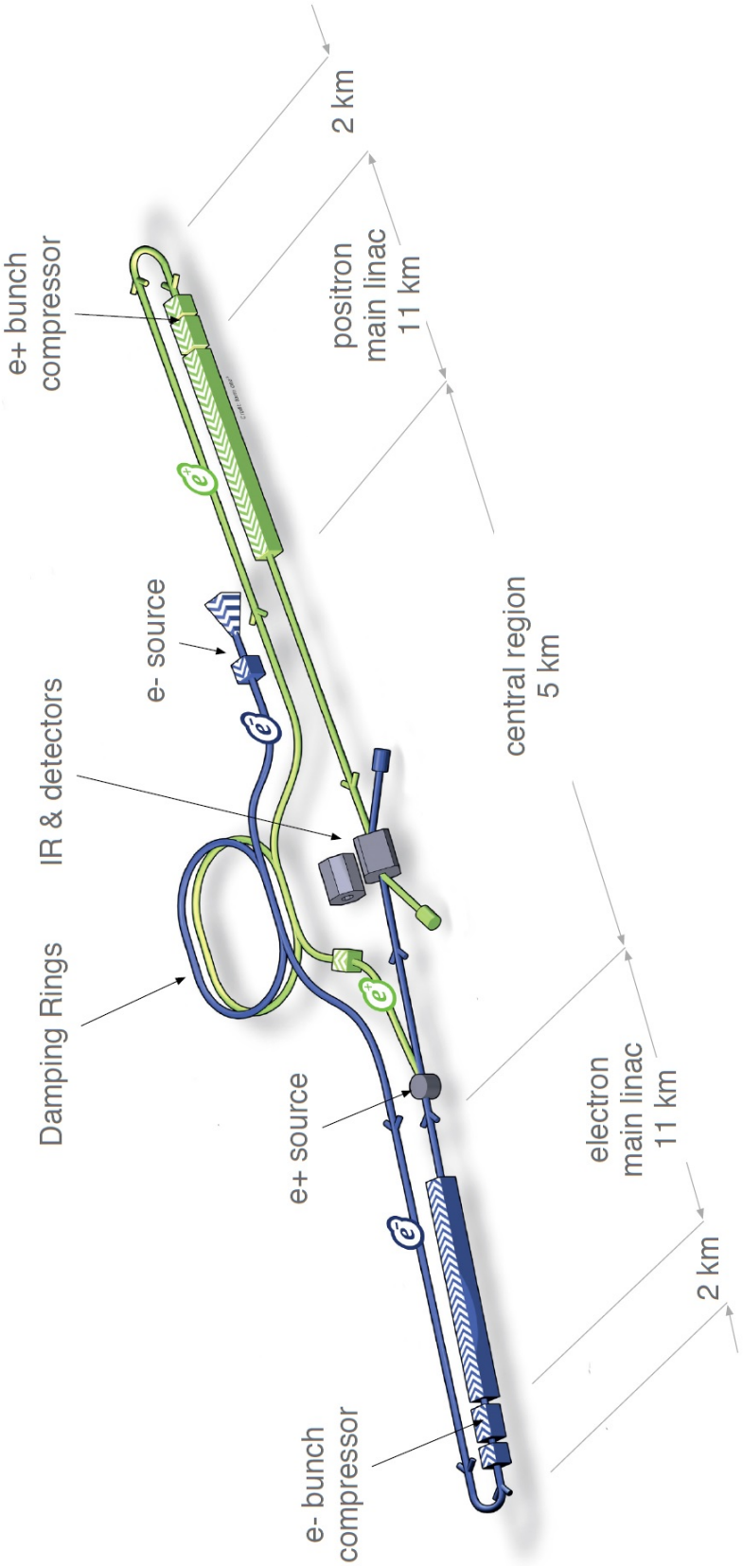


Figure 1.2: Schematic layout of the ILC, indicating all the major subsystems: $e^-$ and $e^+$ sources, bunch compressors, main linacs and the central region, comprising the Interaction Region (IR) and the detectors.

being achievement of 35nm beam size, and second being achievement of nanometer scale beam stability at IP, are being addressed sequentially.

Another key issue in the R&D of the ILC is the Damping Rings (DR) needed to achieve the ultra-low emittance (2 pm in vertical direction) required. In this framework three areas have been identified: the developing of methods to suppress the electron cloud instability and its impact on ultra-low emittance beams, undertaken mainly at the Cornell Electron-positron Storage Ring Test Accelerator (CesrTA); the demonstration of the ultra-low vertical emittance operation and the demonstration of fast injection/extraction system undertaken in ATF.

Within the framework of an international collaboration with 43 partners in 22 countries, the CLIC study aims at a center-of-mass energy range for $e^-e^+$ collisions of 0.5 to 5 TeV, optimised for a nominal center-of-mass energy of 3 TeV. In order to reach this energy in a realistic and cost efficient scenario, the accelerating gradient has to be very high - CLIC aims at an accelerating gradient of 100 MV/m. Superconducting technology being fundamentally limited to lower gradients, only room temperature travelling wave structures at high frequency (12 GHz) are likely to achieve this gradient. In order to optimize the production of sufficient RF power for this high gradient, CLIC relies upon a two-beam-acceleration concept: The 12 GHz RF power is generated by a high current electron beam (drive beam) running parallel to the main beam. This drive beam is decelerated in special power extraction structures (PETS) and the generated RF power is transferred to the main beam. This leads to a very simple tunnel layout without any active RF components (i.e. klystrons). Both beams can be generated in a central injector complex and are transported along the linac.

The CLIC Test Facility (CTF3), built at CERN by an international collaboration, aims at demonstrating the feasibility of the CLIC scheme of multi-TeV $e^-e^+$ linear collider. It is meant to demonstrate the technical feasibility of the key concepts of the novel CLIC RF power source, e.g., generation of high-charge, high frequency electron bunch trains by beam combination in a ring using transverse RF deflectors and operation with a fully-loaded drive-beam accelerator. CTF3 will also be used to test CLIC critical components and in particular will provide the 12 GHz RF power needed to test the main beam accelerating structures at the nominal gradient and pulse length (100 MV/m for 140 ns). As a result of this work, the Conceptual Design Report (CDR) [4] was published in October 2012.

For several years, the particle physics community has been developing the ILC and the CLIC projects. In June 2012, ICFA took the decision that the two projects start to work together under a unique Linear Collider effort collaborating on the technical issues that are common to both. L. Evans has been appointed as the new Linear Collider Director. The new leadership role unifies the two efforts, providing direction for research and development on both accelerator technologies. This new structure for Linear Collider development is a strong signal of the globally integrated nature of particle physics. He will work with three associate directors, one for each of the ILC, CLIC and the associated directors.

## 1.2 The Compact Linear Collider (CLIC)

The Compact Linear Collider (CLIC) study explores the possibility of reaching the multi-TeV energy region by developing a novel acceleration technology, the two beam acceleration, providing a gradient of 100 MV/m in accelerating structures at room temperature in a 48 km-long machine, reaching a collision energy of 3 TeV.

The layout of the CLIC accelerator complex is displayed in Figure 1.3. The generation and the pre-acceleration of the Main Beams (MB) take place in the injector linacs, followed by an emmitance reduction stage in the Damping Rings (DR) (bottom of the figure) until the target values of 500 nm and 5 nm for the normalized beam emittance in the horizontal and vertical planes, respectively, are met. A common linac further accelerates the small emittance beams before their transport through the main tunnel to the turnarounds. The acceleration of the MB begins after the turnarounds with a gradient of 100 MV/m. Traditionally, the accelerating structures in the MB linacs would be powered by klystrons. In this novel acceleration scheme the klystron powering is replaced by the generation of a second beam, the Drive Beam (DB), and its compression and extraction of RF power close to the MB accelerating structures.

The top part of Figure 1.3 shows the DB generation in two linacs and the successive time compression of the DB pulses in the Delay Loops (DL) and Combiner Rings (CR1 and CR2). The time-compressed DB reaches a current of about 100 A at a beam energy of about 2.4 GeV. This compressed DB is transported through the main tunnel to 24 individual turnarounds. Each DB segment is directed by pulse extraction elements, for the final RF power generation, into the accelerating structures of the MB. Hence in the main linac tunnel four beam transport lines can be found: the transport lines of the MB and DB, the acceleration line for the MB and the deceleration line for the DB. After collimation and final focusing in a long Beam Delivery Section (BDS), the beams collide in the IP in the center of the complex.

### 1.2.1 The CLIC two-beam acceleration scheme

The two main linear accelerators of CLIC must accelerate electrons and positrons from 9 GeV to 1.5 TeV in one pass. Additionally, the accelerating field gradient must be as high as possible to keep the length of the machine under reasonable limits. This favours the choice of a room temperature system based on copper accelerating structures instead of superconducting accelerating cavities, as these have an inherently limited maximum field gradient. The accelerating field gradient is generated by feeding these structures with very high RF power. A detailed optimization procedure taking into account the design luminosity, cost (mainly tunnel length), RF breakdown and beam stability issues as well as power efficiency has resulted in the following parameter values for the CLIC acceleration system: 100 MV/m of accelerating field gradient and an RF frequency of 12 GHz. This high accelerating field leads to an RF power of about 270 MW per metre of active structure length at the input of the accelerating structure. A total of about 9.2 TW of RF peak power is required for both linacs. Such high power levels cannot be maintained for very long, the beam bunch train to be accelerated is only 156 ns long, with a repetition frequency of 50 Hz. The RF pulse feeding the structure is longer, 244 ns, taking into account the filling time of the acceleration structures. A rough estimate of a system based on individual RF power sources (klystrons), assuming a klystron unit power of 50 MW with a hypothetical pulse compression factor of 5, determines that about 35000 such klystrons

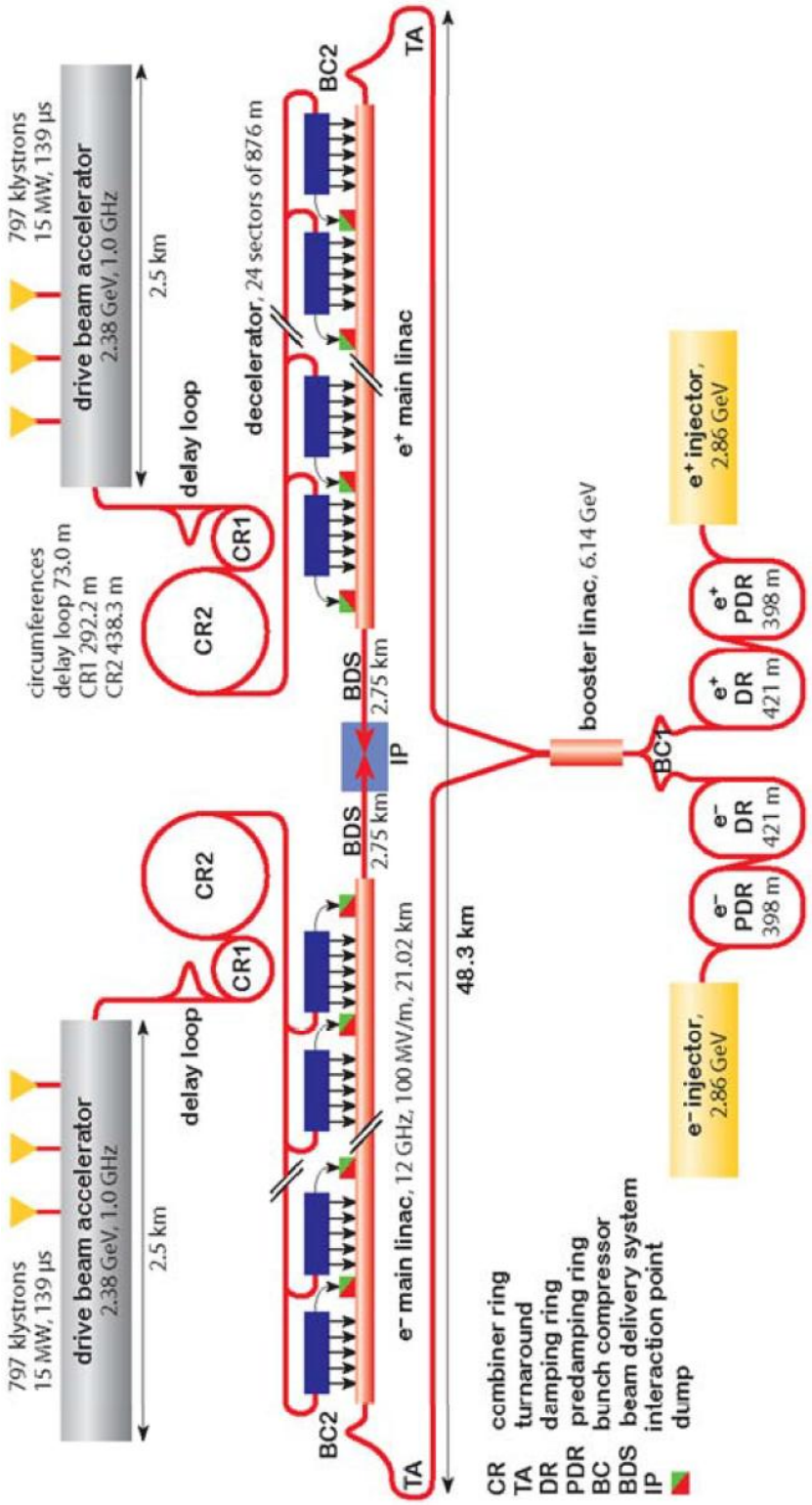


Figure 1.3: Layout of the CLIC complex, showing the Main Beam linacs with their dimensions (center),the Main Beam injection system (bottom) and the Drive Beam generation (top) and deceleration systems (center).

would be required, together with their supporting equipment, not considering the losses in the pulse compression system. This is an infeasible solution. Instead, CLIC is based on a two-beam scheme, where the power for acceleration is transported to the accelerating structures by a second $e^-$ beam, the DB, running parallel to the MB. Beam power is extracted from this beam, converted to RF power in special RF devices called Power Extraction and Transfer Structures (PETS) and transported to the accelerating structures in the MB running at a distance of about 60 cm. One PETS provides RF power for two accelerating structures, as shown in Figure 1.4.

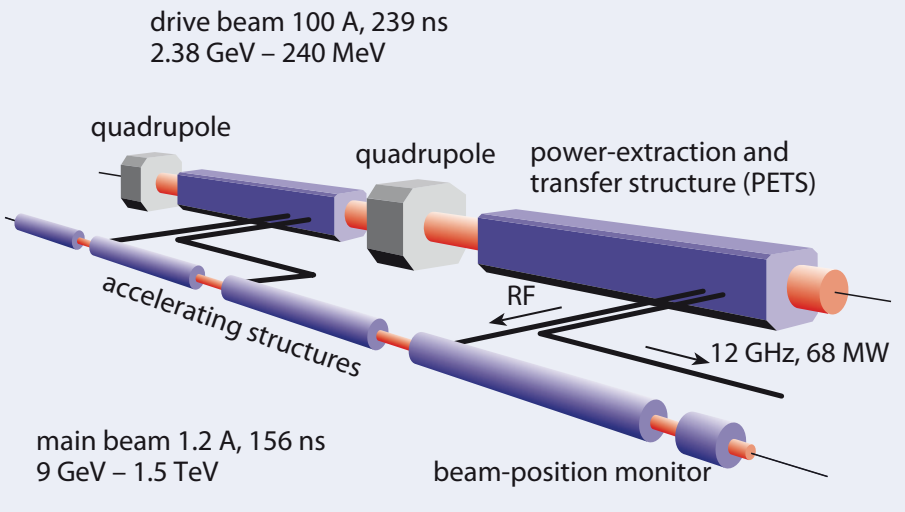


Figure 1.4: Principle of the CLIC two-beam acceleration scheme: The beam power of the Drive Beam is converted to RF power in the PETS, each feeding two accelerating structures of the Main Beam, running parallel at a distance of 60 cm.

CLIC is divided into sectors on average 876 m long, each with about 3000 accelerating structures, accelerating the MB by about 62 GeV. The DB consists of bunch trains, each train supplying one sector with RF power. These trains need relatively low energy, 2.4 GeV, but high peak current of about 100 A during the pulse. About 84% of the stored energy in each train is converted to RF power, after which the train is dumped at the end of its sector. At this point a new DB bunch train arrives to supply the following linac sector. Each of the two main linacs consists of 24 such sections. Each fresh Drive Beam pulse train carries a peak power of about 240 GW. After the beam is decelerated, the 16% of this power is eventually dumped. The RF power pulses are very short, 244 ns, and follow each other with a repetition frequency of 50 Hz. Therefore, the average beam power transported to each linac sector is only 2.9 MW.

The DB is generated at the center of the CLIC complex and is transported in counter flow to the Main Beam, after which turnaround loops make it run parallel with the Main Beam. The first bunch train runs all the way to the first sector at the low-energy end of the main linac, the following one is directed to the turnaround located 876 m upstream; the next ones travel subsequently shorter distances to the next turnaround loops. The gradually reducing travel distances ensure proper synchronization of the arrival of the DB bunch trains in their corresponding decelerating sectors. CLIC has a single tunnel, which houses the MB linac, the DB and the transfer lines. Therefore at each point the tunnel

has four beam lines: the DB and MB of the high-energy linac as well as the DB and MB transfer lines. Every 876 m turnaround loops bring the DB parallel to the MB and after this distance beam dumps dispose of the decelerated DB bunch trains. This is shown in Figure 1.5.

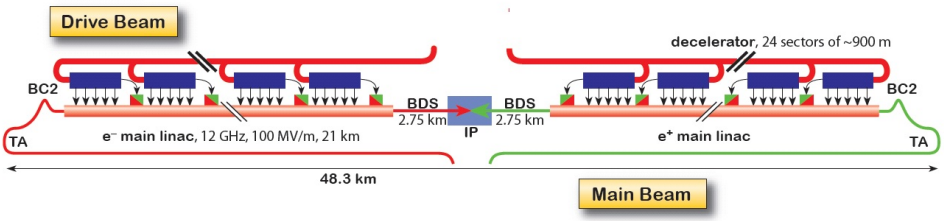


Figure 1.5: Each Drive Beam bunch train supplies RF power to a sector containing 2984 accelerating structures in the Main Beam. Each linac consists of 24 such sectors.

This two-beam acceleration scheme is the most power-efficient solution for CLIC, as the transport of power to the PETS, where it is converted to RF power, is done by an $e^-$ beam, therefore, nearly lossless.

### 1.2.2 Beam position monitoring requirements in the CLIC Drive Beam decelerator

A short description of the DB timing properties and generation scheme will be made for a better understanding of the beam position monitoring requirements in the CLIC DB decelerator.

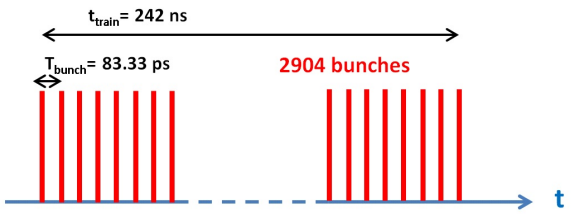


Figure 1.6: CLIC Drive Beam time structure.

The DB bunch train consists of 2904 charged bunches of 8.3 nC each, at a bunching frequency of 12 GHz, whose total duration is 242 ns (Figure 1.6). However, for machine protection purposes [4] [5], such a beam cannot be generated at once. The DB linacs generate first a safe pilot beam with 30 bunches at a 0.5 GHz frequency. This would correspond to only 1 full bunching slot out of 24. Following the successful passage of this beam, a new pilot beam is generated with 30 more bunches at the same frequency (60 in total). Finally, after the successful passage of this beam, a last pilot beam is generated with 60 more bunches and a header, making 121 bunches in total. The beam is now 242 ns long, 1 full bunching slot out of 24.

This beam is later combined in the CRs and DLs in several stages, obtaining gradually 2 full bunches out of 24, 3 out of 24, 6 out of 24 and further intermediate stages until

reaching the final DB configuration (24 full out of 24). This intensity ramp scheme is flexible, being always possible to send any beam configuration with $n$ full and $24 - n$ empty bunching slots. The process is illustrated in Figure 1.7.

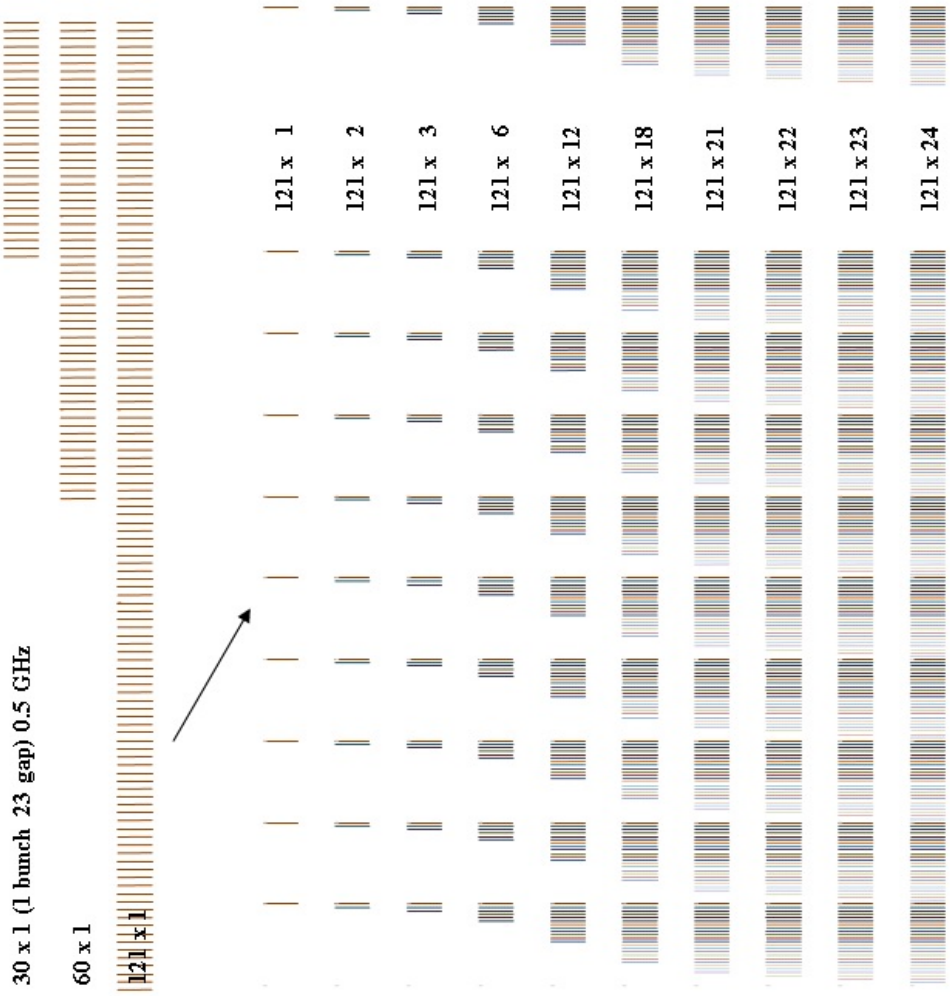


Figure 1.7: CLIC Drive Beam pilot beams (top) and intensity ramp (bottom): from 30x1 bunches at 0.5 GHz, to 121x24 bunches at 12 GHz [5].

The Beam Position Monitors (BPMs) for the DB decelerator must satisfy the following requirements [4]:

- **Quantity**. CLIC comprises approximately 200 km of beam lines in total, which require beam position monitors of different kinds. For the Main Beam linacs, about 4000 BPMs with a resolution under 50 nm will be needed. The Drive Beam decelerators, due to the strong focusing of the beam and its high energy dispersion, require a much large figure: 41580 units, amounting to 75% of all CLIC BPMs. Therefore, the selected design will have to be as compact and economic as possible.
- **Interference suppression**. CLIC is to be constructed in a modular approach, where the DB part of the CLIC Module (Figure 1.8) is composed of two periods, each one

containing a quadrupole to steer the beam, a BPM and a PETS to extract the beam power and convert it to RF. Each module constitutes a FODO lattice, alternating F-type quadrupoles, which focus the beam in the horizontal plane and defocus it in the vertical plane, with D-type quadrupoles, defocusing the beam in the horizontal plane and focusing it in the vertical one. In this lattice distribution, the BPMs will be placed immediately adjacent to the PETS, which emit an interfering signal at 12 GHz with a power of about 135 MW. A significant percentage of this signal propagates from the PETS to the adjacent BPM (Figure 1.9) through the circular waveguide formed by the vacuum pipe, as its frequency is above the cut-off frequency of the fundamental mode, $TE_{11}$, 7.6 GHz for a diameter of 23 mm. Processing the signals from the BPM at the natural beam bunching frequency (12 GHz) in this scenario would lead to the position measurement being perturbed by the interfering signal from the PETS.

- **Time resolution**, understood as the minimum duration of a given beam deviation that is detectable by the BPMs. There is an interest in monitoring position changes of the DB during its generation process, which lasts about 80 ns before reaching steady state. The target time resolution value is 10 ns. In order to fulfil this requirement, it is necessary to develop a readout method that adequately reflects the position signal during the passage of the 242 ns long beam pulse train.

- **Spatial resolution**, understood as the detection limit of the BPM to resolve a minimum relative change of the beam position. Successful dispersion-free steering of the DB depends on the spatial resolution of the BPMs, the target value being 2 $\mu$m in a beam aperture of 23 mm, which requires amplitude measurement at high resolution, about one part in 6000 in amplitude and requiring accurate calibration.

- **Dynamic range**: Due to the different configurations studied for the Drive Beam (Figure 1.7), it is not easy to dimension the dynamic range to achieve the required spatial resolution, 2 $\mu$m for all cases. The system must be able to withstand the high signal values expected when the beam deviation is maximum, but also to perform a correct measurement with the lowest charge beams.

The last three concepts are described in full detail in Chapter 2 for a generic BPM. The target figures for the CLIC DB BPMs are summarized in Table 1.1.

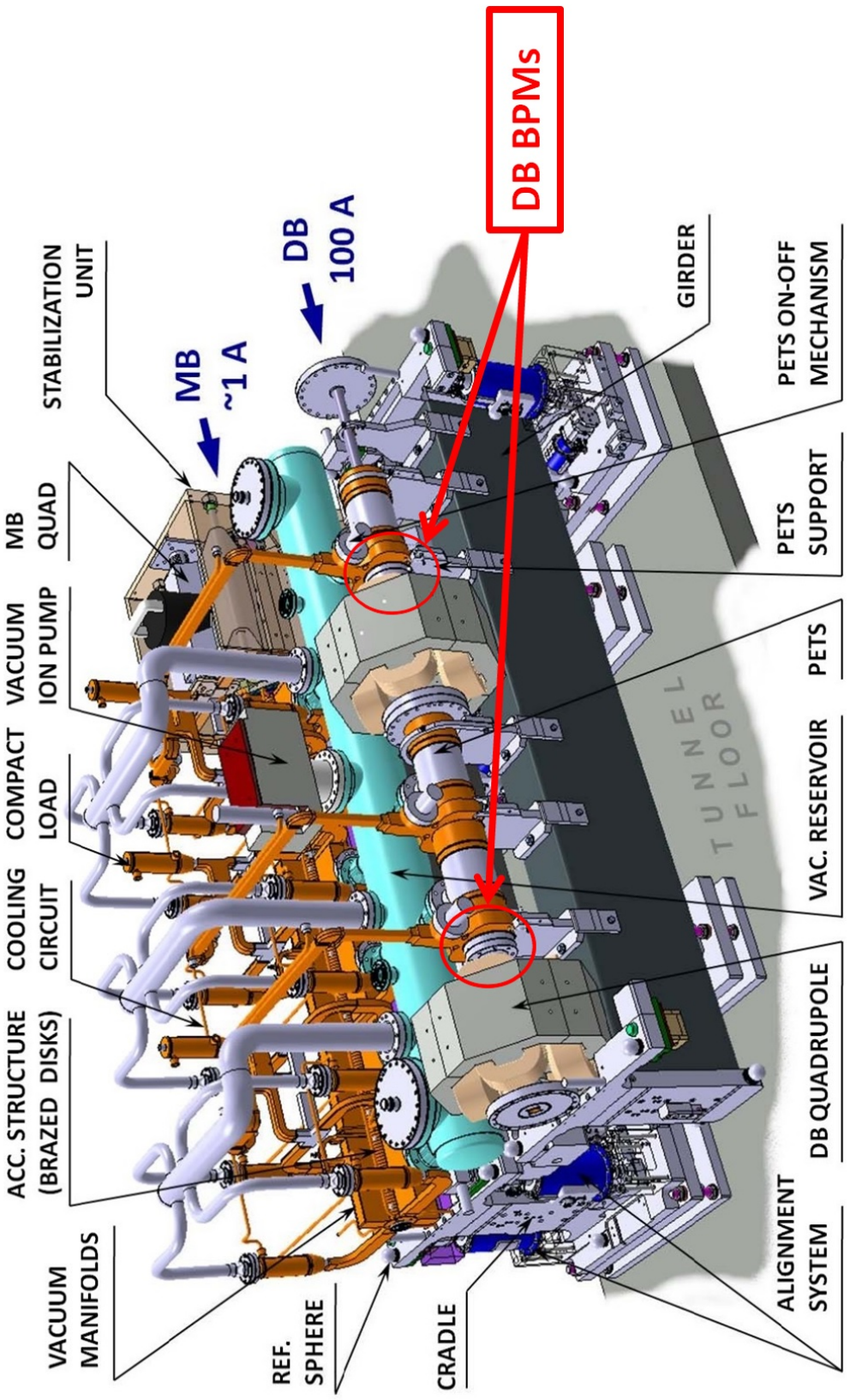


Figure 1.8: Layout of the CLIC Module, with two periods containing a quadrupole, BPM and PETS for the Drive Beam.

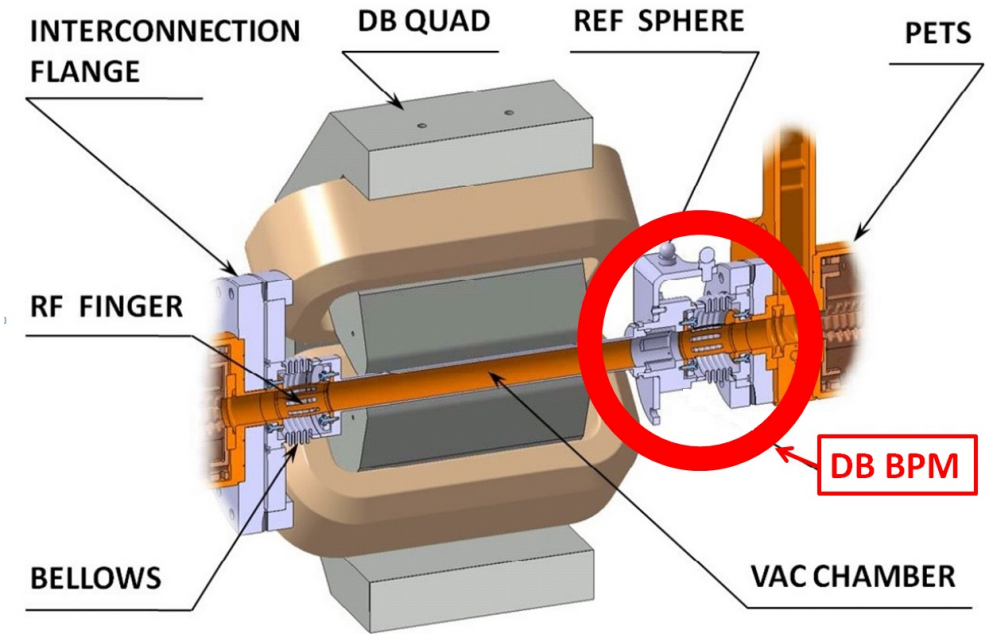


Figure 1.9: Location of the BPMs in the Drive Beam: each BPM is adjacent to a quadrupole (type F or D) and a PETS.

| Parameter | Value |
|---|---|
| Number of BPMs | 41580 |
| Nominal beam current | 101 A |
| Frequency | 12 GHz |
| Bunch charge | 8.3 nC |
| Bunch length | 10 ps |
| Bunches per train | 2904 |
| Bunch train duration | 242 ns |
| Vacuum pipe aperture | 23 mm |
| Spatial resolution | 2 $\mu$m |
| Time resolution | 10 ns |
| Accuracy | 20 $\mu$m |

Table 1.1: Beam position monitoring requirements in the CLIC Drive Beam decelerator.

## 1.3 The CLIC Test Facility 3 (CTF3)

The CLIC Test Facility (CTF3) [6], has been built at CERN by an international collaboration as a proof of concept for the CLIC DB generation and the two-beam acceleration scheme, as required from the International Linear Collider Technical Review Committee. The first results of CTF3 studies have been presented in the CLIC CDR [4], setting an important milestone on the road to CLIC.

Figure 1.10 shows the layout of CTF3, consisting of a 150 MeV $e^-$ linac followed by a magnetic chicane to provide for bunch lengthening before a series of two rings, a delay loop and the combiner ring, in order to minimize coherent synchrotron radiation

effects. After the chicane the beam may be combined by a factor two in the 42 m circumference delay loop, and up to a factor five in the 84 m circumference combiner ring. Alternatively, uncombined beams with a current of 3.5 A may be delivered to the CLIC Experimental Area (CLEX) without entering the delay loop and after only a half turn in the combiner ring. Up to this point, the CTF3 is a scaled-down version of the CLIC drive beam complex required to generate the drive beam as a combined beam of high-current and high-frequency $e^-$ bunch trains as delivered by the combiner ring. It intends to demonstrate the principle of the bunch-interleaving technique using RF deflectors to compress the DB pulses. In CTF3 the compressed beam, with an energy of 150 MeV, 28 A of nominal beam current, a bunch spacing of 83.33 ps (12 GHz) and a train length of 140 ns, is sent into CLEX. Figure 1.11 shows the layout of CLEX, hosting the Test Beam Line (TBL) and the Two Beam Test Stand (TBTS), replaced by the CLIC Two-Beam Module (TBM) in 2014, where the CLIC acceleration scheme is tested, including the extraction of RF power from the DB and its transfer to the accelerating structures of the MB.

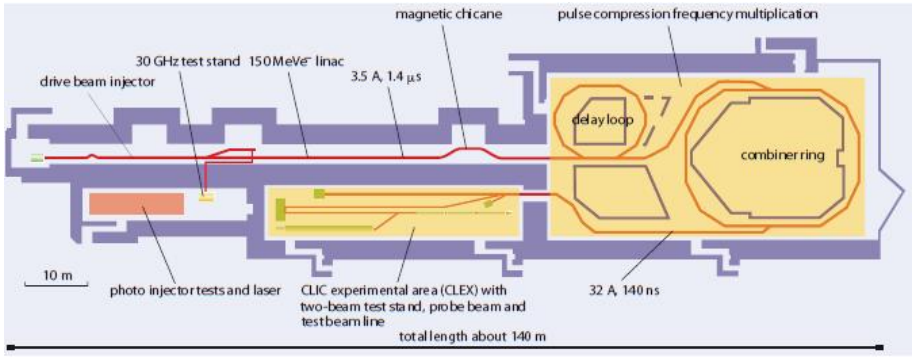


Figure 1.10: Layout of the CLIC Test Facility 3 (CTF3), where the beam from the injector passes through a 150 MeV linac (top), a delay loop and a combiner ring (right) before being delivered to the CLIC Experimental Area (CLEX) (bottom).

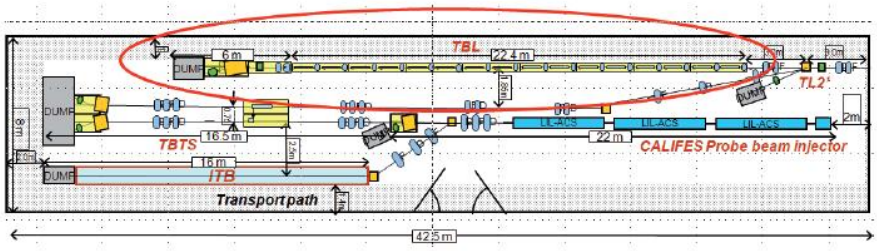


Figure 1.11: Layout of the CLIC Experimental Area (CLEX), showing the Test Beam Line (TBL), the Two-Beam Test Stand (TBTS) and the CALIFES probe beam injector.

The main differences between the CTF3 beam and the CLIC DB are the linac energy and the maximum beam current, with values of 150 MeV and 28 A instead of 2.4 GeV and 101 A respectively. The bunch train duration in CTF3 varies between 140 ns and 242 ns, the nominal duration in CLIC. Additionally, due to the lower initial beam energy, the percentage of extracted beam power in CTF3 is smaller than the foreseen value for CLIC: 54% instead of 90%. Further features of both beams are compared in Table 1.2.

| Parameter [units] | Symbol | TBL | CLIC |
|---|---|---|---|
| Number of PETS | $N_{\mathrm{PETS}}$ | 16 | 1492 |
| Length of PETS [m] | $L_{\mathrm{PETS}}$ | 0.80 | 0.21 |
| Initial average current [A] | $I_0$ | 28 | 101 |
| Power per PETS [MW] | $P$ | ~138 | 135 |
| Initial energy [MeV] | $E_0$ | 150 | 2400 |
| Mean energy extracted [%] | $\eta_{\mathrm{extr}}$ | ~54 | 84 |
| PETS sync. frequency [GHz] | $f_{\mathrm{RF}}$ | 12 | 12 |
| Number of FODO cells | $N_{\mathrm{FODO}}$ | 8 | 524 |
| Length of FODO cells [m] | $L_{\mathrm{FODO}}$ | 2.82 | 2.01 |
| Pulse length [ns] | $t_{\mathrm{pulse}}$ | 140-242 | 242 |
| Transient length [ns] | $t_{\mathrm{fill}}$ | 3 | 1 |
| Bunch length r.m.s. [mm] | $\sigma_{\mathrm{z}}$ | 1.0 | 1.0 |
| Initial norm. emmitance [$\mu$m] | $\epsilon_{\mathrm{N}}$(x,y) | 150 | 150 |
| Beampipe radius [mm] | $a_0$ | 11.5 | 11.5 |

Table 1.2: Comparison of the Drive Beam parameters for CTF3 (TBL) and CLIC.

Especially relevant in the project of this thesis is the Test Beam Line (TBL) at CLEX, as it will allow to test our BPMs with the previously described beam, the closest alike to the future CLIC DB as received in the decelerator. The BPMs of TBL [7] will be used as reference.

The main roles of TBL are the following [8]:

- Proof of concept of the CLIC DB decelerator, with the study and demonstration of its technical feasibility and operation, with the extraction of as much beam energy as possible, demonstrating the power generation technology needed for the two-beam acceleration scheme.
- Demonstration of the stability of the decelerated beam and the produced RF power in the X band by the PETS.
- Benchmark for simulation tools and coding as a validation of the systems involved in the CLIC DB decelerator design.

The TBL layout is highlighted in the top part of Figure 1.11 and, like the DB part of the future CLIC Module, it consists of a series of FODO cells, each with two periods containing a quadrupole (alternating types F and D), a BPM and a PETS. A 3D view of a TBL cell design is shown in Figure 1.12. The quadrupoles, which performs the alternate focusing of the beam every two periods and also the necessary beam steering for proper beam transport along the line, are also equipped with remotely controlled movers for beam-based alignment. The lattice is optimized for the decelerated part of the beam, higher energy particles will see less focusing. The betatron phase advance per cell is close to the theoretical value of 90 degrees per cell for a round beam.

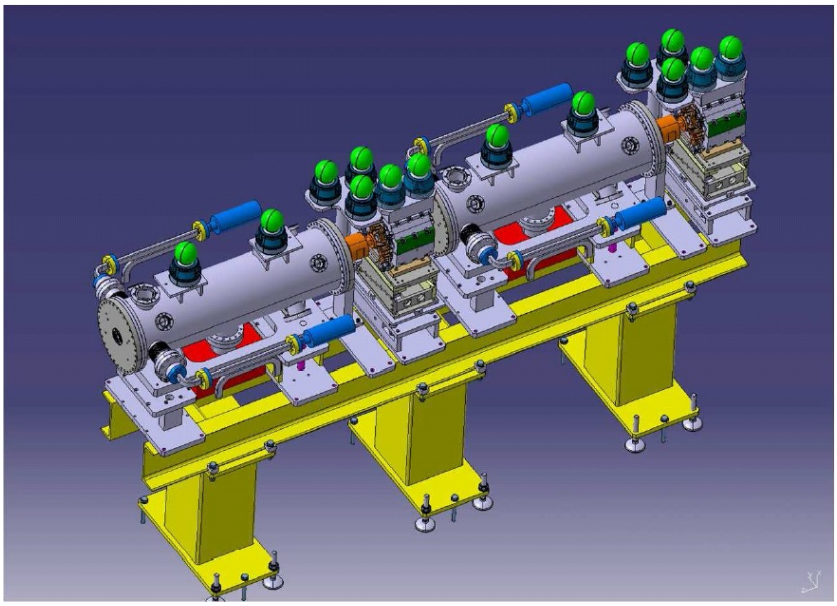

Figure 1.12: 3D view of a FODO cell in TBL, containing two periods of a quadrupole, a BPM and a PETS (the beam direction is from right to left).

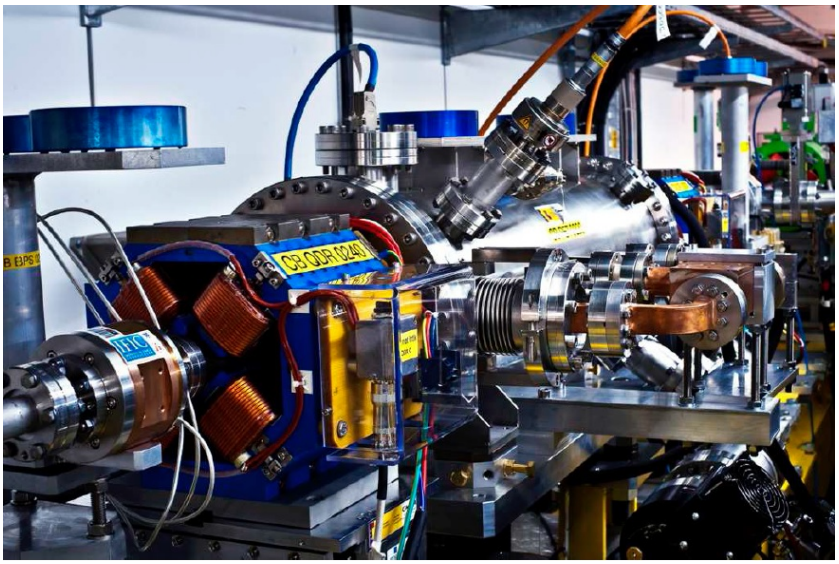

Figure 1.13: TBL view, taken at the limit between two cells: it is possible to see the BPM and the quadrupole of a cell and the PETS corresponding to the upstream neighbouring cell.

The available space in CLEX allows the installation of up to 16 cells with a length of 1.4 m per cell. The TBL is placed after the first bending magnet of the chicane toward the TBTS line (Figure 1.11). The diagnostics section in front of the bending magnet measures the beam properties at the entrance of TBL, although it is formally a part of Transfer Line 2 (TL2). Therefore, TBL starts with a matching section consisting of a quadrupole doublet, a BPM and a pair of correctors, in both the horizontal and the vertical planes, allowing parallel displacement of the beam to excite orbit oscillations in a controlled way.

The matching section is followed by sixteen identical cells as described above. At the end of the beam line another diagnostic section is installed allowing a characterization of all relevant beam parameters. This section consists of a quadrupole doublet and an Optical Transition Radiation (OTR) screen dedicated to transverse beam profile and emittance measurements. A spectrometer with an angle of 10° and a second screen measure the beam energy and energy spread. A segmented beam dump enabling time-resolved energy measurements is also in place. The section is completed by another BPM and a Beam Profile Radio-Frequency monitor (BPR, button pick-up type) providing a proportional signal to the bunch length. The total length of TBL is about 28.4 m including the decelerator line of 22.4 m with the 16 cells being a single vacuum sector, and the diagnostic section of 6 m.

# Chapter 2

# Beam Position Monitoring in Particle Accelerators

## 2.1 Introduction

In any particle accelerator, the beam instrumentation and diagnostics systems are essential components, as they provide the necessary information about the behavior of the beam and its properties. The measurement and monitoring beam properties also reflects the quality of the machine, and provide opportunities for improvements, i.e. by observing the beam response under well-defined excitation, analysis of instabilities, discovering alignment errors of guide field magnets, or by adding beam monitor signals into automatic feedback systems.

The monitoring of some beam parameters is of particular relevance [9], [10]:

- **Beam current (or beam intensity)**. Often different methods need to be applied to monitor the DC beam current or the intensity of individual bunches.
- **Beam orbit**, measured using the data from position readings at multiple locations along the accelerator beam pipe.
- **Beam energy**, often measured indirectly with help of a Beam Position Monitor (BPM) in a dispersive area, or using a dedicated spectrometer arrangement.
- **Beam emittance**, based on the transverse beam profile. Size and shape of the particle distribution in the transverse plane, e.g. by use of screens, wires, or more sophisticated non-invasive measurement methods.
- **Longitudinal emittance**, based on the bunch length. Similar to the transverse plane, the longitudinal distribution of the particles in the RF bucket has to be measured, typically with broadband electromagnetic Pick-Ups (PU) or using synchrotron light emitted from deflecting fields.

While the monitoring of the beam intensity is essential, the BPMs play the most important role in the accelerator beam instrumentation. A large number of installed BPMs along the beam line, typically more than four per betatron oscillation, allows a variety of beam diagnostics, including machine commissioning and troubleshooting. BPM technologies are also used for dedicated betatron tune monitors (in ring accelerators), and transverse feedback systems.

Beam monitors are tools for the observation of the beam in a particle accelerator, and like any other tool, these diagnostics systems are tailored to the needs and requirements of the users and the machine. A few quite different cases can be distinguished:

- **Lepton beams**. Electron or positron beams with higher energies than 1 GeV are ultra-relativistic. This means that Electro-magnetic beam monitors make use of a pure TEM-like field surrounding the beam. Furthermore, usable synchrotron light is emitted already at low energies, which give additional choices for non-invasive observation of some of the beam parameters.

- **Hadron beams**. Protons are 1836 times heavier than leptons. Even at high energies, the field components of the beam have longitudinal components, which can limit some beam parameter measurements. Often, the non-relativistic behavior has to be taken into account. The large particle mass transforms into a high beam power, with high damage potential, which limits some invasive beam measurement methods.

- **Linear accelerators**. The beam passes only once through the linac or beam-line. Single-pass operation of beam monitors is more demanding, often requires more bandwidth of the instrument, and limits the use of repeated measurement statistics to improve the signal-to-noise ratio.

- **Ring accelerators**. Beams are circulating many times, in storage rings for even hours. Additional parameters have to be monitored, e.g. betatron tune, beam life time, etc., and some beam monitors have to cover a wider range with respect to the beam intensity. Often a greater variety of same type beam monitors need to be installed, to cover various integration times, e.g. single selectable bunch, bunch-by-bunch, turn-by-turn, or an average measurement over many turns.

The work described in this thesis is focused on the development of a stripline-type BPM for the CLIC Drive Beam decelerator. In the following section we describe the fundamentals of beam position monitoring.

## 2.2 Fundamentals of Beam Position Monitoring

The term Beam Position Monitor (BPM) refers to all diagnostics devices that measure as their primary goal the transverse beam position (center-of-charge) inside the vacuum pipe of the accelerator. The beam position is a property that can be measured by different methods and beam detector styles. Most commonly used for bunched beams are broadband electromagnetic PUs [9]. These button or stripline style detectors are of rather simple design, are reliable, and apart from serving as non-destructive diagnostics device, are suitable for most BPM applications. The beam position also can be detected using a narrowband passive RF resonator. This so-called cavity BPM utilizes a beam excited dipole eigenmode to detect the transverse beam displacement.

### 2.2.1 Beam-induced Electromagnetic Fields and Wall Image Current

A static point-like charge $q$ in a free space is the source of an electric field $\vec{E}$ whose radial field line distribution is given by Coulomb's Law. However, when this charge is placed inside a vacuum chamber, its electric field must also fulfil the boundary conditions of

$\vec{E}_{\parallel} = 0$ at the beam pipe wall. Figure 2.1 [11] shows the resulting field distribution for $\vec{E}$ in a long conducting pipe with circular cross section of radius $a$. At the surface of the conducting pipe the electric field has only transverse components $\vec{E}_{\perp}$, subsequently the surface charge density $\sigma_q^w$ induced on the pipe wall depends only on those transverse field components:

$$\sigma_q^w = -\epsilon_0 E_{\perp} \tag{2.1}$$

where the superindex $w$ represents the field-induced quantity on the pipe wall, the subindex $q$ indicates the source charge and $\epsilon_0 = 8.8542 \cdot 10^{-12}$ F/m is the vacuum permittivity. The induced charge distribution per unit length $\Lambda_q^w(s)$ along the longitudinal direction $s$ is given by:

$$\Lambda_q^w(s) = \frac{dq_w}{ds} = 2\pi a \sigma_q^w \tag{2.2}$$

This line-charge density, shown in Figure 2.1 results from the integration of the surface charge density $\sigma_q^w$ over the azimuth of the beam pipe. The total induced charge on the beam pipe wall is identical to the source charge, but with opposite sign $q_w = -q$.

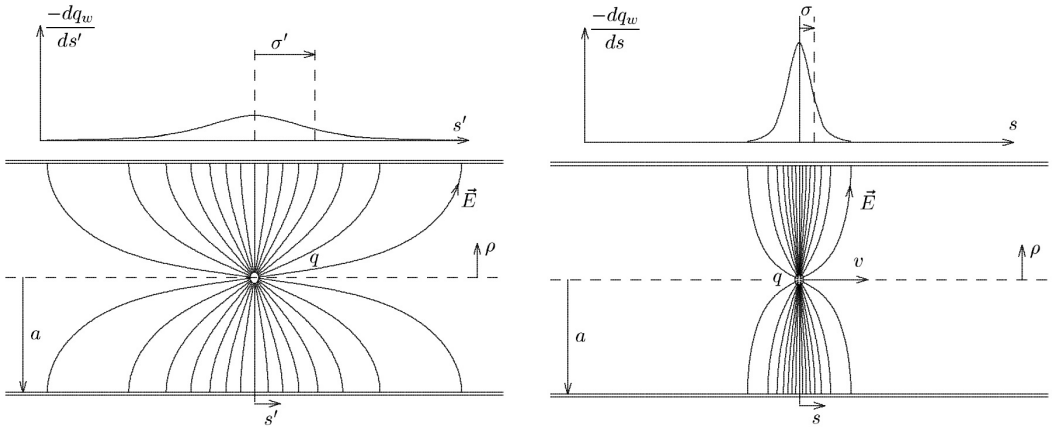


Figure 2.1: Electric field of a static (left) and a moving charge with Lorentz factor $\gamma = 4$ (right) in a circular cylindrical chamber.

For a point charge $q$ moving longitudinally with constant velocity $v_s = \beta c$, with $c = 2.998 \times 10^8\ m/s$ being the speed-of-light in vacuum, a magnetic field adds to the electric field, as a consequence of the charge motion, which represents an electric current. The variation of electric and magnetic fields due to the acceleration of the charge from static to a velocity $v_s$ is described by the Lorentz transformation of special relativity.

If $\vec{v} = 0$ the field distribution corresponds to the static situation (Figure 2.1, left). At a velocity $v_s = \beta c$ the field components which are parallel and perpendicular to the direction of motion of $\vec{v}$ are transformed. The Lorentz transformation applies to arbitrary fields and establishes an implicit dependence of the fields on the position $\vec{r}$ and time $t$. In our case, an observer moving with the charge $q$ would see only an electric field because $q$ is static having a magnetic field $\vec{H}' = 0$. However, for a stationary observer, a purely azimuthal magnetic field is produced due to the velocity of the charged particle and the electric field is now time varying. Both the electric and magnetic fields perceived by the stationary observer are related as follows [12]:

$$\vec{B} = \frac{\mu}{c^2}(\vec{v} \times \vec{E}) \tag{2.3}$$

where $\vec{B} = \mu\vec{H}$ is the magnetic induction vector and $\mu = 4\pi \cdot 10^7 (\mathrm{N/A}^2)$ is the magnetic permeability of free space.

The previous equations imply that the transverse components of the field grow with increasing Lorentz factor $\gamma = 1/\sqrt{1-\beta^2}$, while the longitudinal components remain constant as the velocity increases. Figure 2.1 [11] (right) shows the electric field lines for a charge moving at about 97% of the speed of light ($\beta = 0.968, \gamma = 4$), seen by the stationary observer at a given time. Accordingly, at relativistic velocities the electric and magnetic field lines tend to concentrate within smaller opening angles around the transverse direction, $\alpha \approx 1/(\beta\gamma)$. Subsequently the longitudinal distribution of the wall induced charge $\Lambda_q^w(s)$ narrows with an average length given by its r.m.s. value $\sigma_\Lambda$, given by:

$$\sigma_\Lambda = \frac{a}{\gamma\sqrt{2}} \tag{2.4}$$

For a point-charge $q$ traveling at the ultra-relativistic velocity limit $\beta \approx 1$ and $\gamma >> 1$, the induced wall charge $q_w$ concentrates in a ring of zero length on the beam pipe, since $\sigma_\Lambda \to 0$. Electric and magnetic fields become purely transverse, confined into a thin disc, moving along with the particle $q$ (Figure 2.2) [12]. This effect can also viewed as Lorentz contraction of the space in the direction of motion, observed by the stationary observer.

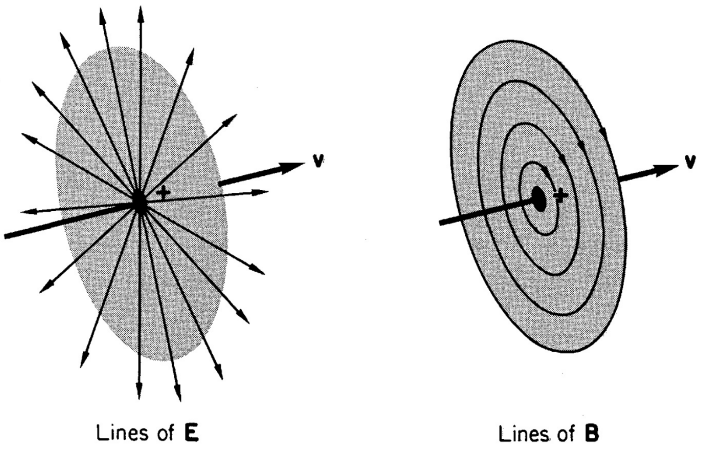


Figure 2.2: Electric (left) and magnetic (right) fields induced by a charge moving at an ultra-relativistic velocity.

By applying the superposition principle, the point charge result described above can be extended to a highly relativistic beam bunch, containing many charged particles. The longitudinal extension of the wall current density, induced by the individual particles of the bunch is given by $\sigma_\Lambda$, and is at a high $\gamma$ substantially smaller than the bunch length, $\sigma_{\mathrm{bunch}} \gg \sigma_\Lambda$. Therefore, the longitudinal distribution of the wall image charge induced by a bunch $\Lambda^w_{\mathrm{bunch}}(s)$ reflects its line-charge density with opposite polarity, with $\Lambda_{\mathrm{bunch}}(s) = -\Lambda^w_{\mathrm{bunch}}(s)$, and assuming $\beta \approx 1$ and $\gamma \gg 1$, i.e. the bunch associated EM fields considered are transverse (TEM fields), as illustrated in Figure 2.3 [11] [13].

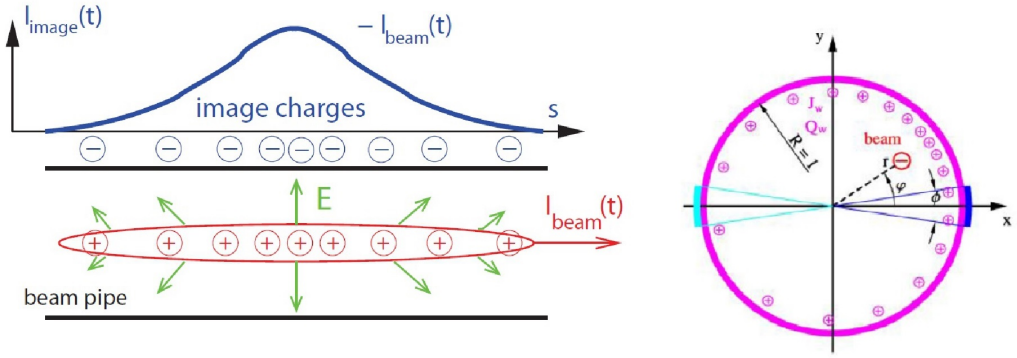


Figure 2.3: Image charges and current induced by the beam in the vacuum pipe walls: centered (longitudinal view, left) and off-centered (cross-section, right).

Thus, a single bunch with $N$ particles of charge $e = 1.6022 \cdot 10^{-19}$ C travelling at a velocity $v_s = \beta c$ in the longitudinal direction $s$ along the vacuum pipe, will represent an instantaneous current of

$$I_w(t) = \Lambda^w_{\text{bunch}}(s)\beta c \tag{2.5}$$

which has a longitudinal profile given by the bunch shape line-charge density, see Figure 2.3.

### 2.2.2 Beam Position Measurement Principle

The basic function of the BPM relies on the induction of image charges on symmetrically arranged electrodes (Figure 2.3) (right). The PU electrodes are isolated and act like near-field RF antennas on the AC (alternating current) of the bunched beam spectrum. The signal level of each BPM electrode depends on the beam-to-electrode coupling, i.e. the distance between beam and electrode, and the beam intensity. The difference of the signal levels of the opposite electrodes, normalized by their sum, is directly proportional to the center-of-mass position of the beam in each transverse axis (shown for the vertical axis in Figure 2.4) [14]. This is the most popular way to extract the beam position from the electrode signals, known as the difference-over-sum normalization method,

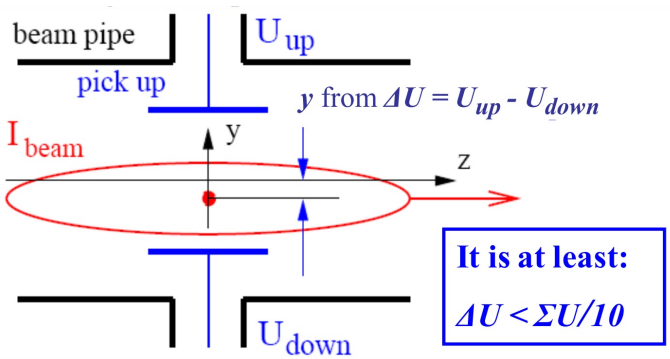


Figure 2.4: Determination of the beam position in the vertical plane using the difference of the measured signals by the pair of opposing electrodes.

In a simplistic view, for relativistic beams ($v \approx c, \beta \approx 1$), the output signal of a broadband BPM PU can be expressed as a function of the angular frequency $\omega$ as [13]:

$$V_{\text{elec}}(x, y, \omega) = s(x, y) I_{\text{beam}}(\omega) Z_{\text{t}}(\omega) \tag{2.6}$$

where $V_{\text{elec}}$ is the output signal of a broadband PU electrode, $s(x, y)$ a sensitivity factor, depending on the beam position $(x, y)$, i.e. the beam-to-electrode coupling factor, $I_{\text{beam}}(\omega)$ the beam current, often approximated by a *Gaussian* function for each bunch signal and $Z_{\text{t}}(\omega)$ is the frequency-dependent transfer function or shunt impedance of the PU. $Z_{\text{t}}(\omega)$ can be defined in the frequency domain according to Ohm's law, characterizes the PU electrode for a centered beam and depends basically on geometrical factors.

The signals provided by the PU are processed by an electronic acquisition system, which consists out of an analog front-end and a digitizing stage, which includes a set of Analog-to-Digital Converters (ADC). The acquired digital position data is sent to the control room, where it is synchronized to the data of the other BPM stations of the beam-line or accelerator. Depending on the specific BPM system configuration, normalization, data decimation (integration), and non-linear correction of position data is performed at the digitizer level, or in the central BPM data acquisition software. The structure of a generic BPM is shown in Figure 2.5.

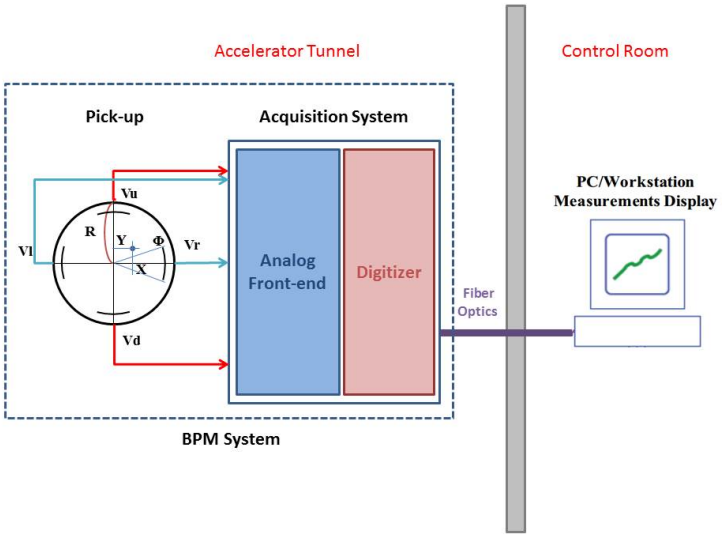


Figure 2.5: Basic structure of a generic BPM system, showing each stage and its usual location.

The horizontal and vertical beam position can be determined from the measured signal amplitudes $V_n$ of the individual electrodes:

$$\begin{aligned} x &= \frac{1}{s_{\text{h}}(x, y)} \frac{V_{\text{right}} - V_{\text{left}}}{V_{\text{right}} + V_{\text{left}}} + OS_{\text{h}} \equiv \frac{1}{s_{\text{h}}(x, y)} \frac{\Delta V_x}{\Sigma V_x} + OS_{\text{h}} \\ y &= \frac{1}{s_{\text{v}}(x, y)} \frac{V_{\text{up}} - V_{\text{down}}}{V_{\text{up}} + V_{\text{down}}} + OS_{\text{v}} \equiv \frac{1}{s_{\text{v}}(x, y)} \frac{\Delta V_y}{\Sigma V_y} + OS_{\text{v}} \end{aligned} \tag{2.7}$$

where $s_{\mathrm{h,v}}(x, y)$ reflects the position sensitivity of the BPM PU, and usually is a non-linear function of both coordinates. In case of a beam pipe with circular cross-section $s_{\mathrm{h}} = s_{\mathrm{v}}$, thus horizontal and vertical position behavior are identical. $OS_{\mathrm{x,y}}$ represent an offset term in the horizontal and vertical planes, respectively, due to mechanical tolerances of the PU and other unwanted asymmetries in the signal processing chains.

### 2.2.3 Characteristics of Beam Position Monitoring Systems

Any implementation of a BPM system has its specific systematics and limitations [14], [15]. They result in characteristics of the overall BPM system, which have to fulfil the basic requirements and functionality, which typically are defined during the design phase of the accelerator.

- **Sensitivity**. The sensitivity $s(x, y)$ for broadband BPM PUs is directly related to the transverse distribution of the wall current (or mirror charges) for a displaced beam, and the integration area defined by the size of the BPM electrodes. For a simplified PU, i.e. a beam pipe with circular cross section, an infinitely thin (line-charge like) beam, and ideal electrodes covering some angle $\varphi$, as shown in Figure 2.3 (right), the position characteristic can be expressed by an analytical function:

$$\begin{aligned} x &= \frac{A-B}{A+B} = \frac{f(x,y,R,\varphi) - f(-x,y,R,\varphi)}{f(x,y,R,\varphi) + f(-x,y,R,\varphi)} \\ y &= \frac{C-D}{C+D} = \frac{f(y,x,R,\varphi) - f(-y,x,R,\varphi)}{f(y,x,R,\varphi) + f(-y,x,R,\varphi)} \end{aligned} \tag{2.8}$$

  where $A$ and $B$ are the signal amplitudes of the two opposite electrodes of the horizontal plane, $C$ and $D$ are the signal amplitudes of the two opposite electrodes of the vertical plane and $f(x, y, R, \varphi)$ is given by:

$$\begin{aligned} f(x,y,R,\varphi) = &\arctan \frac{[(R+x)^2 + y^2]\tan(\varphi/4) - 2Ry}{x^2 + y^2 - R^2} \\ &+ \arctan \frac{[(R+x)^2 + y^2]\tan(\varphi/4) + 2Ry}{x^2 + y^2 - R^2} \end{aligned} \tag{2.9}$$

  basically represents the sensitivity function $s(x, y)$ in Eq. (2.6). An analogous calculation applies for the vertical beam position. the sensitivity in the center of the beam pipe, $s(0, 0)$ can be defined as the slope of the normalized position characteristics for each plane:

$$s_h(0,0) = \frac{d}{dx}\left(\frac{\Delta V_x}{\Sigma V_x}\right) \qquad s_v(0,0) = \frac{d}{dy}\left(\frac{\Delta V_y}{\Sigma V_y}\right) \tag{2.10}$$

  where $\Delta V_{x,y}$ and $\Sigma V_{x,y}$ are the difference and sum signals of the electrode voltages for the horizontal and vertical plane, respectively. In practice the arrangement of the BPM electrodes is different from the cross-section shown in Figure 2.3 (right) and $s(x, y)$ needs to be computed numerically.

  There exists different normalization approaches for the beam position, for example $x, y = 20\log_{10}\left(\frac{\Delta V_{x,y}}{\Sigma V_{x,y}}\right)$ results in a sensitivity expressed in dB/mm.

- **Accuracy**. The accuracy of a BPM defines how well the scaling between the measured signal amplitudes of the BPM electrodes, and a calibrated beam displacement, e.g. in mm is realized. In theory the non-linearities of the BPM PU and those of the analog signal processing needs to be compensated, e.g. by look-up tables or polynomial correction functions. While the non-linear correction enables a correct scaling in general, individual errors due to tolerances of the BPM mechanics or in the analog signal processing may limit the accuracy, or calls for a calibration measurement for each BPM station.

- **Offset and Roll**. The offset, $OS$ in Eq. (2.7), expresses the zero-order polynomial correction term, and is a result of asymmetries in the BPM system due to tolerances in BPM PU mechanics, RF electronics, cables, etc. From the beam dynamics point of view, the offset of the electrical center of each BPM and the magnetic center of the nearby quadrupole magnet is of importance. Using precision mechanical and electromagnetic (stretched-wire) alignment procedures the offset of each BPM can be measured, and put in a pre-alignment data-basis. However, the final offset of each BPM will be measured utilizing the beam, following the well-known Beam-Based Alignment (BBA) procedure. In the same way also the roll between each BPM and quadrupole needs to be evaluated.

- **Spatial resolution**. The spatial resolution defines the detection limit of the BPM system, typically under nominal beam conditions, to resolve a minimum (relative) change of the beam position. While offset and accuracy are dominated by mechanical tolerances, typically in the order of 10 to 100 $\mu$m, the resolution is defined by the PU sensitivity, noise in the electronics, and the integration or measurement time. Depending on the BPM type, the reachable resolution can be in the order of $\mu$m or, for cavity BPMs, even nm.

- **Integration or Measurement Time**. Any beam position measurement is linked with a measurement, or integration time. This time resolution is basically defined by the overall BPM system bandwidth, i.e. bandwidth of the BPM PU, and read-out electronics, including filters in the digital and data acquisition sections. Assuming a constant beam orbit, a long integration time can improve the spatial resolution, however, for beam position measurements on a bunch-by-bunch or turn-by-turn basis a compromise between spatial and time resolution has to be made.

- **Dynamic range**. The BPM system has to cover a range of the beam intensity. At the commissioning of the accelerator, beam intensities usually are kept low, also for safety concerns, while nominal beam operation tries to maximize the beam intensity. The dynamic range of the BPM read-out system has to cover the range beam intensities for a given measurement time. For bunch-by-bunch, or batch-by-batch BPM acquisition the required dynamic range is typically in the order of 30 to 40 dB. However for turn-by-turn BPMs in large ring accelerators this requirement can be very large, and requires the need of switched attenuators and gain stages, which can compromise the calibration.
  In practice, the lower end of the dynamic range is given by noise-floor and insertion losses in the front-end electronics, the upper end is set by non-linearities (power or voltage handling) in active stages, e.g. amplifiers, switched attenuators, mixers, etc.

## 2.3 Types of BPM Pick-Ups (PU)

### 2.3.1 Linear-cut PUs

For different beam pipe cross-shapes, it is possible to cut a section diagonally so that each half constitutes an electrode, as shown in Figure 2.6, left [14]. The response of such a structure to a displacement of the beam is linear. For a given beam displacement $x$ as shown in Figure 2.6 (right), for the horizontal direction, the image voltage in each electrode is proportional to the projection of the beam on its surface. For a circular linear-cut PU with half aperture $a$, the values of these projections in the horizontal plane are:

$$l_{\text{right}} = (a + x)\tan\alpha \tag{2.11}$$

$$l_{\text{left}} = (a - x)\tan\alpha \tag{2.12}$$

which are related to the beam displacement as follows:

$$x = a\frac{l_{\text{right}} - l_{\text{left}}}{l_{\text{right}} + l_{\text{left}}} \tag{2.13}$$

The position reading is linear and can expressed as a function of the image voltages as:

$$x = a\frac{V_{\text{right}} - V_{\text{left}}}{V_{\text{right}} + V_{\text{left}}} = \frac{1}{s_x}\frac{\Delta V_x}{\Sigma V_x} \tag{2.14}$$

The sensitivity $s_x$ for this case can be then worked out as $s_x = 1/a$. These calculations apply also for the vertical plane.

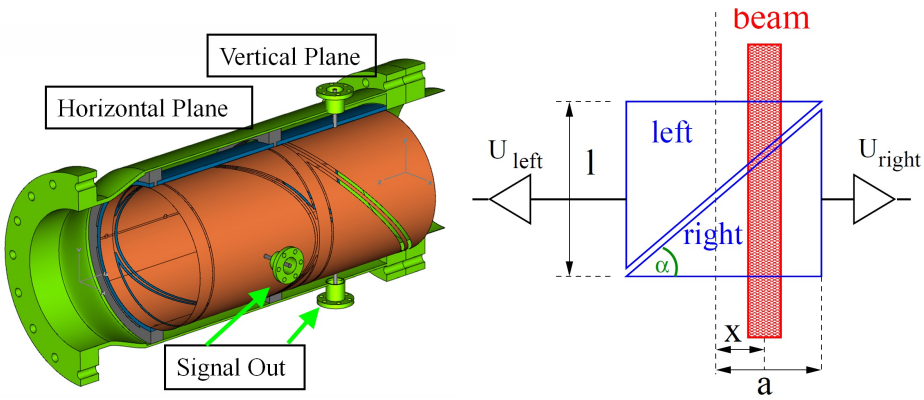


Figure 2.6: Structure of a linear-cut PU with cylindrical electrodes and its position determination scheme.

Careful design of the PU [16] leads to very good linearity values and the absence of any horizontal-vertical coupling, which is a unique feature of this PU type.

However, the value of the position sensitivity can be affected by the crosstalk between adjacent electrodes. To prevent this, an additional grounded separation region or guard ring is usually included in the design of these PUs, managing to reduce the crosstalk up to a factor of three and to increase the sensitivity by a factor of two. On the other hand, if the

electrodes are purely metallic, the separation between adjacent electrodes should always be below a certain limit to prevent field inhomogeneities in the gap.

Linear-cut PUs do not necessarily need to have a circular cross-section. It is only important that the projection of the cut between adjacent electrodes on the vertical and horizontal planes is a diagonal line. Rectangular ("shoebox") realizations have comparable properties to the cylindrical ones [17].

### 2.3.2 Button PUs

Button PUs are the simplest type of BPM, consisting of insulated metallic plates acting as electrodes, whose diameter ranges from several mm to several cm. They are used at proton linacs, cyclotrons and at electron accelerators, where the acceleration frequency $f_{acc}$ is between 100 MHz and several GHz, higher than the ones for proton synchrotrons. The bunch length for which they are suitable is also shorter.

The button electrode is mainly sensitive to the beam electric field. The usual equivalent circuit representation of an electrostatic monitor is a current generator of the same value of the image current intercepted fraction, shunted by the electrode capacitance to ground. If the button is connected to the detector circuit by means of a short run of coaxial cable having characteristic impedance $R_0$ and terminated into an $R_0$ resistor, the transfer (signal) impedance $Z_b(\omega)$ for a centered beam, i.e. the ratio of the voltage induced by the beam at the external termination to the beam current, can be written as [18]:

$$Z_b(\omega) = \phi R_0 \left(\frac{\omega_1}{\omega_2}\right) \frac{j\omega/\omega_1}{1 + j\omega/\omega_1} \tag{2.15}$$

where $\omega_1 = 1/(R_0 C_b)$, $\omega_2 = c/(2r)$ (one electrode trip time), with $C_b$ being the button capacitance to ground, $r$ the button radius, $c$ the speed of light, $\phi$ the coverage factor ($\phi = r/(4b)$), $b$ the beam pipe radius and $j$ the imaginary unit. The cross-section cut of a generic button BPM is shown in Figure 2.7 [14].

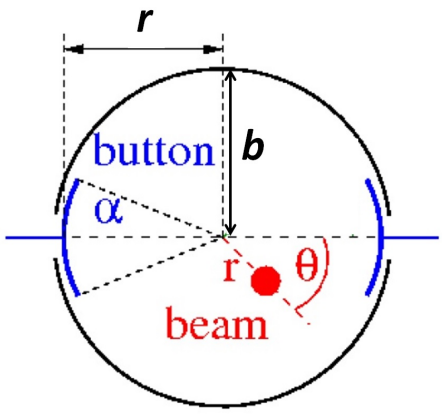


Figure 2.7: Cross-section schematic of a vacuum pipe equipped with button BPMs for the measurement of the beam position in the horizontal plane.

This frequency response is of high-pass type, with two different regimes:

- **Low frequency** ($\omega \ll \omega_1$), where the transfer impedance is given by:

$$Z_b(\omega) = \phi R_0 \frac{j\omega}{\omega_2} = j\omega R_0 \left( \frac{r^2}{2bc} \right) \tag{2.16}$$

- **High frequency** ($\omega \gg \omega_1$), where we obtain:

$$Z_b(\omega) = \phi R_0 \frac{\omega_1}{\omega_2} = \frac{r^2}{2bcC_b} \tag{2.17}$$

In the low frequency regime the electrode acts like a time differentiator. The transfer impedance is largely independent on the value of the capacitance $C_b$, depending only on the load resistance $R_0$ and on the geometrical factors $b$ and $r$. In the high frequency regime the asymptotic response is purely resistive, i.e. the electrode voltage is in phase and proportional to the beam current. The transfer impedance scales with the inverse of the button capacitance and depends on the same geometrical factors above, but not on the value of $R_0$.

Considering these dependencies, it is possible to shape the response in a given frequency region. For example, by increasing the value of the load resistor, the cut-off frequency $\omega_1$ moves towards a lower value, extending the low-frequency response. The high frequency response is not affected as long as the capacitance value is the same. In fact, when dealing with long bunches, sometimes the load to electrostatic monitors is replaced by a high-impedance (cathode) follower mounted very close to the vacuum feedthrough, so to minimize any parasitic capacitance which spoils the high frequency response.

In the high frequency region the response can be enhanced by reducing the capacitance. The drawback is that the cut-off frequency $\omega_1$ moves towards a higher value. In order to improve the sensitivity at all frequencies, a bigger button could be used as the modulus of the transfer impedance scales as $r^2$.

In summary, the overall response can be enhanced by increasing the electrode surface, while an increase of capacitance leads to a reduced response at high frequency and vice versa: the low frequency cut-off of the differentiator response can be reduced by increasing the value of the load resistor. These effects are shown in Figure 2.8 [18].

Short intersections are required with the advantage of a compact mechanical realization. Figure 2.9 [19] shows a typical installation where the four buttons surround the beam pipe. The signal is transferred through a short pin connecting the electrode to a standard RF-connector outside the vacuum. For frequencies in the order of GHz, the signal reflection can be considerable and has to be minimized, optimizing the design of the transition from the button electrode to the connector and the vacuum ceramics. All stages traversed by the signal on its way to the analog electronics need to be matched to 50 Ω. Due to the 50 Ω coupling, the derivative of the beam current is recorded. The capacitance of a button ranges normally between 1 and 10 pF, resulting in a high-pass cut-off frequency of typically between 0.3 and 3 GHz.

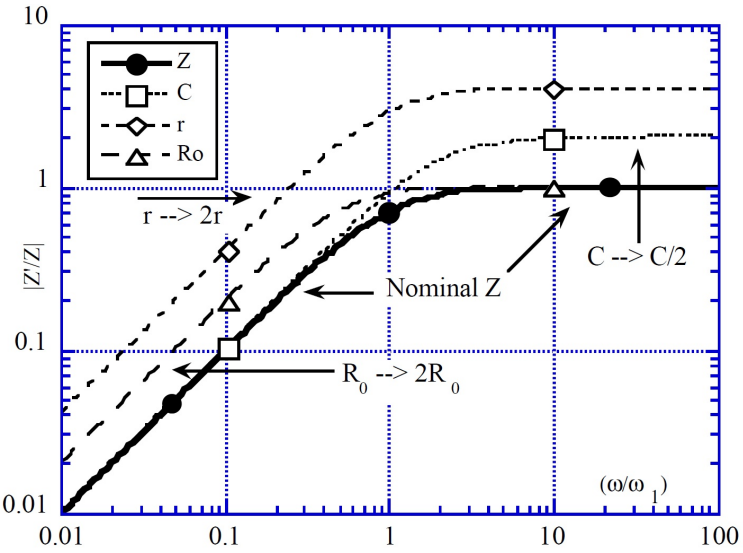


Figure 2.8: Button BPM impedance behavior upon variations of the radius $r$, the load resistor $R_0$ and the capacitance $C_b$.

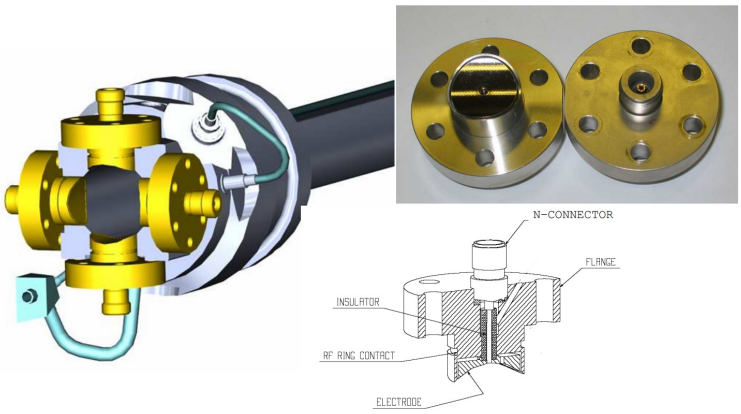


Figure 2.9: Button BPMs in the LHC beam pipe (left). The air side of the prototype (right) is equipped with an N connector.

The design simplicity and low cost of the button and the small size of both the button and the feedthrough make this type of BPM installation the preferred option for many accelerators. However, they are normally less linear than linear-cut PUs and the coupling between their $x, y$ measurement planes is not negligible. Also, if the bunch length becomes comparable to the size of the BPM, the final propagation time leads to a signal deformation. This means that for short bunches button BPMs have to be small and can therefore deliver only low signal levels. Further examples of button BPMs are described in [20–24].

### 2.3.3 Stripline PUs

For the two previously introduced PU types, an electrostatic approach was used, disregarding the effects of signal propagation. In contrast, stripline BPMs are well suited for

short bunch observation because the signal propagation is considered in the design, as is the case for transmission lines in microwave engineering. The azimuthal coverage of the stripline BPM can be larger than of a button type, yielding an increased signal strength. Stripline BPMs also behave as directional couplers which is an additional advantage for colliders with counter-propagating beams within the same beam pipe. It is possible to distinguish between the directions of beam propagation and to record only the position from one beam by suppressing the signal from the counter-propagating one. The electrical properties of such a BPM are comparable to a directional coupler used for microwave devices [25].

In a stripline PU, the electrodes consist of metallic strips of angular coverage $\alpha$ forming a transmission line of length $l$ and characteristic impedance $Z_{strip}$ with the inner face of the vacuum pipe. Figure 2.10 [14] shows a transverse and a longitudinal cut of a generic stripline BPM, in which, for simplicity, only the vertical plane electrodes are represented. Figure 2.11 shows a cross section and a longitudinal view of a stripline BPM designed for the LHC [14].

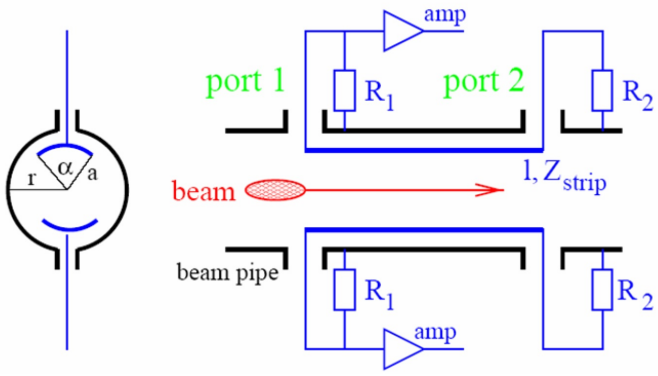


Figure 2.10: Transverse and longitudinal cut of a generic stripline BPM (vertical plane electrodes).

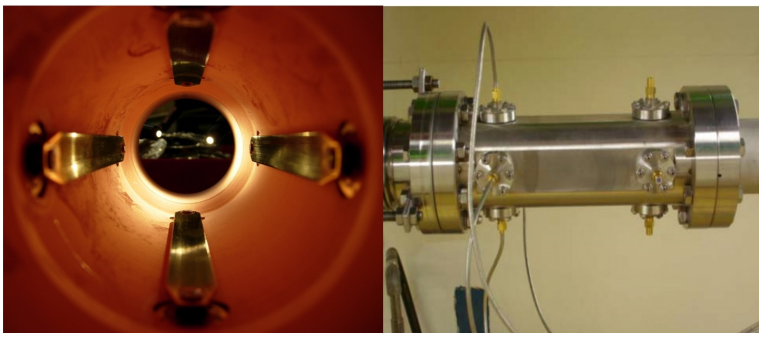

Figure 2.11: Cross section (left) and longitudinal (right) views of a stripline BPM design for the LHC.

When a relativistic ($v = c$) beam charge pulse reaches the upstream port (Figure 2.12, $t = 0$), a Dirac impulse is induced, which splits into two equal parts: an impulse propagating through the output port and another impulse propagating synchronously with the beam along the electrode. When the beam pulse reaches the downstream port (Figure

2.12, $t = l/c$), another Dirac impulse is generated with inverse polarity and also splits into two equal parts: one returning along the electrode to the upstream port and another one cancelling the pulse coming from it (the second one of the generated in $t = 0$). The net signal contribution at the output of the downstream port is then zero. Finally, a pair of Dirac impulses of opposed polarity and separated $2l/c$ in time is observed in the upstream port, being possible to express the impulse response of the device (Figure 2.13) as follows:

$$h(t) = \frac{1}{2}\left[\delta(t) - \delta\left(t - \frac{2l}{c}\right)\right] \tag{2.18}$$

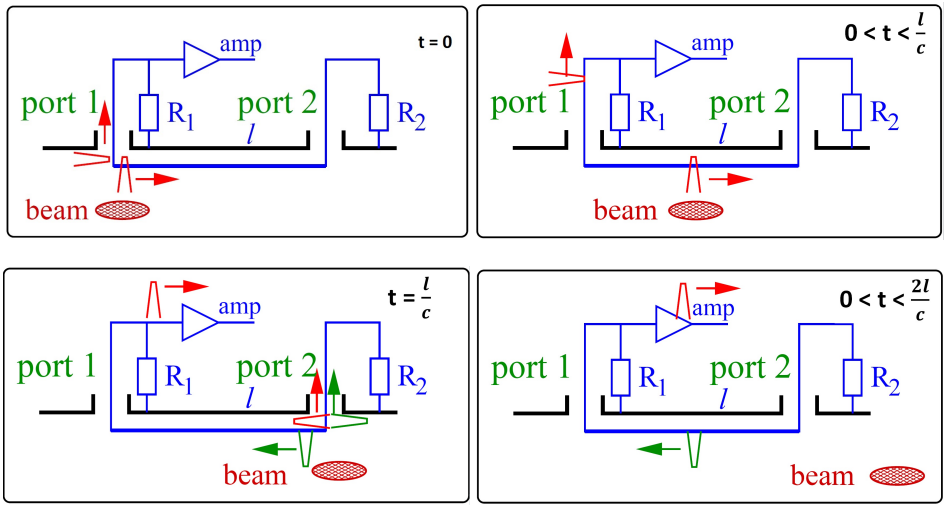


Figure 2.12: Operation principle of a stripline PU with terminated electrodes (8 ports).

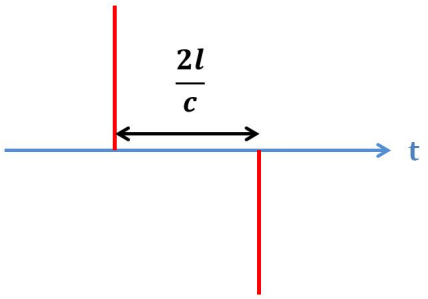


Figure 2.13: Stripline PU impulse response

The transfer function is given by the Fourier transform of $h(t)$ in Eq. (2.18):

$$H(f) = je^{-j\frac{2\pi fl}{c}} \sin\left(\frac{2\pi fl}{c}\right) \tag{2.19}$$

The minima of its magnitude will be located at multiples of $c/2l$ and its maxima at the odd-multiples of $c/4l$, as shown in Figure 2.14 (normalized values) [26].

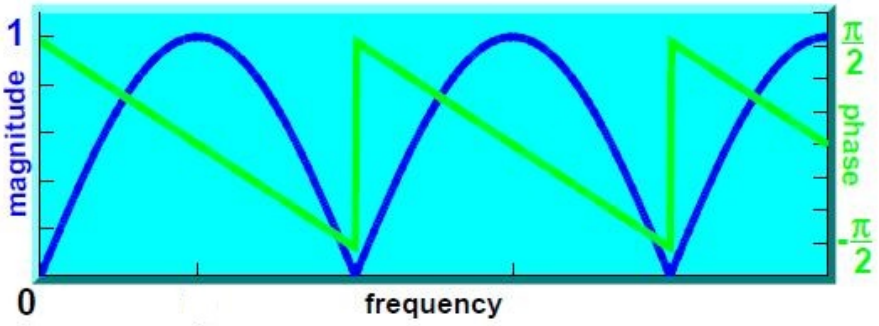


Figure 2.14: Transfer function (magnitude and phase) of a generic stripline PU.

It is possible to implement a mechanically simplified and more compact version of stripline PU replacing the downstream port with a short-circuit, obtaining the same impulse response but saving the cost of four feedthroughs. The details of this implementation will be discussed in Chapter 3.

Pulsed beams consist of a pulse train of a certain duration. If the stripline electrode length, $l$, is dimensioned so that the delay between the pulses present in the impulse response is a natural multiple of the beam bunching period, $T_{\text{bunch}}$, it is possible to make each pulse in the central part of the train cancel with the delayed and inverted version of the pulse generated $N$ periods before. This condition is mathematically expressed as:

$$\frac{2 \cdot l}{c} = NT_{\text{bunch}} \text{ with } N \in \mathbb{N} \tag{2.20}$$

The time response of the system to a multi-bunch beam will be thus simplified to $N$ positive pulses at the beginning and $N$ negative pulses at the end of the train, regardless its duration (Figure 2.15). In the frequency domain, this equates to tuning the $N^{\text{th}}$ notch (not considering DC) of the PU transfer function to the frequency component to be filtered. When dimensioning $l$, the selected value of $N$ will normally be the lowest possible, except in cases where, considering the beam properties, it may cause some problems (such as, for example, an inadequate transverse to longitudinal dimension ratio) or there is an interest in having a particular number of pulses at the beginning or at the end of the multi-bunch time response of the device.

The mechanical realization of this BPM type is more complex compared to the button type due to the difficulty in matching the impedance of the striplines. It is often possible to integrate the stripline BPM inside a quadrupole magnet to reduce the insertion length for the total installation. Several realizations of stripline BPMs are described in [26–31].

### 2.3.4 Inductive PUs

For position determination the Wall Current Monitor (WCM) principle is modified to sense directly the azimuthal image current distribution by at least four strips and is called inductive WCM. A schematic of a generic design is shown in Figure 2.16. The beam pipe is intersected by a ceramic gap and the current strips are installed outside of the beam pipe for better accessibility, as shown in Figure 2.17. The wall current (green lines) is sensed by a transformer surrounding each strip (each strip acts as the primary winding of this

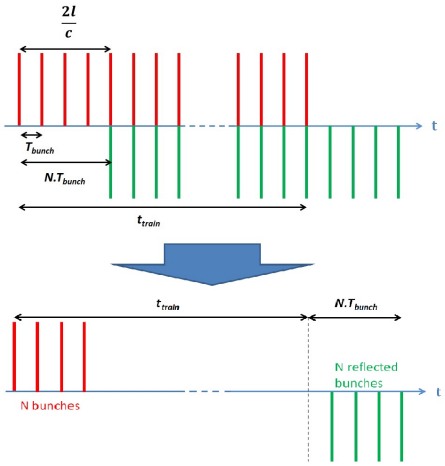


Figure 2.15: Multi-bunch time response of a generic stripline PU.

transformer). The transformer's secondary winding of about 10 to 30 turns is fed to an amplifier for further analog processing. As for the resistive counterpart, ferrites are used to force the low frequency components to the current strips.

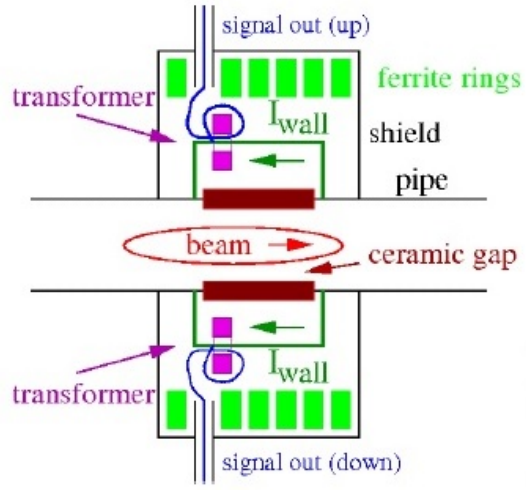


Figure 2.16: Scheme of a generic inductive wall current monitor.

A realization is described in [32]. It uses 8 current strips mounted around the 120 mm diameter beam pipe. The achieved position sensitivity for this device is S = 3.8 $mm^{-1}$ which is about a factor of 2 larger than an ideal linear-cut BPM. A large bandwidth with flat frequency response over six orders of magnitude is achieved. The large bandwidth and the fact that all sensitive parts are installed outside of the vacuum are the main advantages of this BPM type. A modified version of the previously described design has been developed for TBL at CTF3 [7].

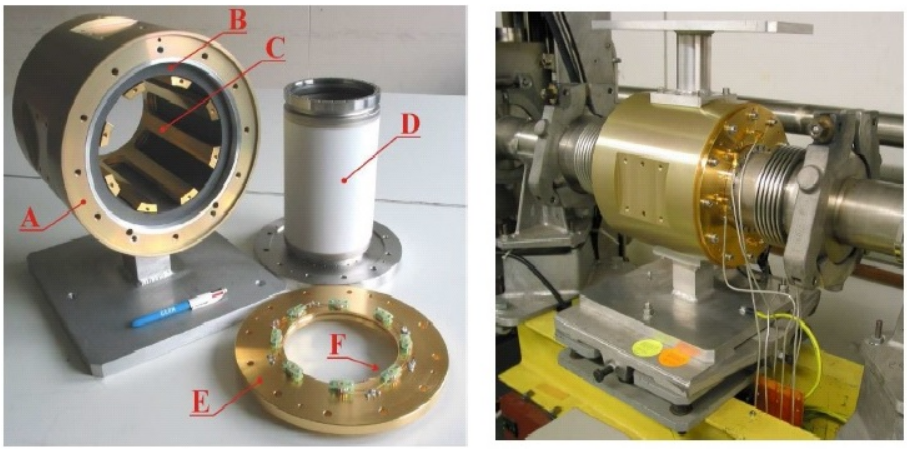


Figure 2.17: Inductive wall current monitor realization for CERN LINAC 2: (A) housing, (B) ferrite rings, (C) current strips, (D) ceramic gap, (E) support and (F) current transformers for the 8 strips.

### 2.3.5 Cavity BPMs

The high accuracy demanded and the very small beam sizes at the Future Linear Colliders (FLCs) and Free Electron Lasers (FEL) require precise beam alignment. In addition, only short pulses ($< 1\,\mu$s) are accelerated with a low repetition frequency, requiring single pulse measurements without averaging. Submicron resolution is often achieved. This challenge can be addressed by the excitation of resonant modes inside a cavity. As short bunches have a wide frequency spectrum, several modes resonating at different frequencies will be excited. This behavior allows for a much higher position sensitivity, as given by the shunt impedance of the dipole mode, than the position monitoring methods based on wall current measurement.

For a pillbox cavity with conductive walls of length $l$ and radius $R$, with $l < 2.03R$, the first Transverse-Magnetic (TM) mode is the fundamental oscillation [33] [13]. The resonance frequencies (*eigenfrequencies*) of the excited $\mathrm{TM}_{mnp}$ modes are given by:

$$f_{mnp} = \frac{c}{2\pi}\sqrt{\left(\frac{J_{mn}}{R}\right)^2 + \left(\frac{p\pi}{l}\right)^2} \tag{2.21}$$

where $c$ is the speed of light in vacuum, $J_{mn}$ is the $n^{\text{th}}$ root of the $m^{\text{th}}$ Bessel function of the first kind and $p \in \mathbb{N}_0$.

The cavity size and the boundary conditions for the electric field at its walls fix the wavelength of the resonant mode (Figure 2.18 [34]). The $\mathrm{TM}_{010}$ mode acts as the monopole mode, with a maximum of the electric field at the center of the cavity, being excited proportionally to the bunch charge. For typical cavity sizes between 5 and 15 cm its resonance frequency $f_{\mathrm{TM}_{010}}$ is in the order of several GHz. The dipole mode, $\mathrm{TM}_{110}$ has a notch at the cavity center and a resonance frequency $f_{\mathrm{TM}_{110}}$ several hundreds of MHz above the monopole mode one. The excitation amplitude of the dipole mode is linearly dependent on the beam displacement as well as bunch charge, while its phase represents the sign. The reference is the phase of the monopole mode, which also needs to be processed. The horizontal and vertical displacements can be distinguished by the different

polarization of the two possible dipole modes. The loaded quality factor $Q_{\text{load}}$ for both modes is chosen to be typically 100 to 1000. A larger value gives a higher signal strength, but reduces the time resolution and by that the possibility to resolve consecutive pulses of about 1 $\mu$s repetition time.

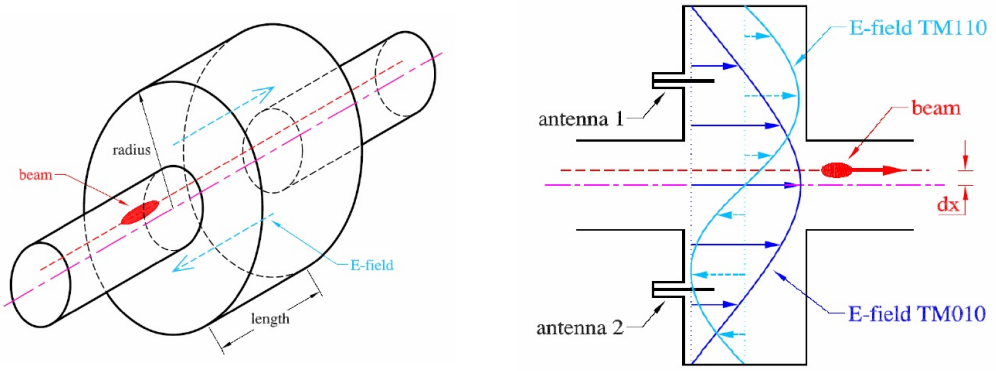


Figure 2.18: Cavity BPM pillbox design (left) and electric field distribution for the monopole and dipole modes (right).

For typical displacements of several $\mu$m only the dipole mode is excited weakly, while the monopole mode with its maximal electric field on the center axis is excited with more signal. Due to the relatively low quality factor, the frequency spectrum is wide and an important percentage of the monopole mode power is present at the dipole mode frequency. An effective method must be chosen to separate the weak dipole mode signal from the monopole contribution, for example, using a waveguide or a slot to implement a High-Pass (HP) filter.

Two different cavities are traditionally built: a position cavity, where the dipole mode is excited, and a reference cavity, where the monopole mode is excited to be used as phase reference for the sign of the beam displacement and for position signal normalization. This approach is followed in the cavity BPMs for the CLIC Main Beam [35] [36]. In this case, both resonance frequencies are separated only 9 MHz, so that the same signal processing can be applied to both dipole and monopole signals for improved stability. The layout of such a device is shown in Figure 2.19 [35]. Further cavity BPM realizations can be found in [37] and [38].

## 2.4 BPM technology selection for the CLIC Drive Beam Decelerator

Among the described beam position monitoring technologies, one must be chosen that addresses the challenges described in Chapter 1, section 1.2.2:

1. CLIC comprises approximately 200 km of beam lines in total, which require BPMs of different kinds. For the Main Beam linacs, about 4000 BPMs with a resolution under 50 nm will be needed. The Drive Beam decelerators, due to the strong focusing of the beam and its high energy dispersion, require a much large figure: 41580

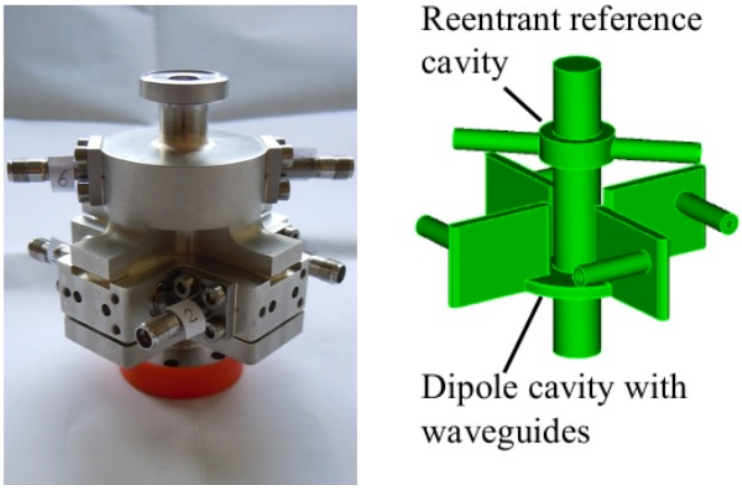


Figure 2.19: Layout of the cavity BPM designed for the CLIC Main Beam.

units, amounting to 75% of all CLIC BPMs. Therefore, the selected design will have to be as compact and economic as possible.

2. The PETS emit an interfering signal at 12 GHz with a power of about 135 MW. A significant percentage of this signal propagates from the PETS to the adjacent BPM (Figure 1.9) through the circular waveguide formed by the vacuum pipe, as its frequency is above the cut-off frequency of the fundamental mode, $TE_{11}$, 7.6 GHz for a diameter of 23 mm. Processing the signals from the BPM at the natural beam bunching frequency (12 GHz) in this scenario would lead to the position measurement being perturbed by the interfering signal from the PETS.

3. The target value for the time resolution is 10 ns. In order to fulfil this requirement, it is necessary to develop a readout method that adequately reflects the position signal during the passage of the 242 ns long beam pulse train.

4. The target value for the spatial resolution is 2 $\mu$m in a beam pipe radius of 12 mm, which requires amplitude measurement at high resolution: the ratio of these quantities yields about 1/6000 in amplitude [4], requiring accurate calibration.

5. Due to the different configurations studied for the CLIC Drive Beam, it is not easy to quote the dynamic range to achieve the required spatial resolution, 2 $\mu$m for all cases. The system must be able to withstand the high signal values expected when the beam deviation is maximum, but also to perform a correct measurement with the lowest charge beams.

In order to meet the first requirement, design simplicity and low cost, the preferred option would be a button BPM. However, as seen in the previous section, these BPMs have an HP transfer function where the cut-off frequency is normally under 3 GHz, which would not allow to filter out the PETS interference at 12 GHz. Among the BPM technologies revised in this chapter, the only one to present a suitable frequency response for this purpose is the stripline. By choosing an appropriate length of the electrodes, it is possible to tune one of the periodic notches of to 12 GHz, filtering out the PETS interference with a large attenuation.

The first prototype to be developed is the most simple and economic option: a compact stripline BPM with short-circuited electrodes, whose design is described in Chapter 3. Chapter 4 describes the design of a suitable electronic acquisition system to process the PU signals. Chapters 5 and 6 describe the tests performed on the first prototype in laboratory and with beam, respectively.

# Chapter 3

# Design of a Stripline Pick-Up with Short-Circuited Electrodes

The first prototype stripline PU for the CLIC Drive Beam was developed at CERN in collaboration with SLAC [39]. This chapter describes the main steps of both the electrical and mechanical design of a compact stripline PU and discusses several geometrical aspects which influence key electrical parameters. Finally, several modifications are suggested for improvement.

## 3.1 Operation principle of a stripline pick-up with short-circuited electrodes

The operation principle of a generic stripline PU and its narrowband rejection properties were explained in Chapter 2, section 2.3. However, it is possible to implement a mechanically simplified and more compact version of stripline PU replacing the downstream port with a short-circuit, saving also the cost of four feedthroughs. The impulse response of the simplified device is the same as the one of the terminated version, although it is generated in a different way. When a relativistic beam charge bunch reaches the upstream port (Figure 3.1, left), a Dirac impulse is generated, which splits into two equal parts: an impulse propagating through the output port and another impulse that propagates along the electrode synchronously with the beam, each one of them with half the charge of the original impulse. In $t = l/c$, time when the second of the generated pulses in $t = 0$ in the upstream port reaches the short-circuit, it is reflected towards the upstream port, arriving in $t = 2l/c$ (Figure 3.1, right). The impulse response is a pair of pulses of opposed polarity separated $2l/c$ seconds:

$$h(t) = \frac{1}{2}\left[\delta(t) - \delta\left(t - \frac{2l}{c}\right)\right] \tag{3.1}$$

The transfer function is given by the Fourier transform of the impulse response $h(t)$ :

$$H(f) = je^{-j\frac{2\pi fl}{c}} \sin\left(\frac{2\pi fl}{c}\right) \tag{3.2}$$

As described in the previous chapter, the notches of the transfer function of a stripline PU will be located at the multiples of $c/2l$ and the maxima at the odd-multiples of $c/4l$.

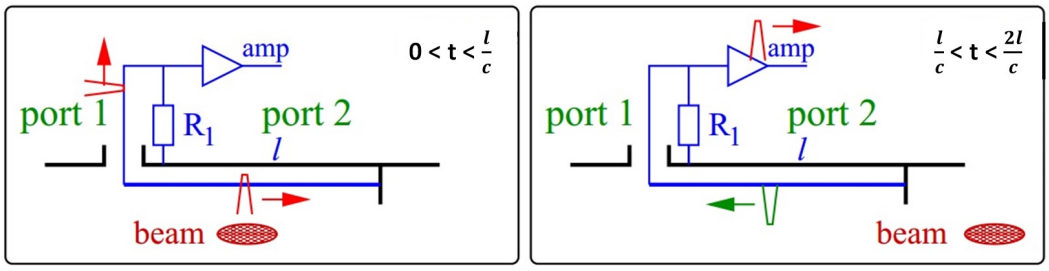


Figure 3.1: Operation principle of a stripline PU with short-circuited electrodes.

## 3.2 Electrical design

### 3.2.1 Electrode length

Once the stripline technology has been selected, the first step of the electrical design of the PU is to calculate the necessary electrode length. From Eq. (2.20):

$$l = N \cdot \frac{c \cdot T_{\text{bunch}}}{2} \quad \text{implies} \quad l = N \cdot \frac{c}{2 \cdot f_{\text{bunch}}} \tag{3.3}$$

where $c$ is the speed of light in vacuum, $f_{\text{bunch}}$ is the beam bunching frequency and $N \in \mathbb{N}$ represents the non-DC notch of the periodic stripline transfer function that is to be tuned to the bunching frequency for its suppression. The value of $N$ to be used in Eq. (3.3) should be as low as possible for design simplicity:

- For $N = 1$:

$$l = \frac{3 \cdot 10^8 \text{ m/s}}{2 \cdot 12 \text{ GHz}} = 12.5 \text{ mm} \tag{3.4}$$

- For $N = 2$:

$$l = \frac{3 \cdot 10^8 \text{ m/s}}{12 \text{ GHz}} = 25 \text{ mm} \tag{3.5}$$

The obtained design length for $N = 1$ is shorter than the aperture of the vacuum pipe (23 mm). In this situation, the fields propagating along the transmission line formed between the electrodes and the pipe wall cease to be strictly Transverse Electro-Magnetic (TEM), originating unwanted resonances at high frequencies [41]. For this reason, the design value for the first stripline PU will be the one given by $N = 2$, that is, $l = 25$ mm, Eq. (3.5).

For $l = 25$ mm, the notches $f_{z_n}$ and the maxima $f_{\text{max}_n}$ of the prototype frequency response (Figure 3.3) are given by Eqs. (3.6) and (3.7), respectively:

$$f_{z_n} = n \cdot \frac{c}{2 \cdot l} = n \cdot \frac{3 \cdot 10^8 \text{ m/s}}{2 \cdot 25 \text{ mm}} = n \cdot 6 \text{ GHz}\ ,\ n \in \mathbb{N} \longrightarrow f_{z_n} = 6, 12, 18... \text{ [GHz]} \tag{3.6}$$

$$f_{\text{max}_\text{n}} = (2n-1)\ \cdot \frac{c}{4 \cdot l} = (2n-1)\ \cdot 3 \text{ GHz}\ ,\ n \in \mathbb{N} \longrightarrow f_{\text{max}_n} = 3, 9, 15... \text{ [GHz]} \tag{3.7}$$

The impulse response of the prototype, considering $N = 2$ in Figure 2.15, will be a pair of pulses of opposed polarity separated by two times the bunching period ($2 \cdot T_{\text{bunch}}$ = 166.67 ps), as shown in Figure 3.2, left. The time response of this prototype to a CLIC Drive Beam multi-bunch pulse train will contain, therefore, two positive pulses

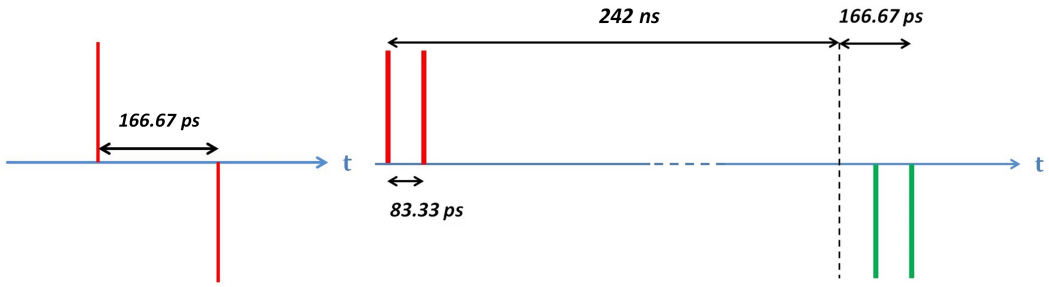


Figure 3.2: Time response of a stripline PU with $N = 2$ to a single bunch (left) and to a multi-bunch beam (right).

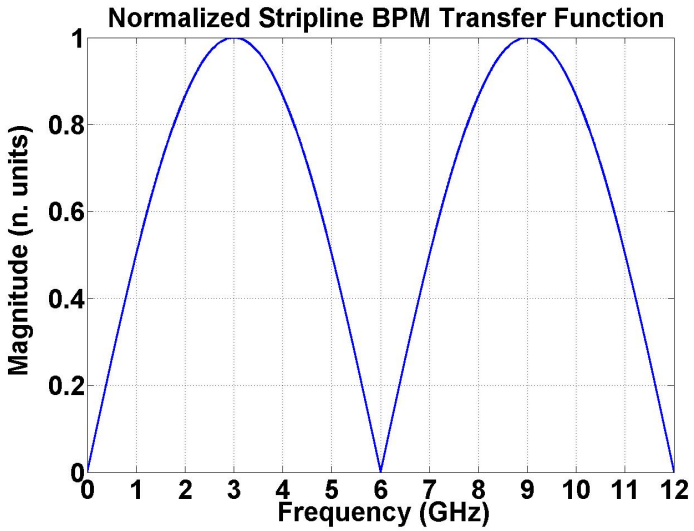


Figure 3.3: Frequency response (magnitude) of a prototype stripline PU with $N = 2$.

at the beginning, separated by a bunching period ($T_{\text{bunch}} = 83.33$ ps) and, after 242 ns, corresponding to the total multi-bunch train length, two negative pulses at the end (Figure 3.2, right).

### 3.2.2 Transverse dimensions

In a stripline BPM, the electrical properties of the transmission lines formed between the electrodes and the vacuum pipe wall are controlled by the dimensions of the cross-section of the BPM. Particularly relevant are the distance between the electrodes and the chamber wall, the electrode thickness and their angular coverage. The most important property to control is the characteristic impedanze $Z_c$, which needs to be matched to 50 Ω. In the following subsections, the characteristic impedance is conceptually described and a set of suitable transverse dimensions is obtained with electromagnetic field simulation tools.

#### 3.2.2.1 Transmission line basics

The simplest possible transmission line is formed by two separate, infinitely long perfect conductors with uniform cross-sections. Figure 3.4 [42] depicts such a line, where the conductors are parallel to the wave propagation direction ($z$ axis) and their cross-sections are denoted by the two closed curves $S_1$ and $S_2$ in the transverse $xy$ plane. The conductors are surrounded by a medium with magnetic permeability $\mu$ and electric permittivity $\epsilon$, assumed homogeneous and isotropic. Other material bodies are assumed to be remote enough not to perturb the field around the conductors.

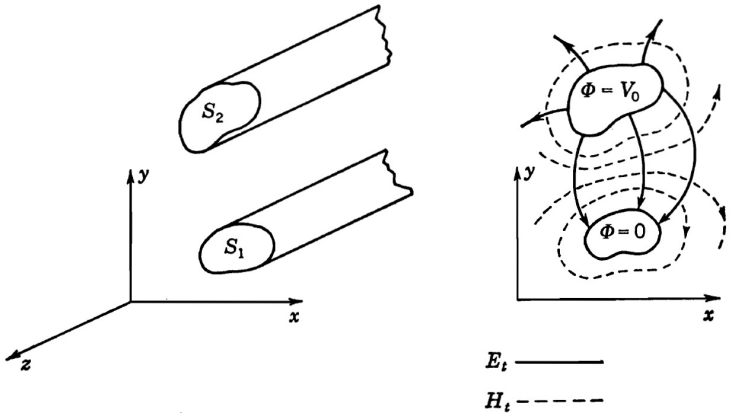


Figure 3.4: Ideal two-conductor transmission line.

For an ideal transmission line as described, TEM propagation modes are possible, for which Maxwell's equations reduce to [42]:

$$\vec{E}_t = -\nabla_t \Phi(x, y) e^{\pm jkz} \tag{3.8}$$

$$\vec{H}_t = \mp \overline{Y} \cdot \vec{E}_t \tag{3.9}$$

where $\vec{E}_t$ and $\vec{H}_t$ are the transverse electric and magnetic field, respectively, $k = 2\pi/\lambda$ is the wave number, $\nabla_t$ is the transverse nabla operator and $\overline{Y}$ is the dyadic wave admittance matrix. The last two terms are defined as:

$$\nabla_t = \hat{x}\frac{\partial}{\partial x} + \hat{y}\frac{\partial}{\partial y} \tag{3.10}$$

$$\overline{Y} = Y(\hat{y}^T \hat{x} - \hat{x}^T \hat{y}) \tag{3.11}$$

where $\hat{x}, \hat{y}$ are the unit vectors in the transverse plane and $Y = \sqrt{\epsilon/\mu}$ is the intrinsic admittance of the medium surrounding the conductors. The negative sign in Eq. (3.8) is added only to respect the convention that E-field lines travel from higher to lower potentials. The potential function $\Phi$ is a solution of Laplace's equation in the $xy$ plane. Solutions exist only if the two conductors are at different potentials. In an electrically neutral system, one of the conductors could be assumed to be at a potential of $+V_0/2$ and the other one at $-V_0/2$. However, according to Eq. (3.8), the field $\vec{E}_t$ is invariant to the addition of a constant to $\Phi$. The conductor $S_1$ can then be assumed to be at a zero potential and $S_2$ to a $V_0$ potential. In the transverse plane, $\nabla_t \times \vec{E}_t$ is zero by identity, which causes the line integral of $\vec{E}_t$ from $S_1$ to $S_2$ to be unique and independent from the integration path. As

the integration is performed in the transverse plane, the dependency of $z$ can be removed from $\vec{E}_t$, considering a simplified vector $\vec{e} = -\nabla_t \Phi(x, y)$. The line integration within the transverse plane is then calculated as:

$$V_0 = -\int_{S_1}^{S_2} \vec{e} \cdot d\vec{l} = \int_{S_1}^{S_2} \nabla_t \Phi \cdot d\vec{l} = \int_{S_1}^{S_2} d\Phi = \Phi(S_2) - \Phi(S_1) \tag{3.12}$$

resulting in a unique voltage wave $V$ associated with the transverse electric field wave $\vec{E}_t = -\nabla_t \Phi(x, y) e^{-jkz}$ given by:

$$V = V_0 e^{-jkz} \tag{3.13}$$

As $S_1$ and $S_2$ are assumed to be perfect conductors, the normal component of $\vec{e}$ will be discontinuous at the conductor surfaces, therefore a surface distribution of charge given by $\rho_s = \epsilon \hat{n} \cdot \vec{e}$ will exist on the conductors, being $\hat{n}$ the unit outbound normal vector from the conductors. For the same reason the tangential magnetic field is discontinuous at the surface of the conductors, originating a surface current density on them:

$$\vec{J}_s = \hat{n} \times \vec{H}_t \tag{3.14}$$

which moves along the $z$ axis as both $\hat{n}$ and $\vec{H}_t$ are vectors in the $xy$ plane. At the conductor surfaces, the normal component of $\vec{H}_t$ and the tangential component of $\vec{E}_t$ are zero, hence, from Eqs. (3.9) and (3.14), we obtain:

$$|\vec{J}_s| = |\vec{H}_t| = Y|\hat{n} \cdot \vec{E}_t| = Y\frac{\rho_s}{\epsilon} = \frac{\rho_s}{\sqrt{\mu\epsilon}} \tag{3.15}$$

where $\rho_s$ is the surface charge density on the conductors.

The total current flowing on the conductor $S_2$ is given by the line integral around its defining curve of the current density:

$$I_0 = \oint_{S_2} |\vec{J}_s| dl = \oint_{S_2} \frac{\rho_s dl}{\sqrt{\mu\epsilon}} = Q v_c \tag{3.16}$$

where $I_0$ is the magnitude of the total axial current on $S_2$, $Q$ is the charge on $S_2$ per unit length and $v_c$ is the velocity of light in the medium surrounding the conductors, with parameters $\mu, \epsilon$. As the outbound unit normal vectors from both conductors have opposite directions, the current $I_0$ flows down the line on one conductor and back on the other. The total current on each conductor is the same, as the total charge (positive on one conductor and negative on the other one) is the same on both. Therefore, associated with the magnetic field wave $\vec{H}_t$ there is a unique current wave given by:

$$I = I_0 e^{-jkz} \tag{3.17}$$

The ratio of the potential difference between the conductors to the total current flowing on them for a wave propagating in either the $z$ or $-z$ direction is defined as the characteristic impedance $Z_c$ of the transmission line, given by:

$$Z_c = \frac{V_0}{I_0} = \frac{V_0}{Q}\sqrt{\mu\epsilon} = \frac{1}{C v_c} = \frac{\epsilon}{C} Z \tag{3.18}$$

where $Z = \sqrt{\mu/\epsilon}$ is the intrinsic impedance of the medium surrounding the conductors, and $C$ is the electrostatic capacitance between the two conductors per unit length. The characteristic impedance differs from the intrinsic (or wave) impedance by a factor which depends only on the geometry of the line. The capacitance function used in Eq. (3.18) is that for a static electric field existing between $S_1$ and $S_2$, even if $Z_c$ can be used to characterize the transmission line for any frequency of the wave, as $\nabla_t \times \vec{E}_t$ is identically zero. The fact that the parameters defining the line are only those associated with static field distributions in the transverse plane is a unique property of the ideal transmission line among wave-guiding structures [42].

#### 3.2.2.2 Impedance matching

In order to have the same amplitude in both Dirac pulses present in the impulse response of the stripline PU, the transmission lines formed by the stripline electrodes and the BPM chamber wall need to have a matched characteristic impedance. From Eq. (3.18), it is possible to work out the capacitance $C$ per unit length that a transmission line should have for its characteristic impedance $Z_c$ to be 50 Ω:

$$Z_c = \frac{1}{C v_c} \longrightarrow C = \frac{1}{Z_c v_c} \tag{3.19}$$

Given that the conductors in the transmission line section of the stripline PU are only surrounded by vacuum, $v_c = c = 3 \cdot 10^8$ m/s, which results in:

$$C = \frac{1}{Z_c \cdot c} = \frac{1}{50 \cdot 3 \cdot 10^8} = 6.6667 \cdot 10^{-11} F/m \tag{3.20}$$

A 2D electromagnetic analysis of a given cross-section geometry with the Electrostatic Solver of the CST Studio® suite [43] allows to determine its capacitance per unit length $C$. Several design iterations can be performed until finding its closest possible value to the one described in Eq. (3.20).

The PU was designed [39] with the transverse configuration shown in Figure 3.5. The blue region represents the vacuum, while the grey regions represent the four electrodes. The electrode thickness, calculated as the difference between *r_elec* and *r_pipe* in the figure, is 3.1 mm for an angular coverage $\phi$ of 45. The transmission line gap between the electrode and the BPM chamber wall is 2.4 mm, given by the difference between *r_out* and *r_elec*. These and other relevant dimensions are displayed in Table 3.1.

| Dimension | Symbol/Expression | Value |
|---|---|---|
| Pipe radius (in BPM chamber) | *r_pipe* | 12 mm |
| Electrode outer radius | *r_elec* | 15.1 mm |
| Electrode thickness | *r_elec* − *r_pipe* | 3.1 mm |
| BPM chamber radius | *r_out* | 17.5 mm |
| Transmission line gap | *r_out* − *r_elec* | 2.4 mm |
| Angular coverage | $\phi$ | 45 ° |

Table 3.1: Transverse dimensions of the compact stripline PU protoype.

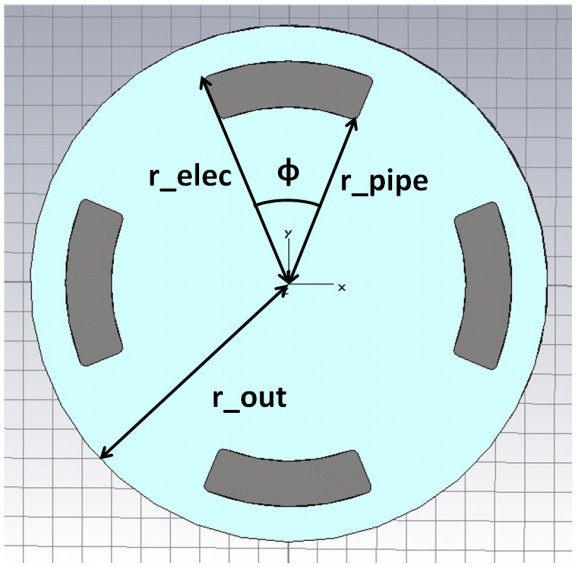


Figure 3.5: Cross-section dimensioning of a stripline PU prototype.

### 3.2.3 Damping of High-Order Modes (HOMs)

Generally, a charge bunch penetrating a structure made of non-perfect conductors, or with discontinuities, excites an electromagnetic field that acts on itself and on the next bunches in the beam train. This field describes the interaction of the charged particle beam with its environment in the time domain and is known as wakefield. It has two components: short-range wakefield, which acts on the pulse exciting it, and long-range wakefield, acting on the next bunches in the beam train. Due to imperfections of the vacuum pipe (non-perfect conductors, finite lengths, changes in the geometry of the pipe...), the electromagnetic field induced by a moving charge ceases to be contained in a perpendicular plane to the acceleration direction and starts to bend. The fields induced by the next bunches in the beam accentuate this effect.

The interaction between a charged particle beam and its environment can be described in the frequency domain by modelling each vacuum chamber component as a frequency-dependent impedance, known as the beam coupling impedance.

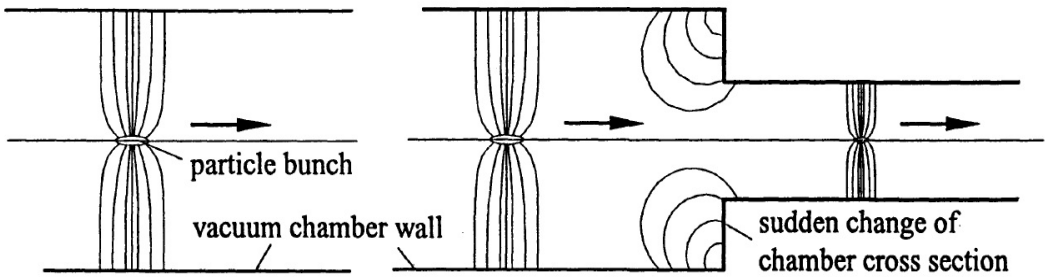


Figure 3.6: Coupling of a charged particle beam to the environment: constant (left) and variable (right) cross-section of the vacuum chamber.

Wakefields can be decomposed into their longitudinal and transverse components to the acceleration axis. The former modifies the energy of the successive beam bunches, as each one loses a part of it when traversing the field induced by its preceding bunches; the latter modifies the transverse dimensions of the beam and, if its progress is left unchecked, it may cause instability by Beam Break-Up (BBU). Additionally, gradients of potential are induced in both directions, which can be interpreted as peaks or mismatches of the longitudinal and the tranverse beam coupling impedances, given by the Fourier transform of the wake function for each direction. For these reasons, it is crucial to damp the wakefields so that these unwanted effects can be mitigated [44].

A wide variety of analytical methods to calculate the wakefields and their associated wake potentials are described in [45]. However, in this case, due to the complexity of the structure, numerical simulation software has been used to compute the electromagnetic fields. In the case of relativistic beams, a charge bunch will never be reached by the short-range wakefield it induces. Therefore, for the CLIC Drive Beam, only the effect of long-range wakefields needs to be studied. For this purpose, the PU has been modelled with the electromagnetic field simulator GdfidL [46] (Figure 3.7 from [39]). Sharp peaks of the beam impedance are observed around 12 GHz, the beam bunching frequency, both in the transverse and longitudinal directions (Figure 3.8 from [39], red trace). In order to damp the wakefields and smoothen these undesired peaks in both the transverse and longitudinal directions (Figure 3.8 from [39], blue trace), a silicon carbide (SiC) ring has been placed in the downstream end of the electrodes, in the vicinity of the short-circuit.

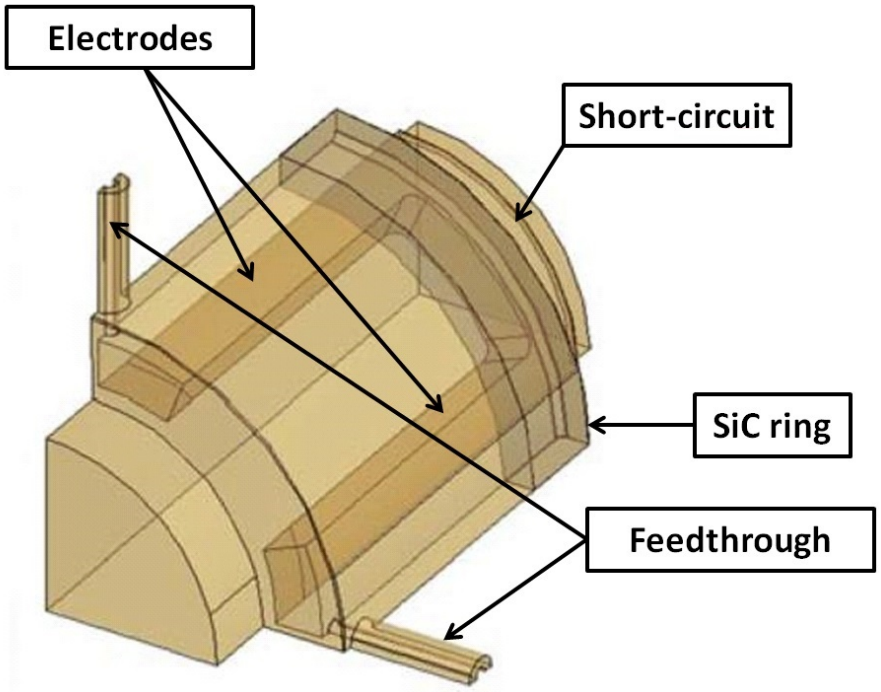


Figure 3.7: GdfidL model of the prototype stripline PU, from [39].

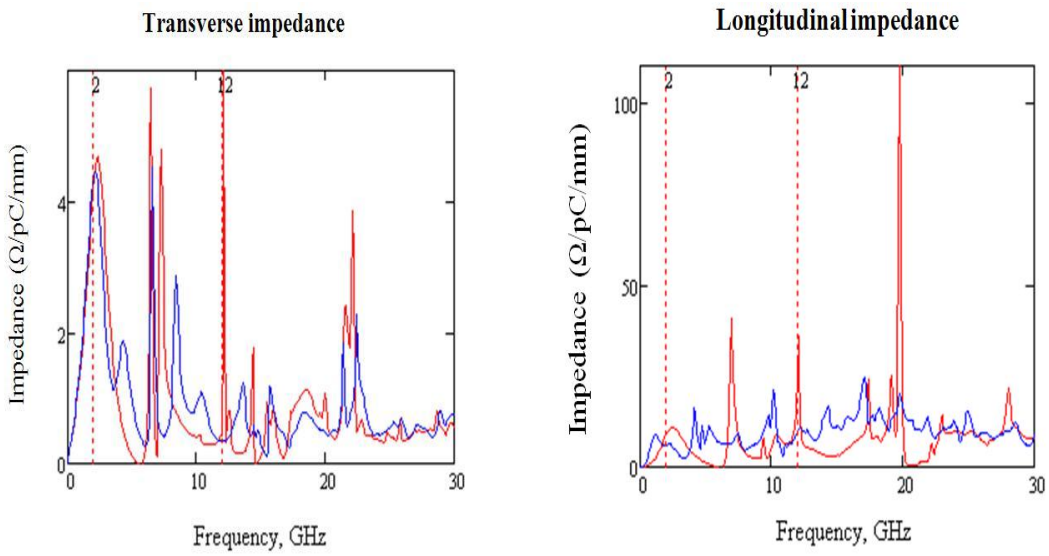


Figure 3.8: Transverse (left) and longitudinal (right) beam coupling impedance in the compact stripline PU prototype. The suppression of the impedance peaks at 12 GHz using the SiC ring (blue trace) is observed in both directions. From [39].

A longitudinal cut of the design is shown in Figure 3.9, being the most relevant dimensions detailed in Table 3.2. A gap of a certain length is needed in the upstream port, which makes the total BPM chamber longer than the electrode. The position at which the pin of the port is inserted in the electrode is given by *l_stub*.

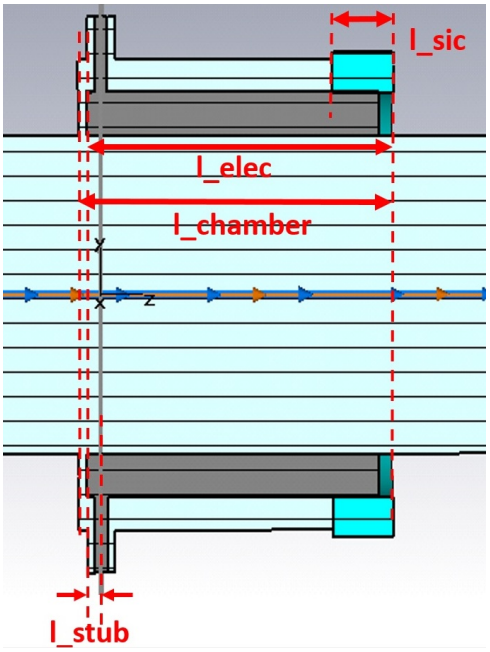


Figure 3.9: Longitudinal cut of the compact stripline PU prototype.

| Dimension | Symbol/Expression | Value |
|---|---|---|
| Electrode length | *l_elec* | 25 mm |
| Chamber length | *l_chamber* | 25.7 mm |
| Gap length | *l_chamber* − *l_elec* | 0.7 mm |
| Stub length | *l_stub* | 1.2 mm |
| SiC ring length | *l_sic* | 5 mm |

Table 3.2: Longitudinal dimensions of the compact stripline PU prototype.

### 3.2.4 Signal transmission outside the BPM body

The port signals are transported outside the structure by means of coaxial feedthroughs. They provide impedance matching, hermeticity, electrical isolation and are able to withstand the high temperature and pressure values expected in the environment. A customized version of the CeramTec® 15310-03-W model [47] has been selected. A detailed view is shown in Figure 3.10.

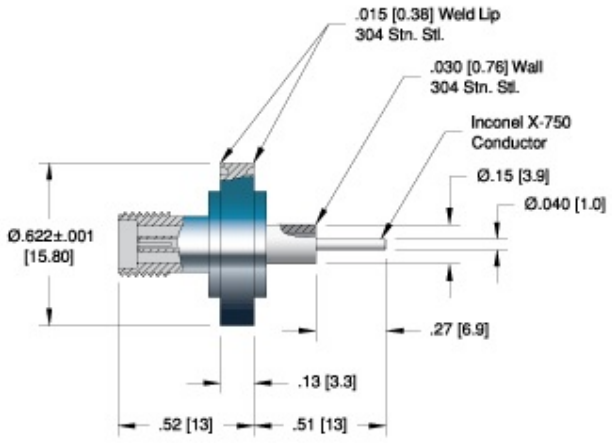


Figure 3.10: CeramTec®15310-03-W coaxial SMA feedthrough.

The electrical, thermal and mechanical properties of this feedthrough model are the following:

- 50 Ω SMA matched impedance
- Materials:
  - Housing: 305 stainless steel
  - Pin: Inconel X-750
  - Insulation: Glass ceramic
  - Flange: 304 stainless steel
  - Contacts: 300 stainless steel
- Voltage rating: 500 V DC

- Current rating: 1 A
- Temperature range: -269° C to 350° C, ISO KF -25° C to 205° C
- Pressure (at 20° C): 1400 PSIG, ISO KF 0 PSIG
- Leak rate: $< 10^{-10}$ Atm-cc/s (He)

In order to prevent perturbations of the beam, no magnetic materials have been used in the feedthrough design.

## 3.3 Mechanical design

The designed prototype stripline PU has downstream short-circuited electrodes, is compact and integrable in the vacuum chamber of the adjacent quadrupole (Figure 3.11), allowing to save space on the Drive Beam line. Its extremes are equipped with CF-63 and CF-40 flanges, being one of them rotatable to facilitate its installation. These two flanges are shown in Figure 3.12.

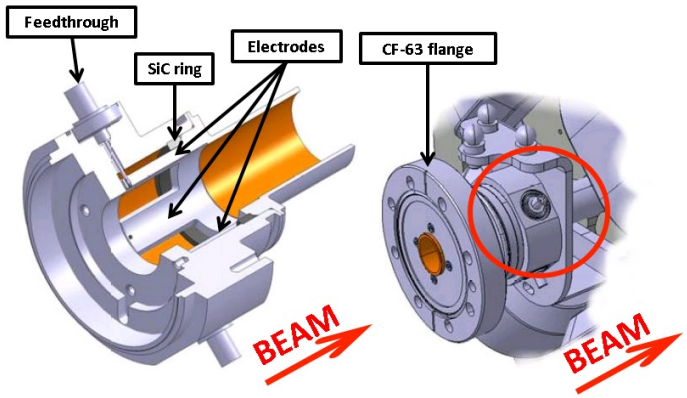


Figure 3.11: 3D views of the prototype stripline PU: longitudinal cut of the BPM body with electrode and feedthrough details (left); detail of the integration into the adjacent quadrupole (right). The left view is a zoom of the highlighted area in the right view.

The different elements of the stripline PU and its assembly are shown in detail in Figure 3.12. Firstly, on the upstream end, the CF-63 flange provides connectivity to the previous element on the CLIC Drive Beam decelerator line: a PETS. Following the CF-63 flange, a bellows has been inserted to decouple the BPM structure from possible vacuum chamber movements in other sections of the beam line. This increases the cross-section radius of the insertion region, causing additional resonances.These resonances are mitigated by the combined action of a copper RF finger installed under the bellows and two loads of SiC at the downstream end of the bellows cavity. These loads prevent the propagation of HOMs from the bellows cavity to the main BPM body and are not to be confused with the SiC ring specified in the previous section, which damps the HOMs in the main BPM chamber. In both cases, Boostec SiC 100® [48] has been used. Both CF-63 and CF-40 flanges, the bellows, the BPM body and the piece holding the electrodes have been manufactured in stainless steel, as it is a light material robust to welding. Similarly as in

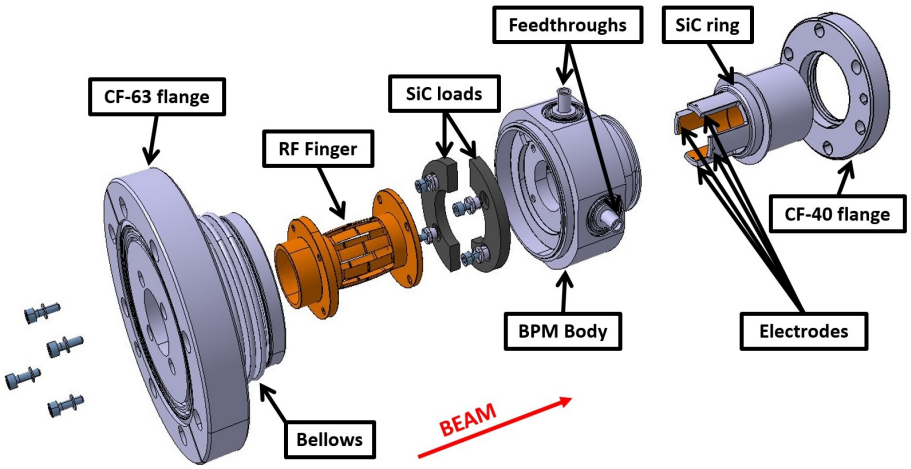


Figure 3.12: Assembly view of the compact stripline BPM prototype for the CLIC Drive Beam.

the feedthrough design, no magnetic materials have been used in order to prevent perturbations of the beam.

The electrodes have been integrated in the piece that attaches the BPM body to the CF-40 flange. They have also been manufactured in stainless steel, although a 30 $\mu$m thick copper coating has been performed over the electrodes to profit from the higher conductivity of this material. This 30 $\mu$m thickness is above the minimum required considering the skin effect on copper at the frequency of interest (12 GHz). The penetration depth $\delta$ of a given material is defined as the depth at which the current density falls to $1/e$ times its surface value. The minimum thickness of the copper coating is set by the penetration depth of copper, $\delta_{\mathrm{Cu}}$, which is given by:

$$\delta_{\mathrm{Cu}} = \sqrt{\frac{2 \cdot \rho_{\mathrm{Cu}}}{\omega_0 \cdot \mu_{\mathrm{Cu}}}} \longrightarrow \delta_{\mathrm{Cu}} = \sqrt{\frac{2 \cdot 0.0168\ \mu\Omega\mathrm{m}}{2 \cdot \pi \cdot 12\ \mathrm{GHz} \cdot 1}} = 0.5955\ \mu\mathrm{m} \tag{3.21}$$

where $\rho_{Cu}$ and $\mu_{\mathrm{Cu}}$ are, respectively, the resistivity and the magnetic permeability of copper and $\omega_0$ the angular operation frequency.

## 3.4 Stripline geometry issues

The simulated impulse response and transfer function of the compact stripline prototype design [39], with and without the SiC ring at the downstream end of the electrodes, are shown in Figures 3.13 and 3.14.

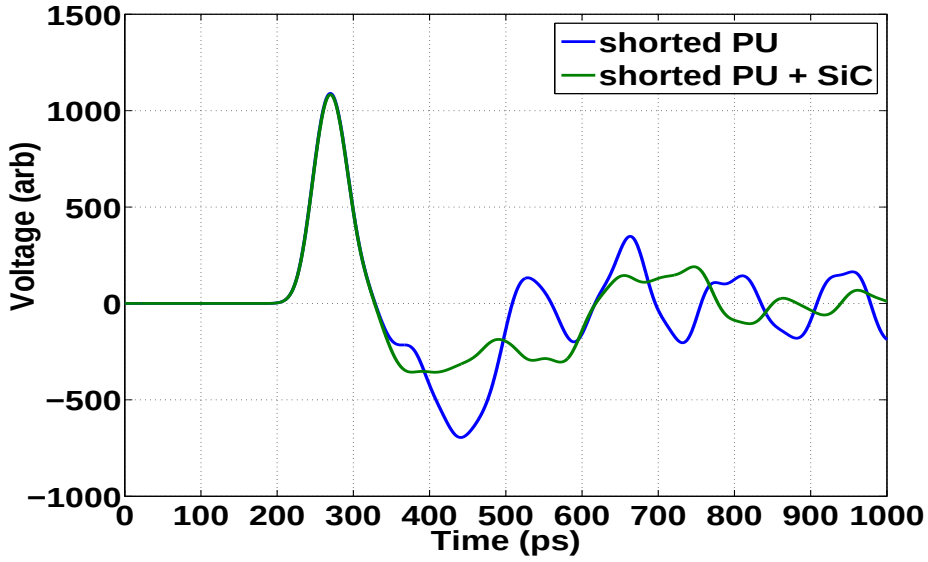


Figure 3.13: Impulse response of the compact stripline PU prototype without SiC (blue trace) and with SiC (green trace).

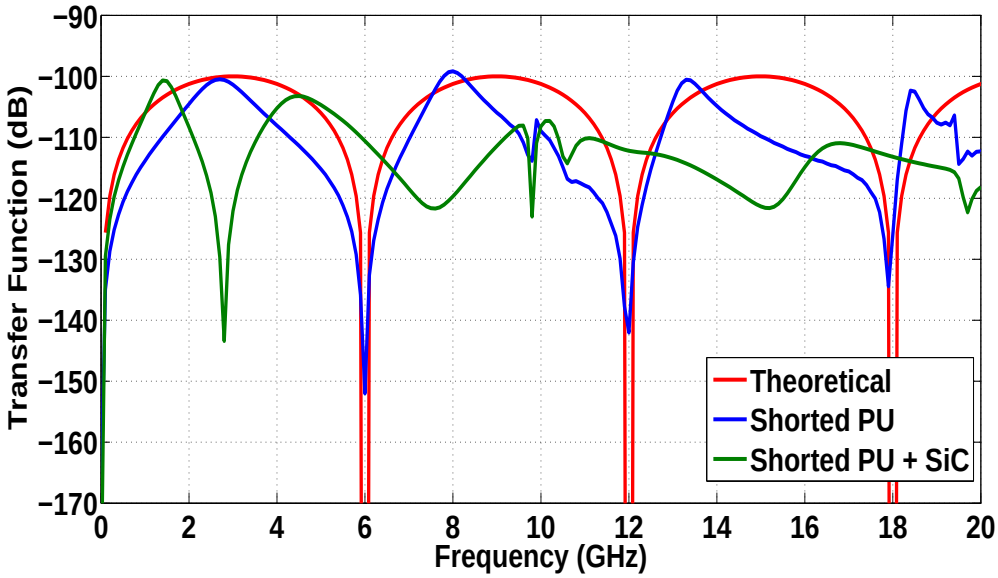


Figure 3.14: Frequency response of the compact stripline PU prototype without SiC (blue trace) and with SiC (green trace) compared to the theoretical one (red trace).

In Figure 3.13 it is possible to observe a bigger time separation between the two impulses present in the time response of the prototype with the SiC ring at the downstream end of the electrodes. This time separation is of about $\tau = 220$ ps, corresponding to an electrode length of $l = \tau c/2 = 33$ mm, instead of 25 mm. The reason for this extended electrode length is the much bigger relative electrical permittivity of the SiC compared to vacuum. This value is not constant in frequency but in the region of interest, close to 12 GHz, is of about $\epsilon_r = 13$ with a loss tangent of about $\delta = 0.2$.

In the frequency domain, Figure 3.14, this effect can be observed in the displacement towards lower frequencies of the peaks and the notches of the frequency response. Despite the remarkable distortion of all lobes, the first two non-DC notches can be seen at about $f_{z_1} = 4$ GHz and $f_{z_2} = 7$ GHz instead of the theoretically expected $f_{z_1} = 6$ GHz and $f_{z_2} = 12$ GHz, respectively.

Apart from the extended electrical length caused by the inclusion of the SiC ring, the simulated magnitude response hints at other design issues, which were studied by EM simulation [27].

The width of the 45° stripline electrodes is large with respect to its length, causing non-TEM fields. Simulations of the transfer function towards more narrow, TEM-like electrodes reduce some of the spurious resonances (Figure 3.15). Particularly, the 10° electrodes approximate the theoretical magnitude response quite well, except for one resonance around 10 GHz.

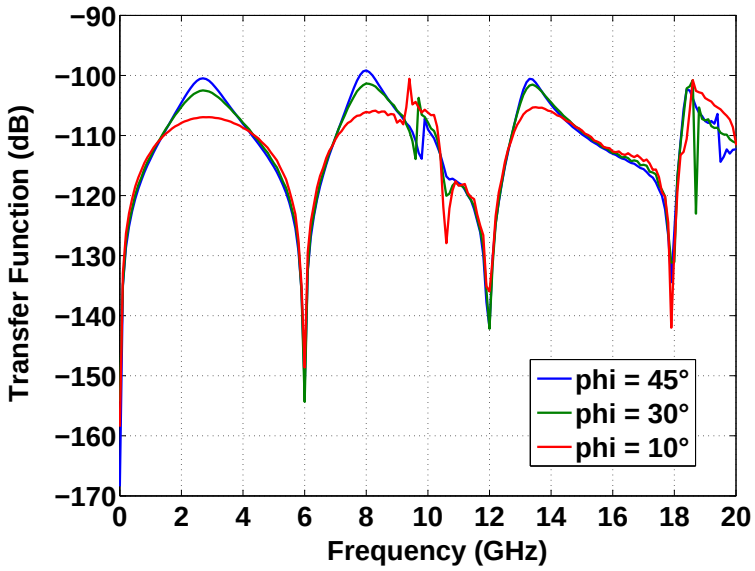


Figure 3.15: Stripline BPM transfer function for different electrode angular coverages, without SiC ring.

This unavoidable resonance seems to be caused by the $TM_{01}$ waveguide mode of the vacuum chamber. A simulation with an 11 mm aperture shifts the effect well above 15 GHz (Figure 3.16).

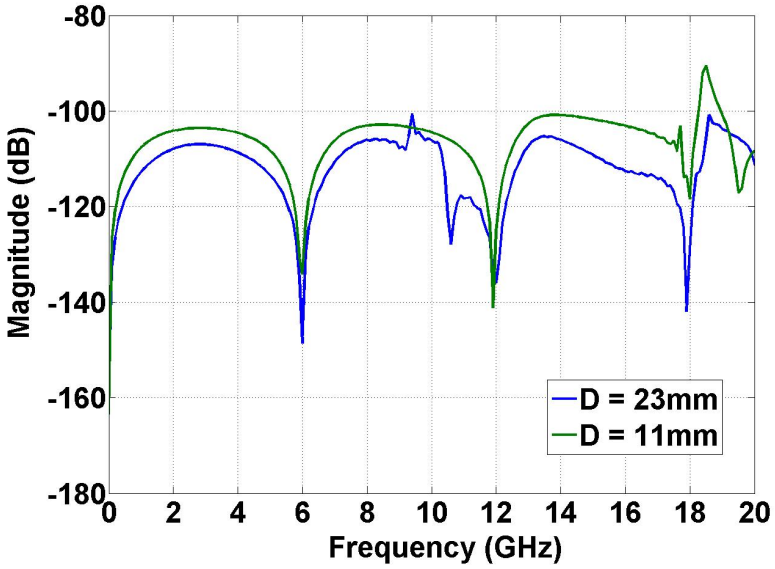


Figure 3.16: Stripline BPM transfer function for different vacuum pipe apertures.

The result of simulations to compensate the length extension effects caused by the SiC ring are shown in Figure 3.17. Any use of SiC clearly also damps the notch effect and hence optimisation to relocate the notch to 12 GHz will only be of minor benefit.

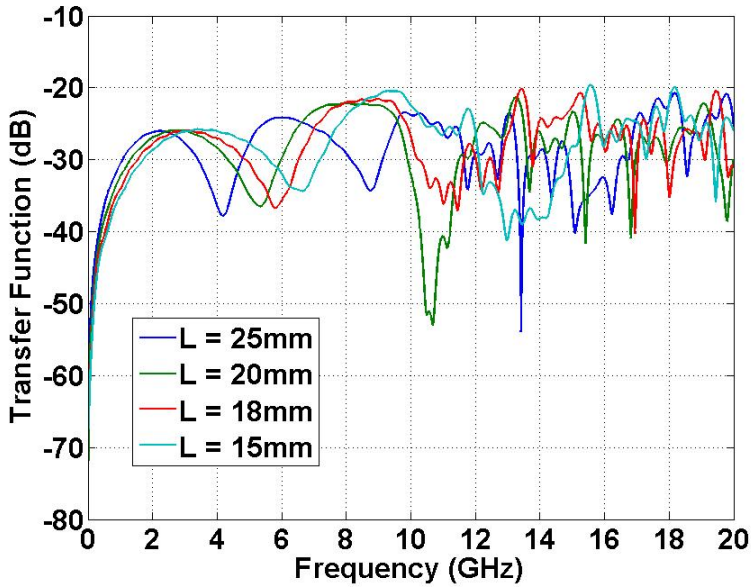


Figure 3.17: Transfer function for different electrode lengths with SiC ring.

As the transfer response of the prototype BPM has some drawbacks with respect to the design intentions (Figure 3.2, right), the expected signal response to a CLIC-like beam was analysed with an EM simulation, based on the CST Studio Particle-in-Cell (PIC) solver. As stimulus signal, a relativistic beam of 20 Gaussian bunches spaced by 83.33 ps, each one with 8.4 nC charge and 1 mm rms length, was supplied. As expected, the

time domain output signal does not show any bunch cancellation (Figure 3.18). The raw waveform recorded by a voltage monitor at the output feedthrough port shows strong high frequency signal content, particularly at 12 GHz.

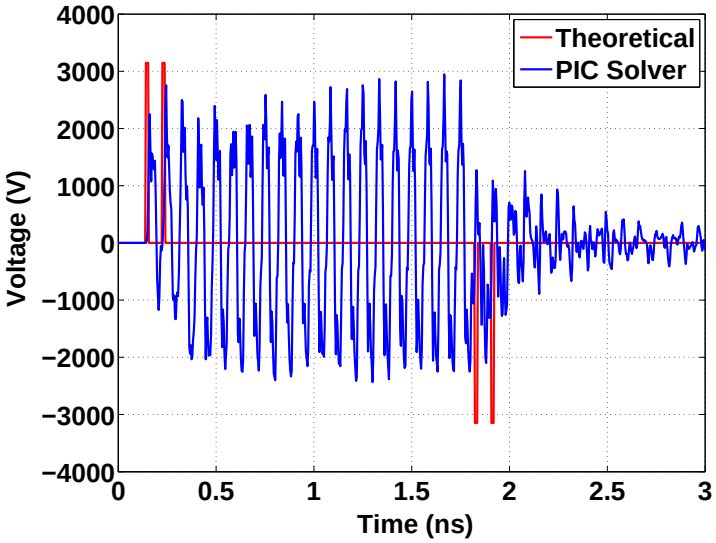


Figure 3.18: Simulated prototype stripline BPM raw output with beam.

As a conclusion of this study, modifications of the angular coverage and length of the electrodes could be suggested. Independently of the effect of the SiC ring, the lobe distortion of the stripline PU frequency response increases with the electrode angular coverage and unwanted resonances appear when the electrode length and the vacuum pipe aperture become similar. Therefore, further stripline PU developments should have narrower and longer electrodes.

# Chapter 4

# Design of an Electronic Acquisition System for the Stripline Pick-Up with Short-Circuited Electrodes

This chapter describes the design of the BPM electronic acquisition system, consisting of the analog front-end for signal conditioning (or shaping) and the digitizing stage (Figure 2.5). Section 4.1 describes the system specifications, from the necessary ones for integration into the control and acquisition system of the complete CLIC module to the different signal processing options available and a deeper study of the PU output signals. The selected structure and features for the system will be detailed in section 4.2. Section 4.3 will summarize the performance of the designed system.

## 4.1 Specifications of the electronic acquisition system

### 4.1.1 Integration into the CLIC Module control and acquisition system

As the distance between consecutive access points to the CLIC tunnel will be considerable, approximately 900 metres, a locally installed control and acquisition system is considered for each one of the CLIC modules (Figure 1.8), adapted to fit the allocated space, the only connections to the surface being mainly the power supply (230 V AC supply line) and the communications network (an optical link). One of the main challenges is the high radiation environment in which the electronic system has to perform satisfactorily.

Considering the different subsystems (Figure 1.8), between 100 and 200 control and acquisition channels are needed for each CLIC module. As each subsystem has different specifications and these can evolve, the most flexible solution is a generic digital motherboard capable of managing a number of mezzanine cards, corresponding to the subsystems.

The local electronics processes the signals coming from the different subsystems in the module, digitizes them and manages their concentration and transmission to the surface according to the GBT (GigaBit Transceiver) protocol [49], developed at CERN for high radiation environments. The GBT standard provides a 4.8 Gbps optical link comprising up to 40 local chip-to-chip links with serialization and deserialization (SER-DES)

functionalities for data concentration and allows the management of multiple synchronous clocks.

The crate hosting the CLIC Module control and acquisition system will be equipped with a service board that hosts the GBT Transceiver (GBTX) chip and a Slow Control Application-Specific Integrated Circuit (SCA). A number, still to be defined, of mother-boards are connected to a back-plane which communicates them with the service board using a chip-to-chip link, as shown in Figure 4.1.

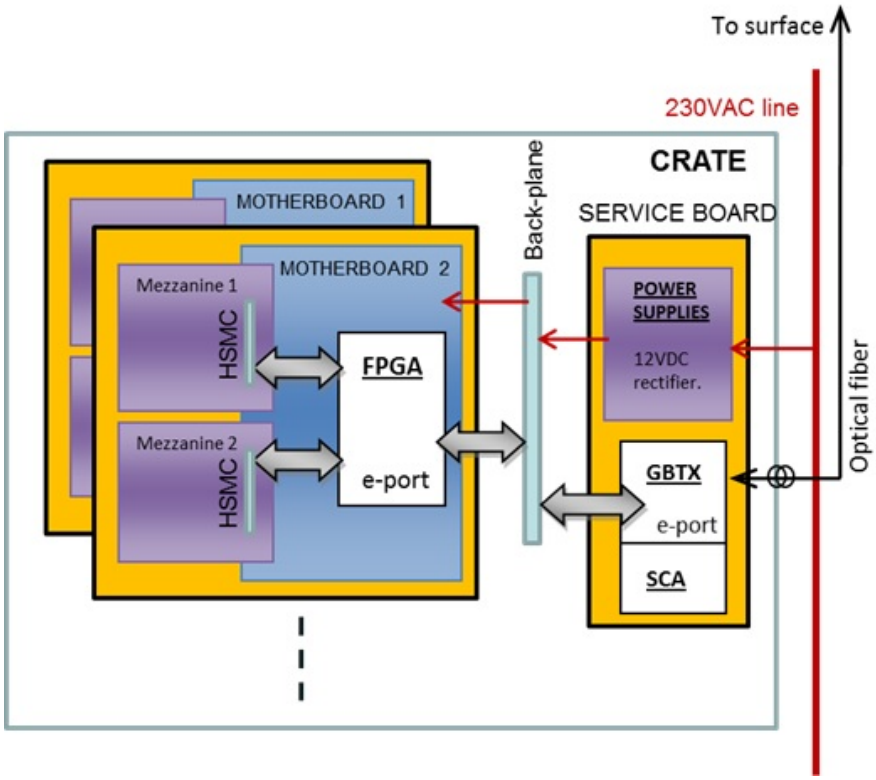


Figure 4.1: CLIC Module control and acquisition system.

The central component of the motherboard will be a Field-Programmable Gate Array (FPGA), whose role is to control the mezzanines and manage the data transfer to and from them. It also concentrates the data from the mezzanines, transmits it to the GBT chip via the back-plane and acquires the descending clock and control signals through the GBT chip.

This design for the CLIC Module control and acquisition system imposes the following guidelines on the design of the BPM electronics:

- **Radiation hardness**. Simulations of the CLIC tunnel environment [50] estimate a radiation dose higher than 1 kGy per year at the location of the electronics crate. With an expected system service life of 15 years, the electronics should resist a total radiation dose of about 15 kGy. The crate will be shielded and radiation-hard components will be selected. Analog components and Analog-to-Digital Converters (ADCs) are usually robust enough, despite not being formally considered as

rad-hard. Digital components are the most sensitive ones to radiation, although the inclusion of digital memory points in the acquisition mezzanine of the stripline BPM is not considered.

- **Power consumption**. The total power consumption of the CLIC Module electronics crate should be between 30 and 50 W, which subsequently requires maximum simplification of the electronic design of the mezzanines for the subsystems.

- **Mezzanine design**. The use of mezzanines for the subsystems facilitates the design of a general purpose motherboard. The mezzanines will be designed with state-of-the-art components and may evolve, being replaced if necessary. On the other hand, this causes the number of links to be limited by the number of connectors. It will be hence necessary to optimize the performance. Altera® High Speed Mezzanine Card (HSMC) connectors [51] will be used for this purpose, providing serial link transmission rates of up to 10 Gbps. In order to fully profit from this feature, the serial output components on the mezzanine, mainly the ADCs should also provide a high output rate.

The reception of the data in the surface is performed by PCIeX8 cards, designed to acquire the signals from 4 GBT optical links, that is, from 4 CLIC modules each.

### 4.1.2 Specifications given by the stripline technology.

• **Pulse charge in the PU time response to a centered beam:** Using the PU properties and considering a centered beam with pulses of charge Q, the current induced by the movement of one of them along a stripline electrode of length $l$ and angular coverage $\phi$ can be calculated as [15]:

$$I(t) = \frac{\phi}{2\pi} \cdot \frac{dQ}{dt}\left[\delta(t) - \delta\left(t - \frac{2l}{c}\right)\right] \tag{4.1}$$

Recalling the operation principle of a stripline PU (Figure 2.15), its response to a beam bunch with charge Q is a pair of pulses of opposed polarity, each with half the input bunch charge, multiplied by the circumference coverage ratio of the electrode. Being the CLIC Drive Beam bunch charge 8.3 nC (Table 1.1) and the electrode angular coverage $\pi/4$ *rad* in the designed PU (Table 3.1), the output pulse charge is determined by:

$$q' = \frac{1}{2} \cdot \frac{\phi}{2\pi} \cdot Q \longrightarrow q' = \frac{1}{2} \cdot \frac{1}{8} \cdot 8.3 \cdot 10^{-9} \approx 0.52\, nC \tag{4.2}$$

• **Sensitivity:** The voltage in the PU output ports depends on the position deviation of the beam from the center in each plane. For instance, the image current captured by the right electrode in Figure 2.5 can be expressed as [15]:

$$I_e = -I_b \cdot \frac{2}{\pi} \cdot \arctan\left[\frac{\left[\left(1 + \frac{x}{R}\right)^2 + \left(\frac{y}{R}\right)^2\right] \cdot \tan\left(\frac{\phi}{4}\right)}{1 - \left(\frac{x}{R}\right)^2 - \left(\frac{y}{R}\right)^2}\right] \tag{4.3}$$

where $I_b$ is the beam current, $\phi$ the electrode angular coverage, $x$ and $y$ the beam displacements on each plane and $R$ the radius of the vacuum pipe.

In order to estimate the sensitivity of the PU, its response to the maximum foreseen deviation of the beam, half the radius of the vacuum pipe (R/2 = 6 mm) must be analysed. The strongest signal values will be obtained when the maximum deviation is aligned with one of the axes. Thus, for y=0 and $\phi = \pi/4$, (4.3) becomes:

$$I_e = -I_b \cdot \frac{2}{\pi} \cdot \arctan\left[\frac{\left(\left(1+\frac{x}{R}\right)^2\right)\cdot \tan\left(\frac{\pi}{16}\right)}{1-\left(\frac{x}{R}\right)^2}\right] \tag{4.4}$$

According to (4.4), the value of the image current is calculated for the following cases:

- For a centered beam (x=0), $I_e = -0.125 \cdot I_b$, as implied by the fact that the electrode covers one eighth of the circumference.
- For a beam located at x=R/2, the current is maximum: $I_e = -0.344 \cdot I_b$.
- For a beam located at x=-R/2, the current is minimum: $I_e = -0.042 \cdot I_b$.

The current in the closest electrode to the beam when it is maximally deviated is 2.75 times the measured current in the same electrode for a centered beam. The current in the most distant electrode to the beam when it is maximally deviated is 1/3 times the measured one for a centered beam. The relationship between the maximum and the minimum current values is then 8.25 .

The beam position is normally extracted using the ratio between the difference $\Delta$ and the sum $\Sigma$ of the measured voltages on the electrodes of each plane. Expression (4.4) can be simplified assuming a small deviation ($x \to 0$) :

$$I_e = -I_b \cdot \frac{2}{\pi} \cdot \arctan\left[\frac{(R+x)\cdot \tan\left(\frac{\pi}{16}\right)}{R-x}\right]. \tag{4.5}$$

For x$\to$ 0, $\arctan(x) \simeq x$, resulting in:

$$I_e = -0.125 \cdot I_b \cdot \frac{R+x}{R-x}. \tag{4.6}$$

$$V_r = Z_0 \cdot I_e(x); V_l = Z_0 \cdot I_e(-x)\ . \tag{4.7}$$

Considering $\Delta = V_r - V_l$ y $\Sigma = V_r + V_l$:

$$\frac{\Delta}{\Sigma} = \frac{4Rx}{2R^2+2x^2}\ . \tag{4.8}$$

For $x << R$, we obtain:

$$\cdot\frac{\Delta}{\Sigma} = \frac{2x}{R}\ . \tag{4.9}$$

The previous operations shows that, for small deviations of the beam around the center, the response is linear, as described by:

$$x = \frac{R}{2} \cdot \frac{\Delta}{\Sigma}\ . \tag{4.10}$$

Comparing with expression (2.10) and assuming a negligible electrical offset $EOS_x$, the

obtained sensitivity is the following:

$$X = \frac{1}{S_x} \cdot \frac{\Delta}{\Sigma} + EOS_x \longrightarrow \frac{1}{S_x} = \frac{R}{2} = 6\ \text{mm} \longrightarrow S_x = 0.166\ \text{mm}^{-1} \tag{4.11}$$

where the undertaken operations are analogous for the vertical plane, so, $S_y = 0.166\ \text{mm}^{-1}$.

These calculations do not consider possible gain mismatches between the electronic acquisition chains for both electrodes, which would result in a non-zero offset and a change in the sensitivity.

• **Resolution:** It is generally understood as the ability to measure small displacements of the beam, as opposed to its absolute position. Thus, it represents the minimum displacement or beam position variation the PU can detect. Typically, the resolution value of a system, specifically of a PU, is much better (lower) than the accuracy, being the accuracy as low as the resolution for the best performance case, which will be eventually limited by the noise floor in the whole system, the PU and the readout and acquisition electronics.

Although the system response can be assumed linear for small deviations, the measured value depends on the gains of the electronic acquisition chains for the opposed electrodes of each plane. The architecture allows gain optimization so that the closest electrode to a deviated beam can cover as much ADC dynamic range as possible. However, for this reason, this range will not be covered in the most distant electrode, resulting in a degraded resolution as the deviation increases. A decision has been made to acquire the electrode signals via the analog readout chain but to avoid processing $\Delta/\Sigma$ before digitization. This ratio will be processed via software or, in the future, in the FPGAs present in the electronic crate of the CLIC module.

The position resolution can be found for any deviation on each axis ($x$ or $y$, being $V_r$, $V_l$, $V_u$ and $V_d$ the electrode voltages) using standard error calculation. As the beam position depends on $\Delta$ and $\Sigma$ (Eq. (4.10)), the combined standard error $\epsilon_x$ in its measurement is calculated as follows:

$$\epsilon_x = \sqrt{c_\Delta^2 \cdot \epsilon_\Delta^2 + c_\Sigma^2 \cdot \epsilon_\Sigma^2} \tag{4.12}$$

where:

$$c_\Delta = \frac{\partial x}{\partial \Delta}\ ;\ c_\Sigma = \frac{\partial x}{\partial \Sigma} \tag{4.13}$$

Using Eq. (4.10) in Eq. (4.12) and Eq. (4.13) results in:

$$\frac{\epsilon_x}{x} = \sqrt{\left(\frac{\epsilon_\Delta}{\Delta}\right)^2 + \left(\frac{\epsilon_\Sigma}{\Sigma}\right)^2} \tag{4.14}$$

where $\Delta = V_r - V_l$, $\Sigma = V_r + V_l$, obtaining:

$$\Delta = V \cdot \left(1 - \frac{V_l}{V_r}\right)\ ;\ \Sigma = V \cdot \left(1 + \frac{V_l}{V_r}\right) \tag{4.15}$$

where V is the ADC input voltage. The resulting position error is given by:

$$(\epsilon_x)^2 = 2x^2 \cdot \frac{(\epsilon_V)^2}{V^2} \cdot \left( \frac{1}{\left(1 - \frac{V_l}{V_r}\right)^2} + \frac{1}{\left(1 + \frac{V_l}{V_r}\right)^2} \right) \tag{4.16}$$

Substituting values of $x$, the resolution can be calculated for any position in the horizontal axis. For a centered beam ($x$=0) the obtained error is as follows:

$$\epsilon_x = \frac{R}{2\sqrt{2}} \cdot \frac{\epsilon_V}{V} \tag{4.17}$$

This calculation is analogous for the vertical axis, resulting in the same dependence for $\epsilon_y$.

The final value of the position resolution depends on the acquisition dynamic range. With a pipe radius of 12 mm and a specified resolution of 2 $\mu$m for a centered beam, $\epsilon_V/V = 1/2121$ or, in dB, a SIgnal to Noise And Distorsion ratio (SINAD) of 67 dB. Recalling the relationship between them:

$$\text{SINAD} = 6.02 \cdot \text{ENOB} + 1.76 \tag{4.18}$$

the obtained Effective Number Of Bits (ENOB) is 10.7 . To keep this resolution when the deviation is at its maximum, the SINAD needs to be increased 2.75 times, obtainig finally a specified SINAD of 75.3 dB, corresponding to an ENOB of 12.2 .

As the actual electrode response is not a linear function of the deviation (see Eq. (4.3)), the resolution will not be constant in the considered deviation variation range. For each value of the deviation, the dynamic range of the ADC will determine the resolution.

• **Accuracy:** Accuracy is the ability to determine the position of the beam relative to the device being used for measuring the beam position. This is limited by some combination of pick-up nonlinear response to displaced beams, mechanical alignment errors, mechanical tolerances in the beam detection device, calibration errors in the electronics, attenuation and reflections in the cables connecting the pick-up to the electronics, electromagnetic interference, and circuit noise. Signal processing introduces additional inaccuracies such as the granularity of the Analog-to-digital Converters (ADC) given by its number of resolution bits determining the quantization step through the Least-Significant-Bit (LSB). All these effects are reflected in the position measurement errors usually having a random gaussian distribution.

The specified accuracy or precision needed in the position measurement of the CLIC DB is 20 $\mu$m, a value 10 times bigger than the specified resolution. Even with a sufficiently high ENOB for the ADC, the accuracy may be tipically limited by integral nonlinearities, different drifts and common mode due to gain mismatch between channels. These two factors can be corrected through calibration. Concerning the integral nonlinearities, the currently used ADCs have a better linearity than 3.3 bits (factor 10).

Calculating $\Delta/\Sigma$ from expression 4.4 and comparing the result with expression (4.10), it is possible to represent the theoretical against the estimated positions (Figure 4.2) and determine where they separate more than $\pm$10 $\mu$m. An accuracy of around 20 $\mu$m is obtained for a 0.6 mm deviation from the center. The accuracy requirement is hence only met for a 10% of the considered deviation range. For this percentage to be increased, the position needs to be calculated without approximations, taking into account the nonlinearity of the electrode response.

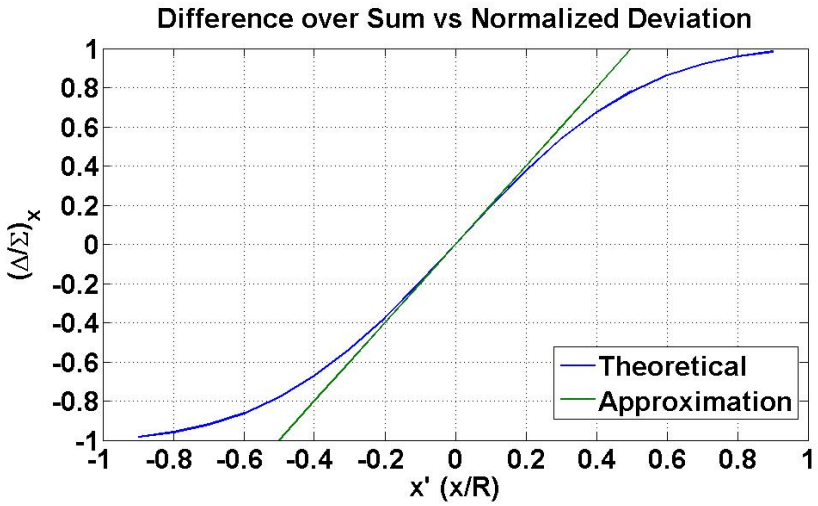


Figure 4.2: Theoretical and estimated normalized positions for a stripline PU.

### 4.1.3 Signal processing

The most frequently used technique in BPMs is to process the PU signals at the beam bunching frequency and downconvert them to lower frequency bands before transmission. In the CLIC Drive Beam, this is, however, not possible due to the PETS interfering signal at 12 GHz, which propagates along the vacuum pipe (whose cut-off frequency is $f_c$ = 7.6 GHz) to the BPM and perturbs the position measurement.

The considered alternative is base-band signal processing. For a pulse train length of 242 ns, a 4-40 MHz processing window provides adequate signal levels despite being close to a minimum of the PU transfer function, given the CLIC Drive Beam high current values. A good signal-to-noise ratio is necessary at low frequencies for a correct operation of the system, being this another reason for the choice of a stripline PU rather than a button-type one.

The PU output signals are very intense and narrow, which makes it necessary to stretch their energy in time using an analog filtering/shaping scheme before digitization. The selected solution is integrating the signal by means of low-pass (LP) filters. Considering the system operation frequencies, these filters will have to be implemented with lumped elements. After digitization, the position signal is extracted by processing $\Delta/\Sigma$ via software or, in the future, in the FPGAs present in the CLIC module.

As its transfer function is proportional to a sine, the PU behaves as a differentiator or a high-pass (HP) filter at low frequencies ($\sin f \simeq f, f \to 0$). In this band, the amplitude of the response increases with frequency. In order to obtain a proper time resolution, the time constants of the filters must be selected so that they allow the first pair of pulses in the PU time response to be integrated before the arrival of the second pair of pulses (242 ns afterwards). A combination of filters that performs this task is the following: a first-order low-pass (LP) filter at 4 MHz, a first-order LP filter at 20 MHz and a second-order LP filter at 35 MHz. The frequency response of the complete system, PU and filter chain, is shown in Figure 4.3. The placement order of each filter in the analog chain does not alter its final frequency response, although a particular implementation will be presented and discussed in section 4.2.

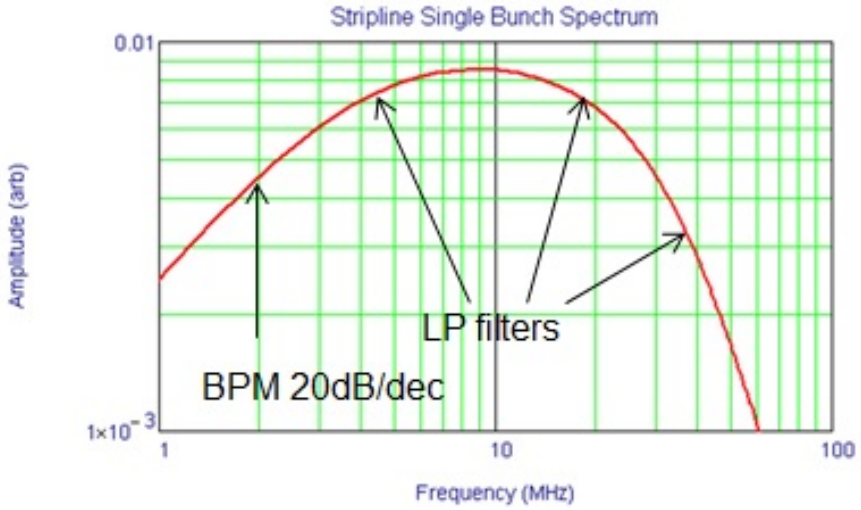


Figure 4.3: Transfer function of the complete system, showing the contribution of all stages: PU (rise at low frequencies), first order low-pass filters at 4 MHz and 20 MHz and second-order low-pass filter at 35 MHz.

Impedance matching is also essential to avoid reflections, as they could travel back to the PU, causing signal interpretation problems. In addition, a 4 pF capacitance is estimated for the feedthrough, which adds a new pole at 800 MHz. This will be the first filtering in the signal path, where the charges from the PU begin to be integrated and the input voltage limited. For these reasons, impedance matching should needs to be specified up to, at least, 800 MHz for the whole analog readout chain.

The nominal CLIC Drive Beam configuration consists of 121 sectors of 24 pulses each, with a bunching frequency of 12 GHz. Starting at only one pulse per sector, the beam is combined in a multi-stage process until having 24 pulses per sector. The different beam configurations have to be analysed in order to determine the maximum and minimum input signal levels to the electronics. The position resolution is only specified in the CDR [4] for the nominal beam configuration with a value of 2 $\mu$m. However, once the components of the system have been chosen, the position resolution will be calculated for several intermediate configurations.

The obtained values for the charge of each pulse in the time response of the PU (Figure 2.15) are the following, depending on the direction of the deviation:

- The pulse charge in the time response to a centered beam is 0.52 nC (Eq. (4.2)).
- In the closest electrode to a maximally deviated beam, the charge is $2.75 \cdot 0.52$ nC = 2.86 nC.
- In the most distant electrode to a maximally deviated beam, the charge is $\frac{1}{3} \cdot 0.52$ nC =0.344 nC.

If a deviation occurs in the middle of the beam pulse train, the time response is different, as shown in Figure 4.4. When the deviation starts, it is important to note another pair of pulses with charge 2.75-1=1.75 times the pulse charge in the response to a centered beam, as it is partially cancelled with the inverted and delayed version of the previous

pair of pulses. Similarly, a pair of negative pulses with this charge value will be present when the deviation finishes, followed by the pair of negative pulses indicating the end of the train.

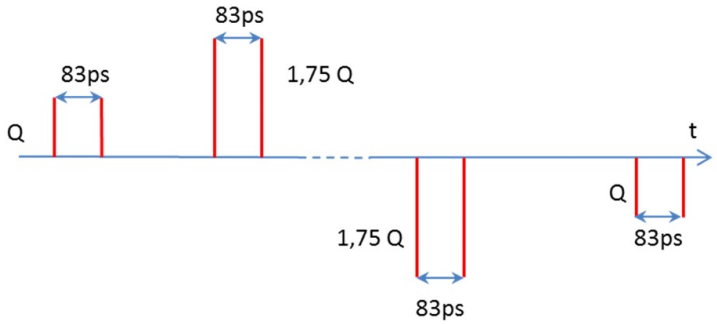


Figure 4.4: Stripline pick-up time response to a beam with a deviation in the middle of the pulse train.

After the acquisition and digitization of the electrode signals, the position signal is obtained by deconvoluting the acquired waveform with the impulse response of the complete system (PU and analog readout chain). For this purpose, as single-bunch operation is not considered in the Drive Beam, a theoretical transfer function will be used, corrected with a precise calibration.

## 4.2 Electronic architecture.

The simplest possible architecture will be used for the system: analog lumped-element filters with good impedance matching, an ADC driver and the ADC.

### 4.2.1 Selection of the ADC.

As discussed in the previous section, there are several constraints in the design of the mezzanine for the BPM. The main one is the limited number of links between the mezzanine connectors and the motherboard(s) of the electronic crate in the CLIC module. The chosen solution for an optimized performance is to consider high output data rate connectors. The type with the currently highest rate is HSMC. For each BPM, it is necessary to acquire the signals from 4 electrodes. Therefore, 4 digitization channels are needed per BPM.

Another important aspect to consider is the jitter in the ADC clocks, as well as limiting the gain dispersion between the BPM electrode channels. This dispersion is due to the presence of common mode in the measurement of the deviation. For these reasons, an adequate choice is a 'quad ADC' (4-channel ADC). It has further advantages, such as a single clock signal, single control and a lower power consumption.

The acquisition will have to be synchronous with the accelerator timing and the specified time resolution is 10 ns [4]. As the currently used data rates in the CLIC Test Facility 3 (CTF3) are 96 MSample/s and 192 MSample/s, the selected ADC will need to support, at least, one of these rates.

A specified ENOB of 12.2 (75.3 dB) for frequencies up to 35 MHz determines a maximum ADC jitter of [52]:

$$T_j = \frac{1}{2\pi \cdot BW \cdot 10^{\frac{\text{SINAD}(dB)}{20}}} \longrightarrow T_j = \frac{1}{2\pi \cdot 35 \cdot 10^6 \cdot 10^{\frac{75.3}{20}}} = 0.8\ ps. \tag{4.19}$$

where BW is the bandwidth of the system.

Taking into account the previous considerations, the ADC LTC2174-14 by Linear Technology® [53] is selected, as it reaches a good compromise between dynamic range, power consumption, architecture and sampling rate. Its mean features are simultaneous 4-channel sampling (14 bits), 73 dB SINAD (11.8 ENOB), configurable sampling rate of up to 125 MSample/s, low power consumption (450 mW with 1.8 V supply), serial LVDS (Low-Voltage Differential Signalling) outputs, selectable input range (1 Vpp y 2 Vpp), 800 MHz sample and hold frequency bandwidth (Full Power) and a sampling jitter of 0.15 ps.

The number of units of this ADC that can be implemented per mezzanine is two. Therefore, a mezzanine will be needed for every two BPMs. The sampling rate will be configured to 96 MHz for synchronization with CTF3.

The analog inputs are differential, with a selectable range between ±1 Vpp o ±2 Vpp. For a nominal beam, it will be necessary to attenuate the signals to prevent the saturation of the ADC. For this reason, the selection of the ±2 Vpp range allows to limit the noise figure. For the lowest charge beam configurations, the ±1 Vpp can be used.

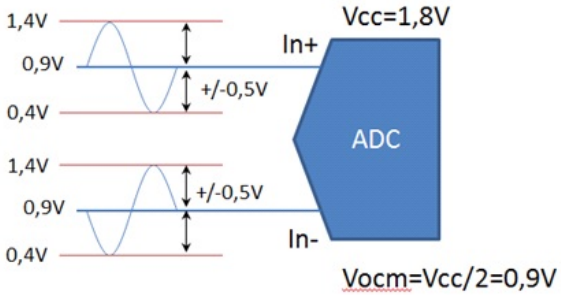


Figure 4.5: Input, supply and common-mode voltage diagram for the ADC *LTC2174* by *Linear Technology*.

The signal will have to be converted from single to differential mode, with a 0.9 V common-mode voltage. Its range of values will be from 0.4 V to 1.4 V. The use of a differential ADC driver amplifier allows to change the DC component, maintain linearity and convert the signals from single to differential mode.

A 2 Vpp dynamic range with 11.8 ENOB corresponds to the following ADC input noise:

$$\frac{Vpp}{\sqrt{12} \cdot 2^{ENOB}} \longrightarrow \frac{2}{\sqrt{12} \cdot 2^{11.8}} = 162\ \mu Vrms \tag{4.20}$$

### 4.2.2 Estimated resolution.

The SINAD value given by the manufacturer, 73 dB, corresponds to an ENOB of 11.8. In laboratory tests of the ADC, an ENOB of 11.7 was measured, which is a good result, close to the announced value. Using this value and Eq. (4.16), the resulting dependency of the resolution on the normalized beam deviation (by the radius, R) with respect to the center is shown in Figure 4.6.

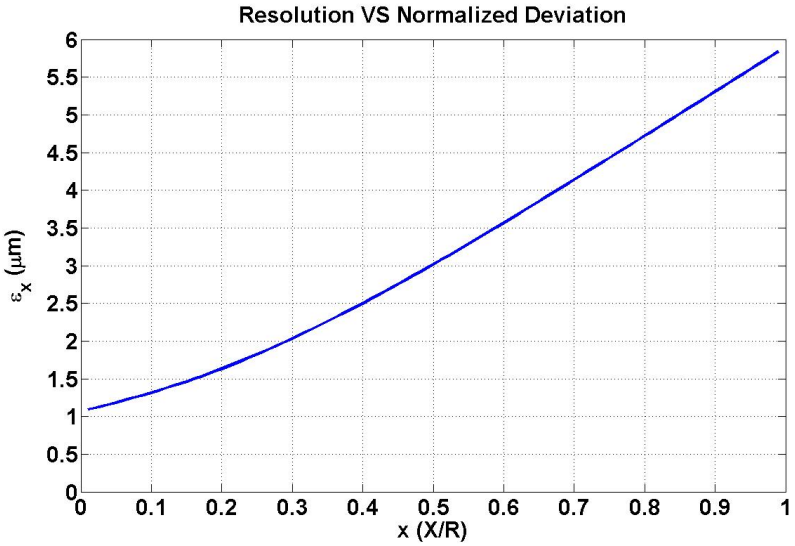


Figure 4.6: Dependency of the position resolution on the normalized beam deviation with respect to the center.

In order to achieve a 2 $\mu$m resolution for a deviation of R/2, the necessary ENOB is 12.2 bits. With the selected ADC, the ENOB is 11.7 bits, 0.5 bits are lost. Despite this, the resolution value for $x$=0.5 (X=R/2) is not much worse: 3 $\mu$m.

For a centered beam, the resolution is 1.1 $\mu$m if the signals are correctly scaled to the ADC input range. This will normally be the case, with possible exceptions with the initial beam configurations, which have the lowest charge values.

It can also be reasonably assumed that future ADC generations will reach better values of resolution and sampling rate. In any case, the selected architecture will not limit the performance of the system in the future, as HSMC connectors support up to 10 Gbps rates with a maximum jitter of 0.2 ps. With these values, the sampling will be limited to an 87 dB SINAD, 14.2 bits ENOB.

### 4.2.3 Signal shaping and ADC driving stages.

In this subsection, the implementation details of the necessary filters for the signal shaping scheme described in the previous section are presented. The ADC driver amplifier stage, where the single to differential mode conversion is performed, is also described. A block diagram of the complete acquisition system is shown in Figure 4.7, indicating the order of each filter and the selected structure for its implementation.

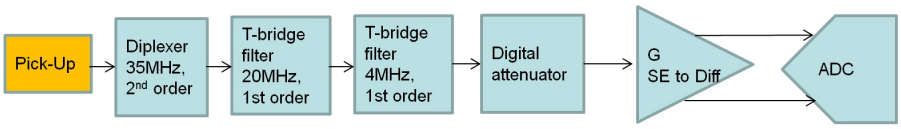


Figure 4.7: Block diagram of the analog readout chain.

#### 4.2.3.1 Input filters

The input filters will be passive and implemented with lumped elements so that the input impedance of the system is 50 Ω-matched up to, at least, 800 MHz, the cut-off frequency of an additional low-pass filter introduced by an estimated capacitance of 4 pF for the vacuum feedthrough (first parallel capacitor in Figure 4.8). The frequency response of the shaping filters will be of Butterworth type to prevent stability issues.

The first element of the chain is the second-order low-pass filter at 35 MHz, which has been implemented as an input diplexer. Two LC branches are connected in parallel: a high-pass branch, which is left loaded with 50 Ω, and a low-pass branch through which the signal path continues.

The first-order low-pass filters have been implemented as "T-bridge" structures, as they provide a wider matching bandwidth. The first one to be implemented is the 20 MHz filter, followed by the 4 MHz filter. The schematic of the filtering stage is shown in Figure 4.8.

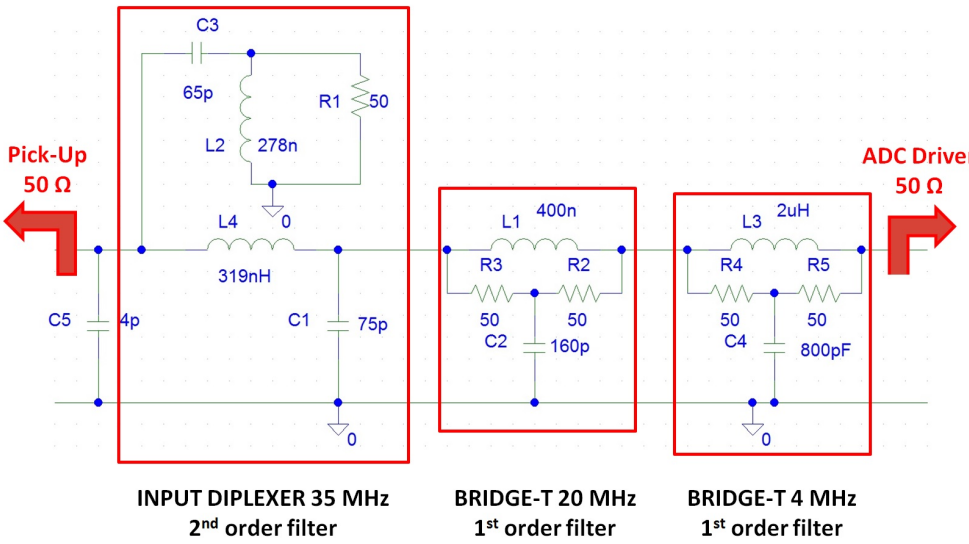


Figure 4.8: Signal shaping stage with lumped element passive filters.

In order to characterize the filter chain in the time domain, a PSPICE® simulation has been performed, modelling the charge pulses at the beginning and at the end of the PU time response to a centered beam. The CLIC Drive Beam charge pulses can be modelled as square current pulses of 10 ps ($\sim 3\sigma$) width and an amplitude of 0.52 nC/10 ps = 52 A. This will be the input signal to the electronics. The output of each filter is shown in Figure 4.9, where it is possible to note the signal being widened in time and its peaks

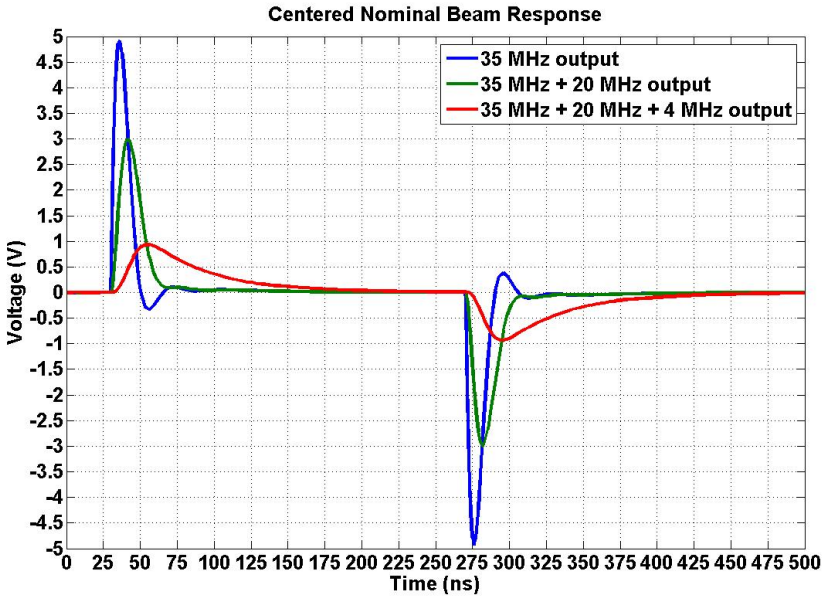


Figure 4.9: Output signals of the passive filters in the adquisition system.

smoothened by the succesive filtering stages. This confirms that the selected shaping window is correct.

For a nominal centered beam, the amplitude of the filter output signal is around 900 mVp. The output signals for the rest of considered beam configurations in the combination process are represented in Figure 4.10.

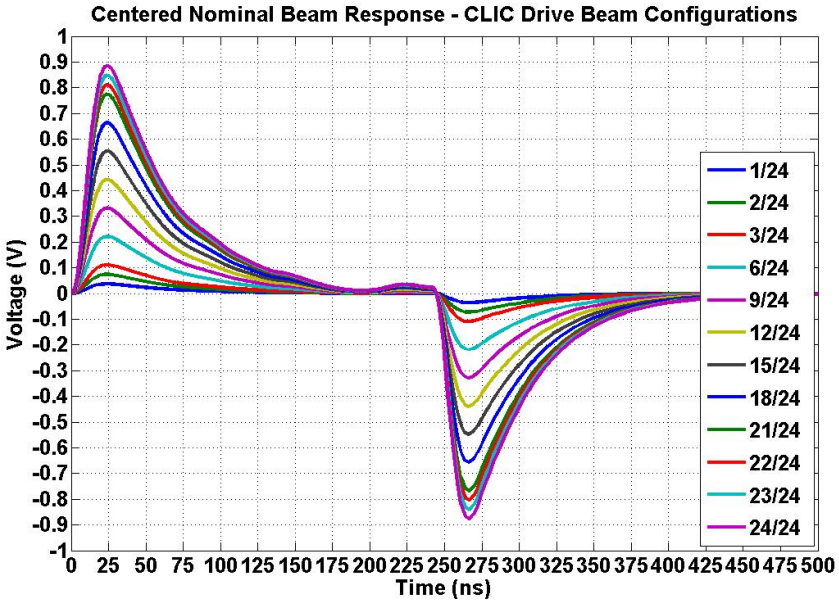


Figure 4.10: Output signals of the passive filters in the acquisition system for all foreseen CLIC Drive Beam configurations (centered beams).

Amplitudes between 37 mV and 900 mV have been obtained. If the resolution is to be maintained, these signals must be adapted to the ADC dynamic range regardless the beam configuration that induces them. This implies that the signals induced by the lowest charge beams need to be amplified. On the other hand, for a maximum deviation of R/2 = 6 mm, the amplitudes in the time response to a centered beam multiply by 2.75, as seen in the previous section. As the filtering stage response is linear, the output voltage of the channel corresponding to the closest electrode to a maximally deviated beam will be $0.9 \cdot 2.75 = 2.5$ V. In this case the signal needs to be attenuated.

For the purpose of adapting the signals induced by all possible beam configurations to the ADC dynamic range, a controllable attenuator and a gain constant in the ADC driving stage can be considered. In this case, the constraint will be the achievable SNR with this system.

A maximum position deviation of 10 ns happening inside the pulse train is now simulated. The input signal to the electronics is the one represented in Figure 4.4. On this occasion, a 6 dB attenuator has been included in the model to maintain the signal within the ADC dynamic range. The output signal of the electronics is shown in Figure 4.11.

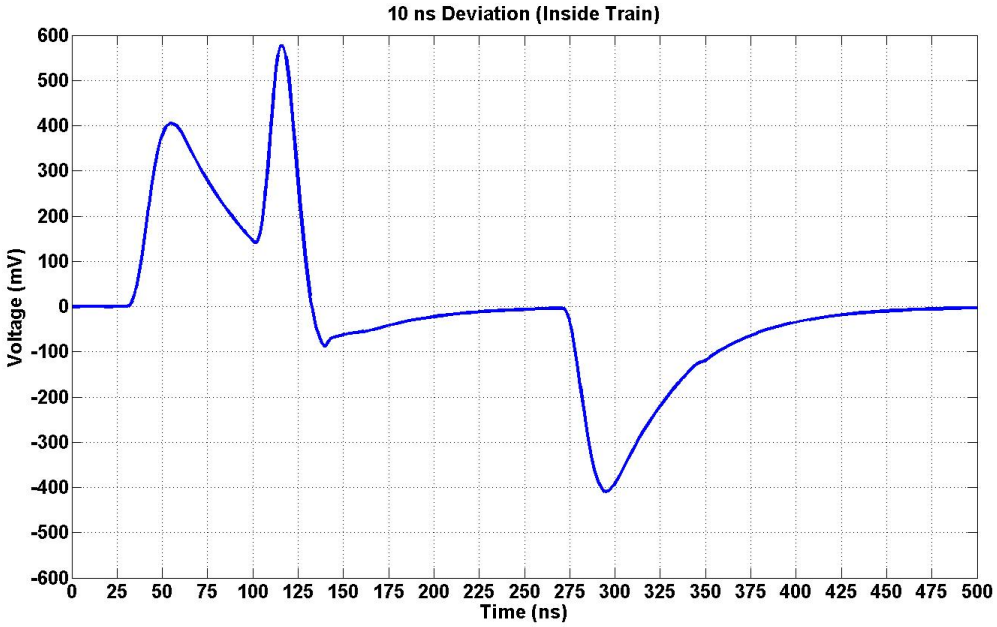


Figure 4.11: Time response to a maximum deviation of 10 ns happening inside the CLIC Drive Beam pulse train.

The maximum signal levels will always be the ones induced by a maximum deviation present during the passage of the full pulse train.

Figure 4.12 shows the simulated transfer function for the whole filter chain and its input impedance in the frequency domain.

The response has been simulated for an AC input of 1 A, so that 50 V in the plot corresponds to 50 Ω. It is possible to note the roll-off frequencies and the matched input impedance in the bandwidth of interest.

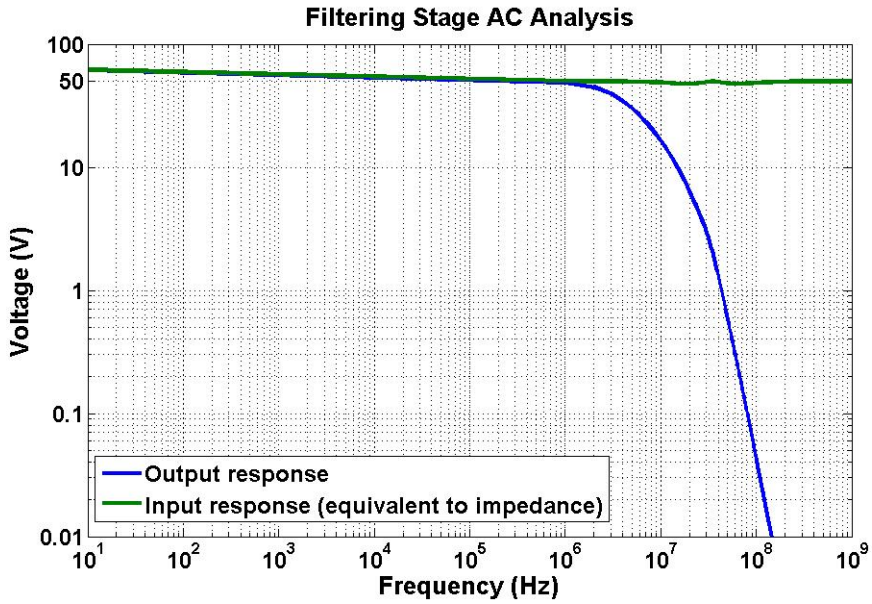


Figure 4.12: Transfer function and input impedance of the filtering stage.

#### 4.2.3.2 ADC Driving stage

The selected ADC driver is the LTC6406 model by Linear Technology®, with the following features: 1.6 nV/$\sqrt{\text{Hz}}$ noise, 18 mA current at 3V, Rail-to-Rail differential input, supply voltages from 2.7 to 3.5 V, power switch, compatible with ADC LTC2174-15 ($V_{OCM}$ = 0.9 V) and the distortion characteristics for the second and third harmonics detailed in [54].

In subsection 4.2.1, the ADC input noise for a dynamic range of 2 V - 11.8 ENOB was calculated to be 162 $\mu$Vrms.

The total output integrated noise of the analog readout chain can be reduced by limiting the output bandwidth of the driver amplifier to, for instance, 50 MHz, by implementing a filter with this cut-off frequency in the feedback loop of the driver. For any gain value implemented in this stage, the dynamic range will be limited by the ADC. On the other hand, it is possible to profit from the excess of dynamic range to implement a gain for the weakest signals, induced by the lowest charge beams. This favours their adaptation to the ADC dynamic range.

It would have also been possible to implement the first-order low-pass filter at 4 MHz as an active filter, placing a parallel RC branch in the feedback loop of the ADC driver amplifier, reducing the total output integrated noise to a further extent. However, the transfer function for this configuration had a zero around 150 MHz, not resulting in the ideal response in the bandwidth of interest.

Calculations in subsection 4.2.2 showed that an ENOB of 11.7 bits in the ADC allowed to obtain a 1.2 $\mu$m resolution if the full ADC scale is reached. As the specified resolution is 2 $\mu$m, an excess of dynamic range of $2/1.2 = 1.67$ can be assumed. In order to obtain a 2 $\mu$m, an input voltage 1.67 times lower would suffice, that is, 0.6 V instead of 1 V.

For $g = 1$, being $g$ the conversion gain from single to differential mode, the time response to a nominal centered beam had an amplitude of about 900 mVp, as shown in Figure 4.9.

For a nominal centered beam, the adquisition has been made with an excess of dynamic range of $0.9 \cdot 1.67 = 1.5$. This implies that, for $g = 1$, although the ADC dynamic range is not fully covered, the obtained resolution value is very favourable: $2/1.5 = 1.33\,\mu$m.

It is possible to calculate the maximum gain that can be implemented in the ADC driving stage without degrading the resolution value of 2 $\mu$m. An ENOB of 11.7 bits corresponds to an input noise of 173 $\mu$Vrms. Multiplying by the excess factor, 1.5, the system could withstand a total noise of $173 \cdot 1.5 \simeq 260\,\mu$Vrms. With these figures, the output noise after the driver amplifier is of about $\sqrt{260^2 - 173^2} = 194\,\mu$Vrms.

Simulations of the driver amplifier output noise as a function of the stage gain show that, for higher gains than 2, the following empirical expression applies:

$$V_{\text{noise}} \approx 21.1 \cdot g + 25.2 \tag{4.21}$$

The highest possible $g$ that fulfils Eq. 4.21 without surpassing the maximum value is $g = 8$. This is the maximum gain that can be used without degrading the resolution value above 2 $\mu$m.

As seen in previous sections, the minimum signal values are obtained for the lowest charge beams, with the lowest possible number $n$ of pulses per sector (out of 24). For $n = 1$, the amplitude of the output waveform is around 37 mV. With a $g = 8$ gain, the ADC input voltage ($V_{\text{in}}$) and the achievable resolution ($dX$) for other beam configurations have the following values:

- $\underline{n = 1} \rightarrow V_{in} = 8 \cdot 37\text{ mV} = 296\text{ mV} \longrightarrow dX = \frac{0.6\ V}{0.296\ V} \cdot 2\,\mu\text{m} = 4.05\,\mu\text{m}$
- $\underline{n = 2} \rightarrow V_{in} = 8 \cdot 74\text{ mV} = 592\text{ mV} \longrightarrow dX = \frac{0.6\ V}{0.592\ V} \cdot 2\,\mu\text{m} = 2.03\,\mu\text{m}$
- $\underline{n = 3} \rightarrow V_{in} = 8 \cdot 111\text{ mV} = 888\text{ mV} \longrightarrow dX = \frac{0.6\ V}{0.888\ V} \cdot 2\,\mu\text{m} = 1.35\,\mu\text{m}$

From $n = 4$ on, the ADC input voltages would exceed the scale (1 Vp), but appropriate programming of the attenuator will allow to keep the adjustments of the signal to the dynamic range. It must also be remarked that the specified resolution, 2 $\mu$m, can be achieved from $n = 3$ for centered beams.

- **Future performance considerations:**

It can be reasonably assumed that next-generation ADCs will have better features in terms of SNR, which will allow to reduce the ADC driving stage gain. It is estimated that this gain reduction will allow to save 2 bits for an ADC with a ±1 V range.

The possibility of using Low-Noise Amplifiers (LNAs) to provide the gain has also been considered. In the future, it would be an alternative in case the resolution becomes an issue. In this application, the use of LNAs has been avoided for two reasons: high power consumption, unnecessary with the current specifications, and a higher implementation complexity (need for switching to limit the consumption). The system architecture should be as simple as possible. Even if the resolution values estimated in this study may not be the final ones, as improvements in the components are expected in the future, they have allowed to assess the feasibility of an acquisition system of this kind.

• **Input impedance:**

The input impedance to the ADC driving stage $R_i$, depends on its gain, as the resistors in the feedback loop are related to the ones in the input branches (Figure 4.13). The following expression applies:

$$R_i = \frac{150}{1 - \frac{g}{2\cdot(1+g)}} \longrightarrow g = 8 \longrightarrow R_i = 270\ \Omega \tag{4.22}$$

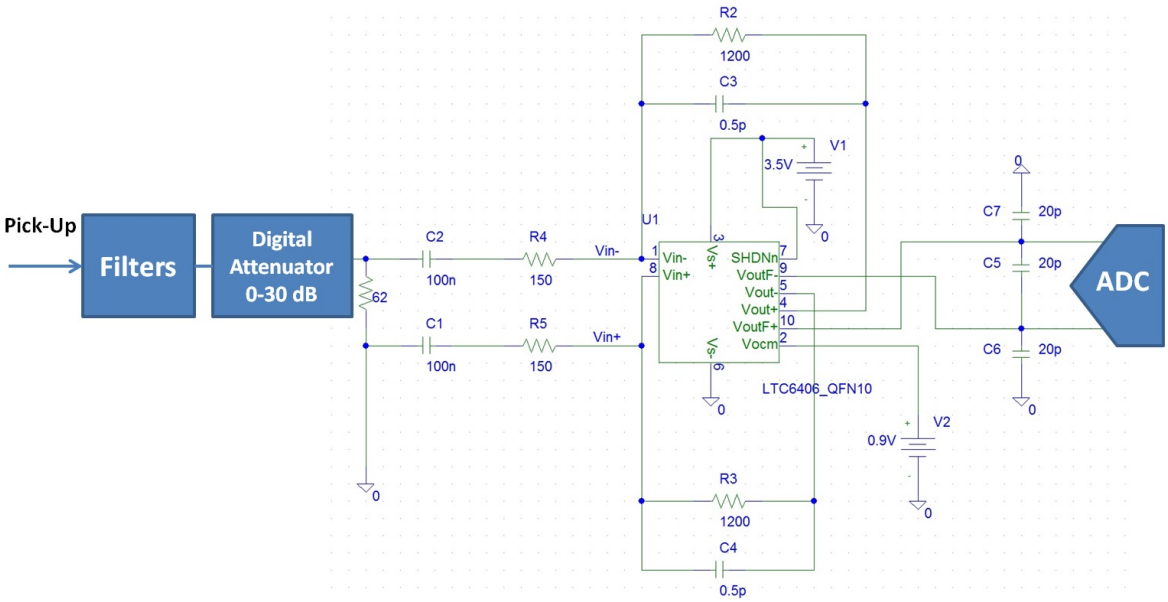


Figure 4.13: ADC driving stage with a 50 MHz low-pass filter in the feedback loop of the amplifier, preceded by a controllable attenuator and the filtering stage.

• **Programmable digital attenuator:**

For $g = 1$, a signal with 0.9 Vp amplitude was obtained in simulations corresponding to a centered nominal beam. For a maximally deviated nominal beam, the signal in the closest electrode should be 2.75 times bigger: around 2.5 Vp. For $g = 8$, attenuation of, at least, $1/(2.5\cdot 8) = 1/20$, that is, 26 dB, will be needed. The attenuator will be placed after the filtering stage and before the ADC driving stage to prevent level mismatch due to the gain. The input power in this case will be 2.5 Vp/50 Ω $\approx$ 21 dBm.

Digital programmable attenuators in versions of up to 30 dB, with 5 control bits (1 dB steps) and up to 25 dBm input power are currently available in the market.

The attenuator is the only digital component in the designed acquisition system. However, as it is not a memory component and is usually fabricated in GaAs technology, of proven robustness, no issues are expected in meeting the requirement on radiation hardness.

#### 4.2.3.3 Calibration

The calibration will be performed in real time and transparent to accelerator operations. The selected procedure is to implement a Digital-to-Analog Converter (DAC) to inject

white noise in the processing bandwidth. An electrode of each plane will be used as the calibration input for the adjacent plane.

#### 4.2.3.4 Test mezzanine

For the purpose of testing not only the complete BPM system, but also the performance of the ADCs, the data transmission in the HSMC connector, clock synchronization and the driver amplifier (LTC6406), a general-purpose acquisition mezzanine has been developed (Figure 4.14). The filters have not been included to be able to acquire also non-shaped test signals, but they will be connected externally during the tests.

A gain of 8 and a 26 dB attenuator were implemented to adapt the dynamic range of the readout chain. The considered sampling rate is 96 MSample/s and the output bandwidth is limited to 48 MHz.

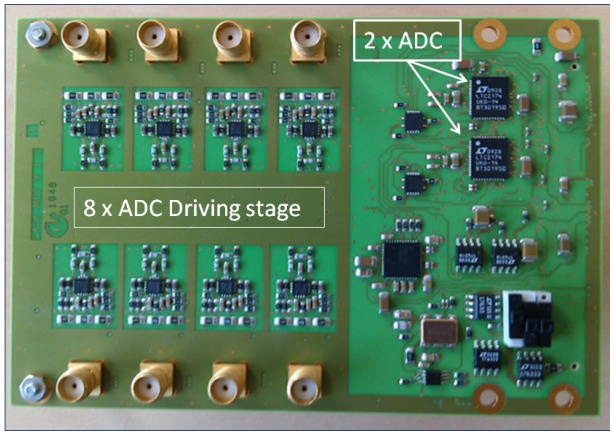


Figure 4.14: General-purpose acquisition mezzanine.

This mezzanine can be connected via HSMC to a PCIe card, similar to the considered ones for data reception on the surface, but it is also able to emulate the rest of the CLIC module acquisition system (motherboard, GBT optical transmission and further features).

## 4.3 Conclusions

This study shows that the designed electronic acquisition system fulfils the requirements of the project for the specified beam deviation ranges in terms of resolution (2 $\mu$m), accuracy (20 $\mu$m) and time resolution (10 ns). Due to the high number of units to be produced, the number of lumped elements has been minimized. As the signal processing scheme is based on charge integration, it can be adapted to other stripline PUs showing a different number of pulses in their multi-bunch response by simply changing the attenuator settings according to the new output signal levels.

# Chapter 5

# Laboratory Characterization Tests of the Prototype Stripline BPM System

Following the fabrication of the prototype stripline PU with short-circuited electrodes, the complete BPM system (PU and electronics) was characterized using two different test benches: in the first one a thin wire crossing the BPM emulates a beam bunch train in a low frequency range (up to approximately 150 MHz), allowing to test the acquisition electronics; in the second one, a 50 Ω-matched coaxial waveguide allows to measure the frequency response of the prototype PU up to approximately 15 GHz.

## 5.1 Low-Frequency characterization

### 5.1.1 Methodology

The purpose of this test is to characterize the prototype stripline BPM in laboratory using an emulation of the CLIC Drive Beam pulse (bunch train). The structure of this beam was described in Chapter 1 (Figure 1.6 and Table 1.1). Each pulse has a duration of 242 ns and consists of a train of bunches with 8.3 nC charge each, spaced 83.33 ps, corresponding to a 12 GHz bunching frequency. These bunches are Gaussian with a length of $\sigma_z = 1$ mm, which for a relativistic beam can be expressed in time as $\sigma_t = 3.33$ ps. Such a Gaussian pulse can be approximated by a rectangular pulse of duration $3\sigma_t = 10$ ps. As there are currently no commercial generators able to provide such short pulses, it is not possible to test the BPM in the laboratory on a bunch-by-bunch basis. Therefore, an alternative excitation method is needed so that the response of the BPM can be, under certain conditions, the same or proportional to its response to a real beam.

In the processing range of the acquisition electronics ($0-40$ MHz), a stripline pick-up behaves as a differentiator. Its response to a nominal multi-bunch train contains only the two first and the two last charge bunches, with opposed polarities. It is not possible to inject a 12 GHz signal in the thin wire, but it is indeed possible to inject a long current pulse of the same duration as the multi-bunch train (242 ns), containing the same charge.

The filters act as integrators for the captured image current by the stripline PU. As long as their duration does not exceed the time constant of the highest-frequency filter (in this case, 35 MHz), different input current signals enclosing the same area (charge)

will induce the same output signal in the filtering/shaping stage. For instance, the output signal for a 10 ns long input charge pulse of 1 nC will be the same as for a 100 ns long input pulse of 0.1 nC. Even for long time integrations (longer than 20 ns) the response is very similar (about 90%) and allows to characterize the BPM.

The goal is to inject a high current pulse with a very short rise/fall time $t_r$ and a constant amplitude $I_{b0}$: the PU will derive this signal, resulting in an output with constant pulses whose amplitude is proportional to the slope of the input signal rise and whose duration is equal to the rise/fall time $t_r$ (Figure 5.1).

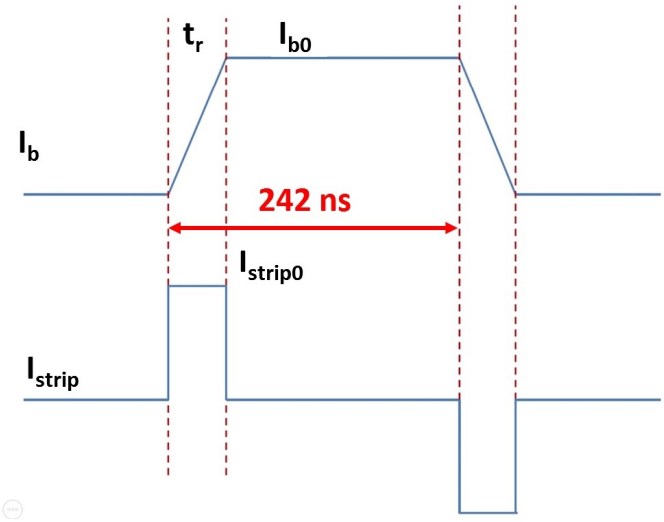


Figure 5.1: Emulation of the CLIC Drive Beam bunch train with a 242 ns long pulse (top) to excite the stripline BPM; output signal with rectangular pulses during the input signal rise and fall time intervals (bottom).

The next step is to consider the relationship between the currents of both signals. Being $I_b$ the injected current in the wire, $I_{\text{strip}}$ the output current of the stripline PU and $t_r$ the rise time, both currents are related as:

$$I_{\text{strip}} = \frac{\tau_0}{8} \cdot \frac{\delta I_b}{\delta t} \tag{5.1}$$

where $\tau_0$ is the time constant of the equivalent high-pass filter formed by the PU at low frequencies, and the factor $1/8$ accounts for the fraction of the total current captured by each stripline electrode when the beam, or the wire in our model, is centered. It is possible to calculate the value of $\tau_0$ considering the tangent of the stripline transfer function at the origin (Figure 5.2).

The transfer function of the stripline prototype PU, normalized to unity, can be expressed as $G(f) = \sin(\frac{\pi \cdot f}{6 \cdot 10^9})$. For low frequencies, the sine function can be approximated by its argument, resulting in $G(f) \approx \frac{\pi \cdot f}{6 \cdot 10^9}$. The cut-off frequency of the equivalent high-pass filter of the PU is given by the point where the linearly approximated plot reaches the maximum value of the original sine function:

$$1 = \frac{\pi \cdot f_{c_{HP}}}{6 \cdot 10^9} \longrightarrow f_{c_{HP}} = 1.91 \text{ GHz} \tag{5.2}$$

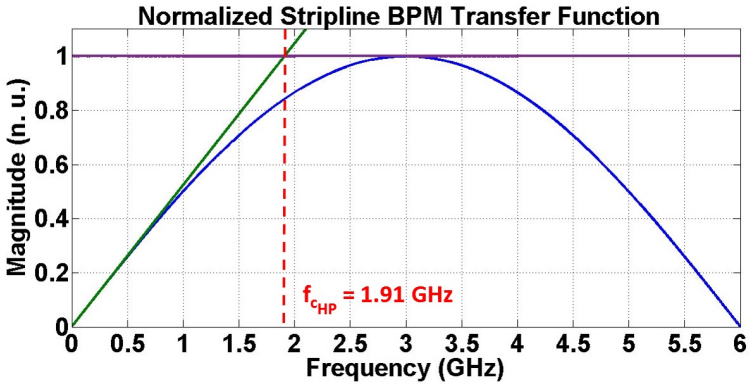


Figure 5.2: Normalized transfer function (blue trace) and equivalent high-pass filter response with $f_{c_{HP}} = 1.91$ GHz (green and purple traces) of the prototype stripline PU.

corresponding to a time constant of $\tau_0 = 1/(2\pi \cdot 1.91 \cdot 10^9) = 83,33$ ps, the same value as the CLIC DB bunching period.

If the rise/fall is linear, $I_{b0}$ being the final pulse amplitude on the wire, we obtain, for the interval $0 < t < t_r$:

$$I_b = t \cdot \frac{I_{b0}}{t_r} \longrightarrow \frac{\delta I_b}{\delta t} = \frac{I_{b0}}{t_r} \tag{5.3}$$

Finally, the amplitude of the output pulses of the stripline PU is calculated as:

$$I_{strip0} = \frac{\tau_0}{8} \cdot \frac{I_{b0}}{t_r} \tag{5.4}$$

The response of the prototype stripline PU to a centered multi-bunch beam was first considered in Chapter 3: it consists of a pair of bunches at the beginning of the train and another pair of pulses of opposed polarity at the end, 242 ns later (Figure 3.2). In Chapter 4, the charge of each one of these bunches was calculated as 0.52 nC (Eq. (4.2)). Therefore, the total charge captured by each stripline PU electrode in the presence of a nominal centered multi-bunch beam is 1.04 nC.

### 5.1.2 Test setup

The test setup used for the low-frequency characterization of the prototype stripline PU with short-circuited electrodes is located at the laboratories of the CERN Beam Instrumentation Group (BE-BI), and was designed for the characterization of the LINAC4 stripline BPMs [55] [56]. It consists of a structure where the Device Under Test (DUT) is fixed in the center and crossed by a thin wire of 0.2 mm diameter that can be moved in both the horizontal and the vertical directions by two servomotors with a 5 $\mu$m precision [57]. The signal input is performed via an SMA connector placed at the upstream end of the wire. Another SMA connector at the downstream end of the wire allows to choose the type of termination: open, short-circuit or a 50 $\Omega$ impedance. For this test, we chose a short-circuit. Two additional vacuum chambers are added upstream and downstream of the BPM to avoid abrupt discontinuities in the vicinity of the BPM that could alter the field distribution reaching the electrodes. The structure is represented in Figure 5.3.

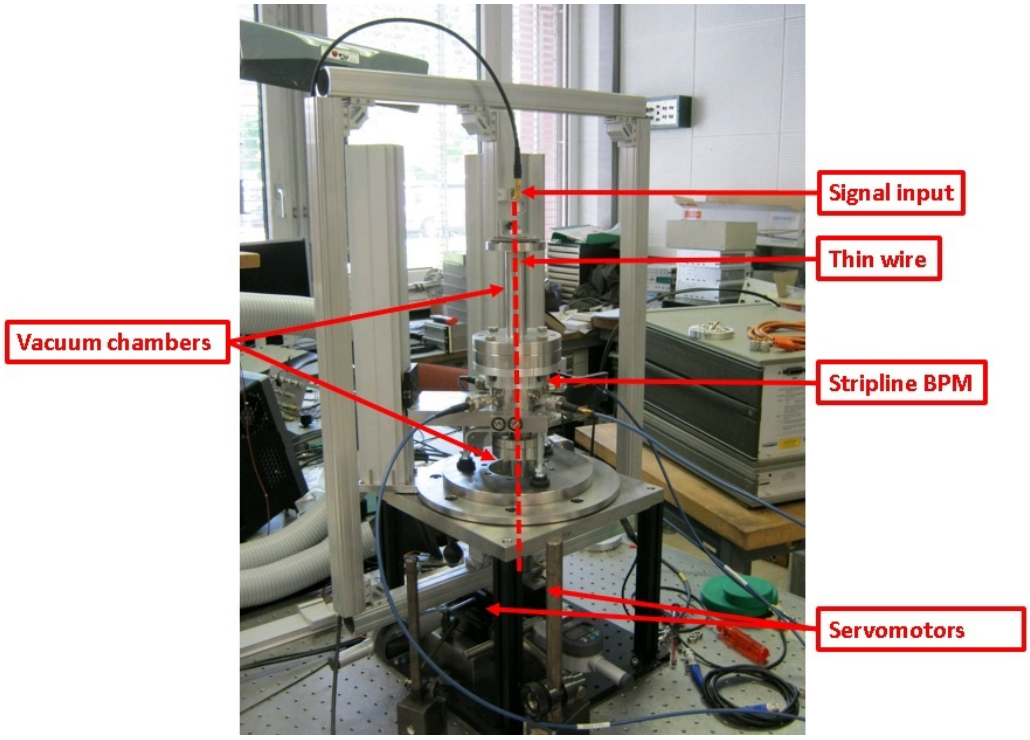


Figure 5.3: Thin wire test bench for low-frequency characterization of the prototype stripline BPM.

A current pulse generator with $t_r \approx 15$ ns, 10 A over 50 Ω [58], was used to excite the BPM through the thin wire. An important aspect to consider is the matching of the input impedance of the system formed by the cable and the BPM mounted in the test bench. This impedance was measured by means of a Time Domain Reflectometry (TDR) to be about 270 Ω. Therefore, it was necessary to place a 62 Ω parallel resistor at the input of the test bench, so that the total input impedance would be 50 Ω. Due to this matching, it was not possible to inject all the current given by the generator in the wire traversing the BPM, but about $\frac{62}{62+270} \approx 19\%$ (1.9 A).

The diagram of the test setup with its different components is shown in Figure 5.4.

The equipment used for this test, apart from the wire test bench, is listed below:

- A customized laboratory-made current pulse generator with $t_r \approx 15$ ns, 10 A over 50 Ω [58].
- As power supply sources for the current pulse generator, the TTI®TSX3510P [59] and the ELC®AL-936N [60] units were used.
- The Tektronix®AFG3252 arbitrary function generator [61] was used to generate the trigger.
- As clock generator, the CG635 model by SRS® [62] was used.
- An external board where the passive filters described in Chapter 4, section 4.2 were implemented.

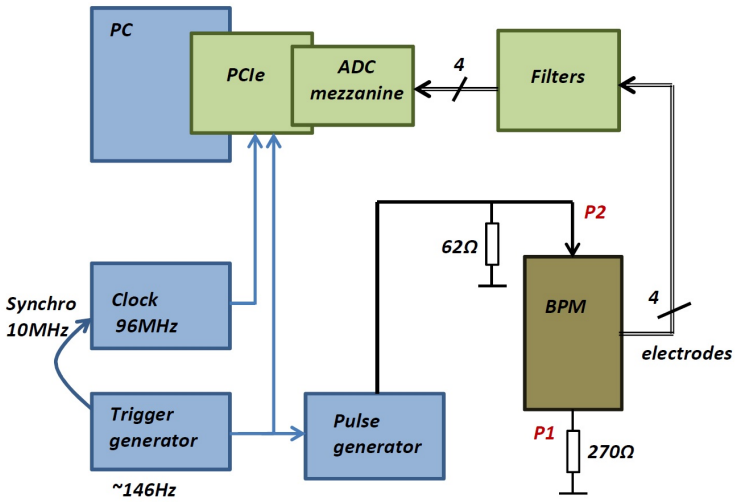


Figure 5.4: Block diagram of the test bench for low-frequency characterization of the prototype stripline BPM.

- The test mezzanine described in Chapter 4, section 4.2, able to acquire the signals from up to two BPMs.
- The PCIe card described in Chapter 4, section 4.2, which emulates the rest of the CLIC module acquisition system.
- A computer performing the data acquisition.

The complete laboratory setup is shown in Figure 5.5.

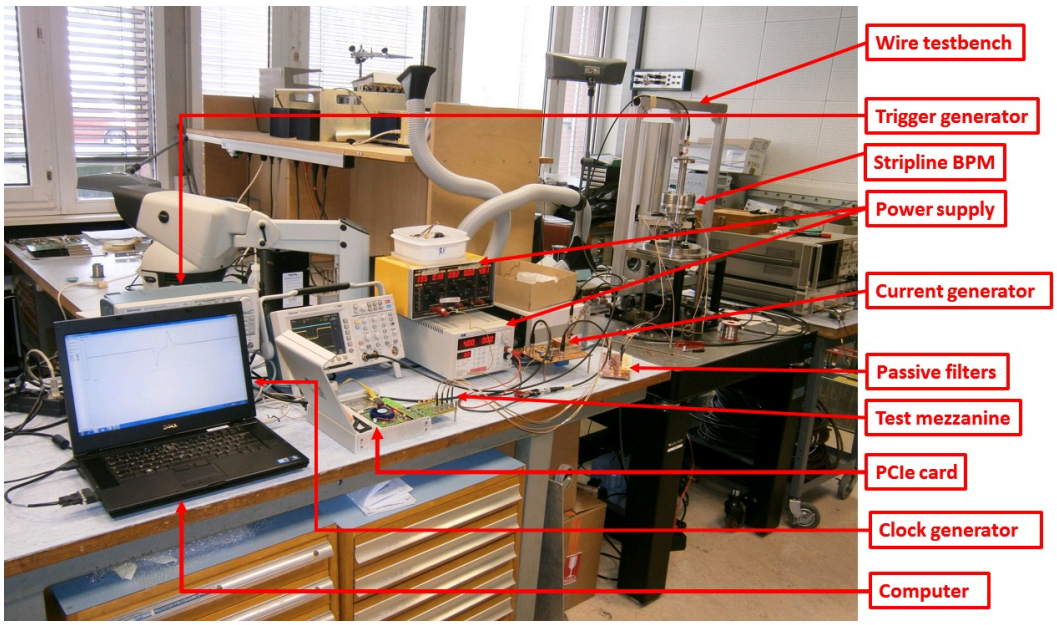


Figure 5.5: Complete setup for low-frequency characterization of the prototype stripline BPM.

The reference sampling clock rate was chosen to be $f_{\text{sample}} = 96$ MHz, the same as in CTF3 at the scheduled time of installation. The acquisition mezzanine was connected via HSMC to the PCIe test card, which was connected to the computer. Similarly as in the accelerator, a synchronous clock signal and an acquisition trigger must be provided to the PCIe card. The ADC samples the BPM signals on a continuous basis and sends the data to an FPGA FIFO. Upon reception of the trigger, the FIFO freezes with a delay corresponding to the length of the desired data acquisition window and the latency of the complete system. At this point, the data can be transferred to the PC through the PCIe bus. Both the clock and the trigger must be synchronous. As the current is generated by discharging capacitances, the trigger rate must be below a maximum frequency (typically 500 Hz). For this test we used 146 Hz. The main timing challenge is to produce synchronous trigger and clock signals with very different frequencies.

Acquisition and analysis software [63] was developed in C++ to process the BPM data, allowing offset calibration, adjustment of the length of the acquisition window and data averaging on a configurable number of windows. Additionally, it allows real-time extraction of the position signal and reconstruction of the beam pulse by deconvoluting the BPM signals with the theoretical transfer function.

The wire was aligned with the electrical center of the BPM by means of an optical fork [64], providing a $\pm 5$ $\mu$m precision. The acquisition chain and the electrical and mechanical centers of the BPM were calibrated afterwards.

### 5.1.3 Simulation of the test scenario

As described in Chapter 4, section 4.1, the horizontal and the vertical positions can be estimated theoretically as:

$$x = \frac{R}{2} \cdot \left(\frac{\Delta}{\Sigma}\right)_H = \frac{R}{2} \cdot \frac{V_{\text{right}} - V_{\text{left}}}{V_{\text{right}} + V_{\text{left}}}$$
$$y = \frac{R}{2} \cdot \left(\frac{\Delta}{\Sigma}\right)_V = \frac{R}{2} \cdot \frac{V_{\text{up}} - V_{\text{down}}}{V_{\text{up}} + V_{\text{down}}} \tag{5.5}$$

where $\Delta$ and $\Sigma$ are the difference and the sum, respectively, of the voltage signals from the electrodes (right, left, up and down) and $R$ is the vacuum pipe radius. This estimation is a first approximation that does not take into account several aspects of the BPM, such as the specific geometry of the electrodes.

A 2D simulation of the PU geometry with the CST Studio Electrostatic Solver provides a more accurate estimation of the difference-over-sum ratio as the beam (or the wire) moves off the center in one or both coordinate planes.

Firstly, the cross-section of the PU geometry is modeled and one of the electrodes is set to a normalized potential of 1 V, leaving the other three at 0 V, as shown in Figure 5.6. The result of this simulation is the distribution of the potential in both the vertical and the horizontal directions along the cross-section. This is represented in Figure 5.7.

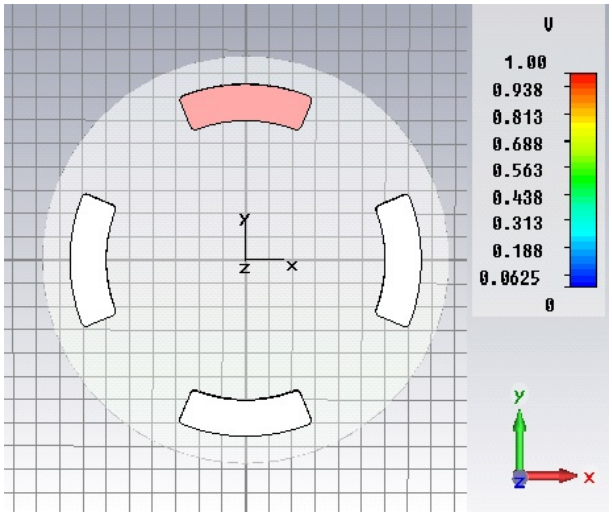


Figure 5.6: Simulation model with the potential in the upper electrode set to 1 V.

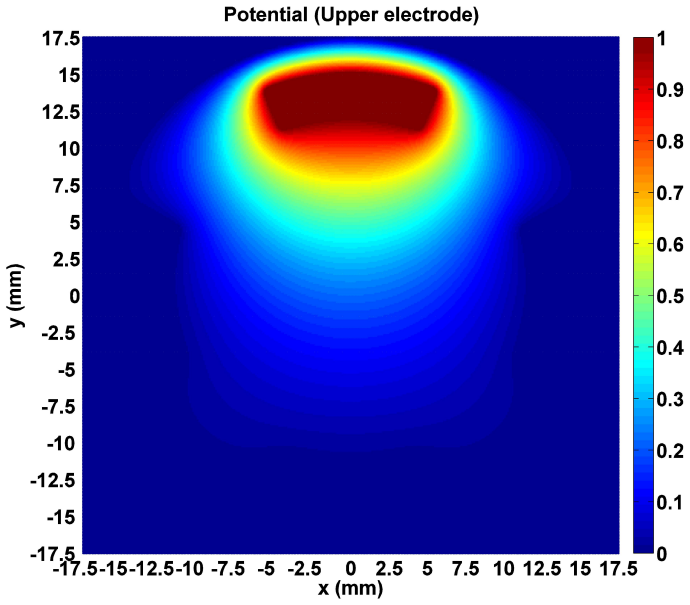


Figure 5.7: Distribution of the potential in both directions of the cross-section of the stripline PU due to the upper electrode being set to 1 V.

As the geometry of the prototype stripline PU is symmetric with respect to the $x$ and $y$ axes, the result data matrix from the simulation corresponding to the upper electrode can be flipped 90°, 180° and 270° with mathematical software (in our case MATLAB®), obtaining the distribution of the potential for the left, down and right electrodes, respectively, without repeating the simulation. Figure 5.8 illustrates the distribution of the potential for the left electrode.

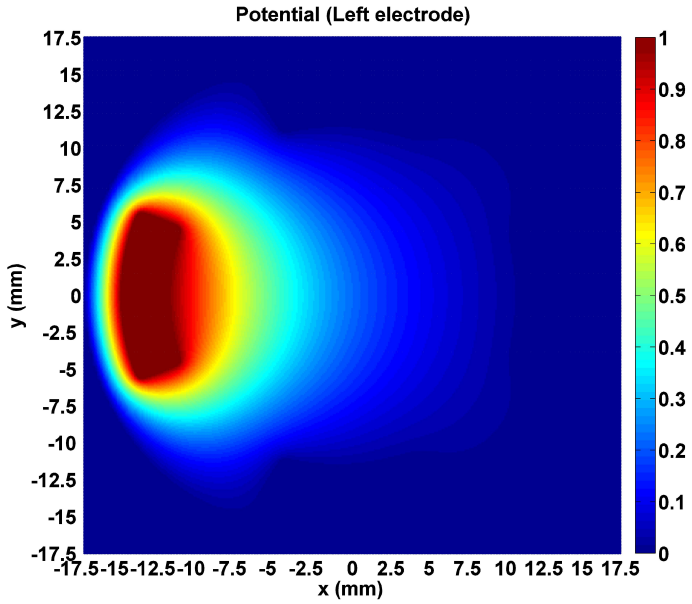


Figure 5.8: Distribution of the potential in both directions of the cross-section of the stripline PU due to the left electrode being set to 1 V.

Using Eq. (5.5) with the four potential data matrices, it is possible to obtain the difference-over-sum ratio in the whole cross-section ($XY$ plane, $\vec{z}$ being the propagation direction of the beam). The result is plotted in Figures 5.9 and 5.10. The gaps observed in the location of the electrodes of the opposite coordinate axis are due to the potential distribution not being defined inside perfect conductors.

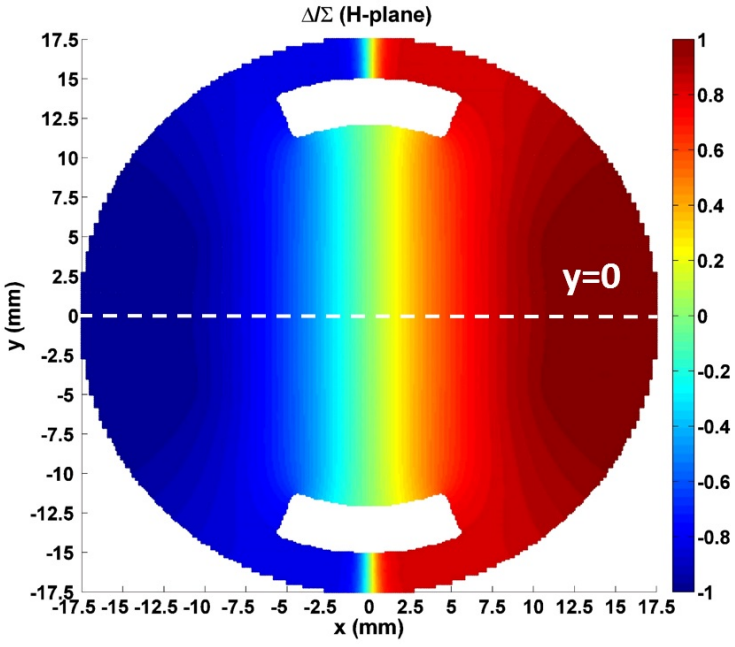


Figure 5.9: Difference-over-sum ratio in the BPM cross-section for the horizontal plane.

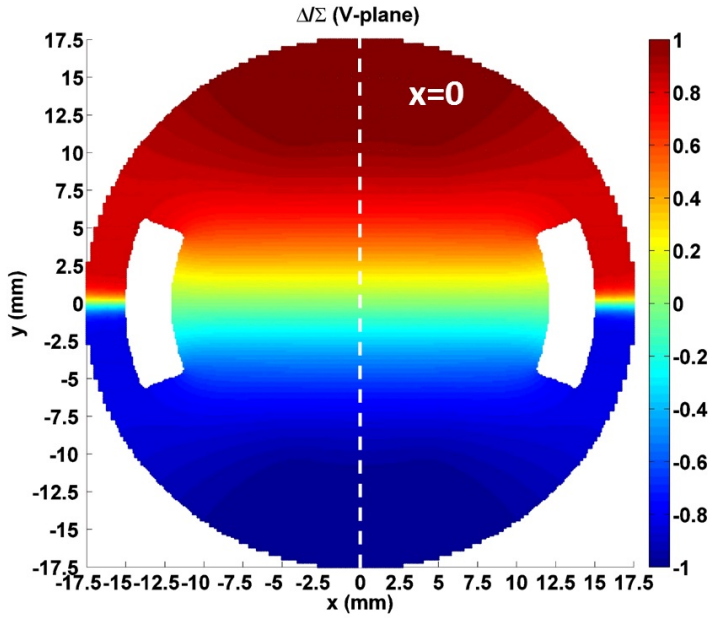


Figure 5.10: Difference-over-sum ratio in the BPM cross-section for the vertical plane.

At this point, it is possible to extract the curves for $x = 0$ and $y = 0$ (dashed line in Figures 5.9 and 5.10), obtaining the simulated difference-over-sum signal values for the intended movement directions of the wire. The results are shown in Figure 5.11. The curve is the same for the horizontal and the vertical axis. The value of the slope at the origin is 137 $m^{-1}$. These results will also be shown in Figures 5.15 and 5.16 and in Table 5.2 for comparison.

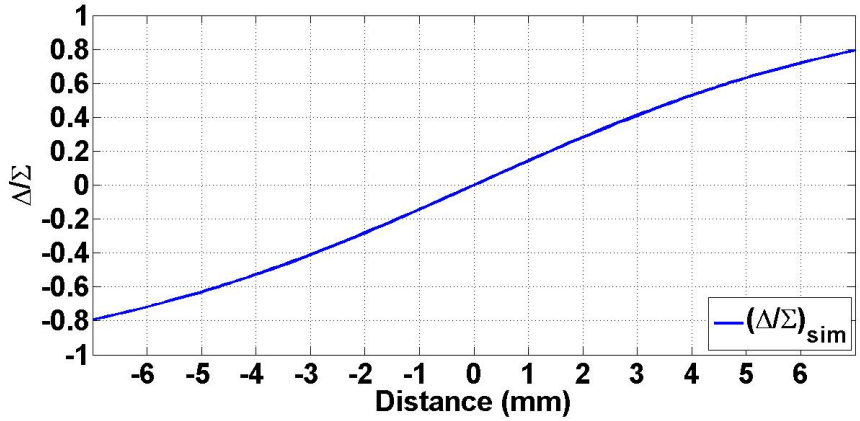


Figure 5.11: Simulated difference-over-sum signal curve for movements along the $x$ ($y = 0$) and $y$ ($x = 0$) axes.

### 5.1.4 Results

The injection of the pulse described in section 5.1.1 in a centered wire produced the signals shown in Figure 5.12.

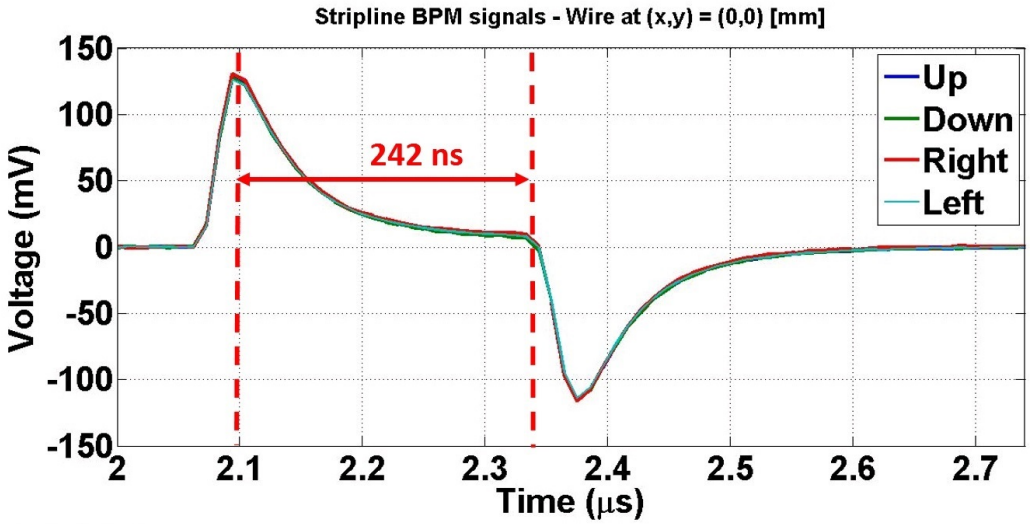


Figure 5.12: Output waveforms of the electronics produced by the low-frequency emulation of a centered 242 ns multi-bunch beam.

The proposed test method has led to output signals with the same shape as the simulated ones in Chapter 4, section 4.2, for a wide variety of beam configurations (Figure 4.10). There is, however, an unforeseen effect: the signal does not completely return to zero after the first pulse. Two possible reasons for this effect are the accumulation of charge and impedance mismatch in the test setup.

In order to test the sensitivity and linearity parameters of the prototype, the wire was displaced in both axes, $x$ and $y$, in steps of 1 mm within a range of ±6 mm. As expected, the shape of the output signals is maintained for all tested positions of the wire, the amplitude for each channel depending only on the distance from its corresponding electrode, demonstrating the correct performance of the designed acquisition scheme. Figure 5.13 shows the output signals for all four positions on the coordinate axes at a distance of 4 mm from the center. The amplitude variation is of about 1.2 dB/mm.

The measured position is extracted using Δ/Σ processing. Eqs. (4.4) and (4.7) in Chapter 4 determine, without any assumptions, the Δ/Σ ratio function for a movement of the beam along both axes $x$ and $y$, known from now on as the theoretical Δ/Σ curve, displayed also in Figures 5.15 and 5.16 for comparison. Eq. (4.10) in Chapter 4 assumes small beam displacements from the center compared to the pipe radius ($x, y << R$), estimating the position as a function of the difference-over-sum ratio as:

$$x = \frac{R}{2} \cdot \left(\frac{\Delta}{\Sigma}\right)_H = \frac{R}{2} \cdot \frac{S_{\text{right}} - S_{\text{left}}}{S_{\text{right}} + S_{\text{left}}}$$
$$y = \frac{R}{2} \cdot \left(\frac{\Delta}{\Sigma}\right)_V = \frac{R}{2} \cdot \frac{S_{\text{up}} - S_{\text{down}}}{S_{\text{up}} + S_{\text{down}}} \tag{5.6}$$

where R is the beam pipe radius, $\left(\frac{\Delta}{\Sigma}\right)_{H,V}$ is the difference-over-sum ratio in the horizontal

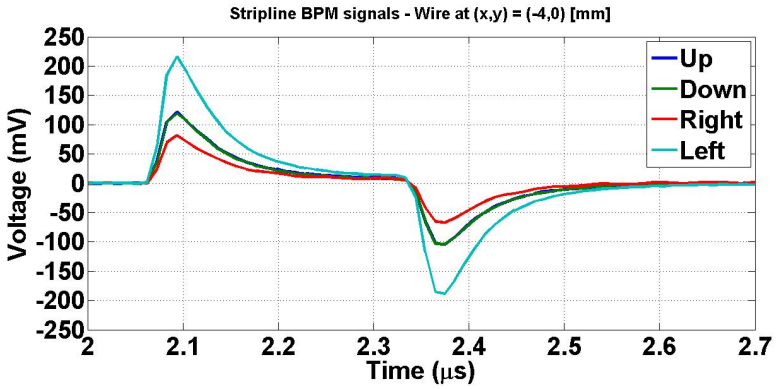


(a) (x,y) = (-4,0)

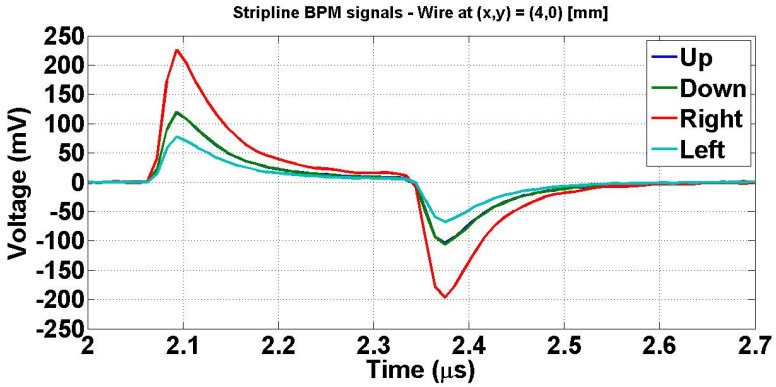


(b) (x,y) = (4,0)

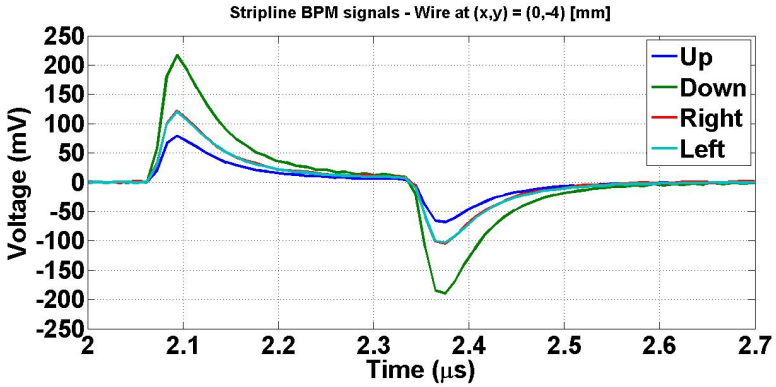


(c) (x,y) = (0,-4)

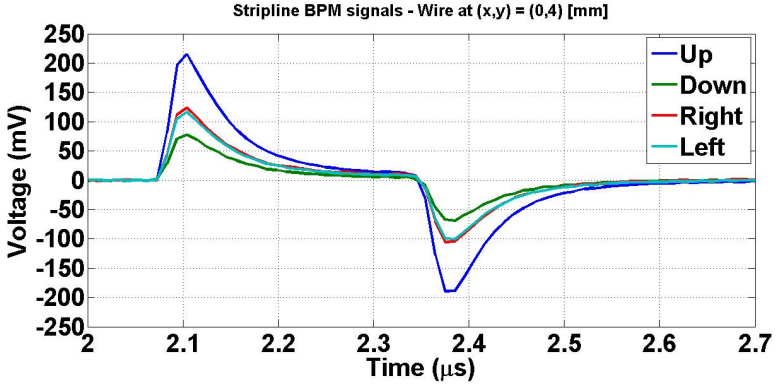


(d) (x,y) = (0,4)

Figure 5.13: Output waveforms of the electronics produced by the low-frequency emulation of a 242 ns multi-bunch beam at a distance of 4 mm off the center.

and vertical plane, respectively, and $S_i$, $i = (R, L, U, D)$ is the metrics from the $i^{th}$ electrode used for the position calculation. Different signal properties can be used, the most common choices being the peak voltage value or the area under the voltage curve within a specific time interval. The second option makes better use of the information contained in the BPM output signals. In our case, the area under the positive semi-pulse of the waveforms is computed, considering 5% of the peak voltage value $Vp$ as threshold (Figure 5.14), and input in Eq. (5.6). As the BPM output signals have been already digitized with $f_{sample}$ as sampling rate, the area $S_i$ under each signal $v_i[n]$ can be calculated as:

$$S_i = \sum_{n=N_{\text{start}}}^{N_{\text{end}}} v_i[n] \cdot T_{\text{sample}} \tag{5.7}$$

where $N_{\text{start}}$, $N_{\text{end}}$ are the extremes of the integration interval and $T_{\text{sample}} = 1/f_{\text{sample}}$ is the sampling period.

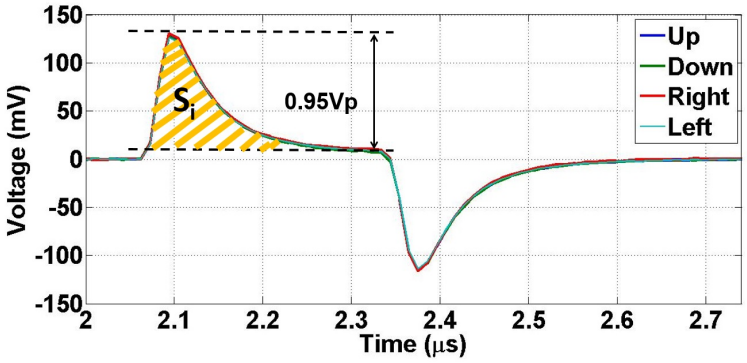


Figure 5.14: The area under the output waveform is used as metrics for the position calculation using Δ/Σ processing.

The linearity and sensitivity parameters are given by:

$$x, y = (S_{H,V}^{-1}) \cdot \left(\frac{\Delta}{\Sigma}\right)_{H,V} + EOS_{H,V} \tag{5.8}$$

where $S_{H,V}$ is the sensitivity and $EOS_{H,V}$ is the electrical offset. Another important parameter is $\sigma_{H,V}$, the contribution, for each plane, of the nonlinearity to the overall precision, giving the uncertainty in the position measurements. The sensitivity and the electrical offset are obtained from the linear fit between the measured positions of the wire ($x$ or $y$) by a micrometer [65], known in the following as reference positions, and the values of $\left(\frac{\Delta}{\Sigma}\right)_{H,V}$ measured by the BPM. The contribution of the nonlinearity to the overall precision is calculated as the r.m.s. value of the linearity error, that is, the difference between the reference positions and the measured positions by the BPM. The measured sensitivity curves are represented in Figures 5.15 and 5.16 for the vertical and the horizontal plane, respectively. The values of the reference positions and the measured Δ/Σ for the vertical and the horizontal plane are shown in Table 5.1. The parameters of the linear fit for both planes as expressed in Eq. (5.8) are shown in Table 5.2. The uncertainties in the sensitivity and in the electrical offset have been calculated as the standard errors of both linear regression parameters.

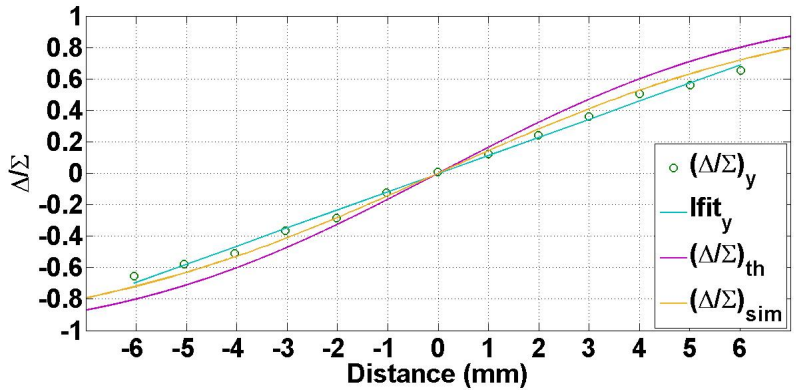


Figure 5.15: Theoretical (purple trace), simulated (orange trace) and measured (green trace) sensitivity curves in the vertical plane for the prototype stripline BPM.

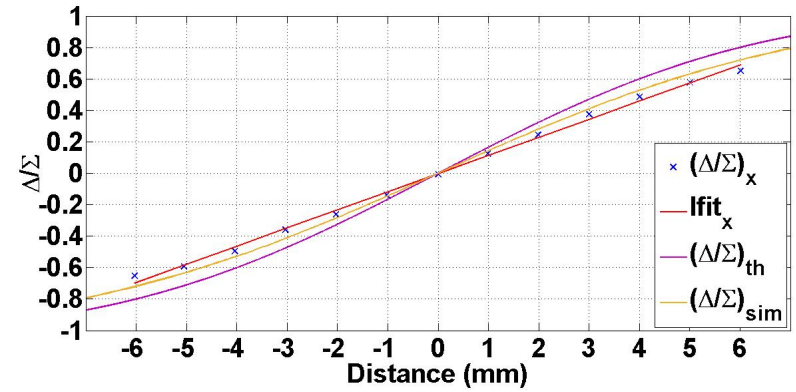


Figure 5.16: Theoretical (purple trace), simulated (orange trace) and measured (red trace) sensitivity curves in the horizontal plane for the prototype stripline BPM.

### 5.1.5 Conclusions

The experimentally obtained data sets (green circles and blue crosses in Figures 5.15 and 5.16, respectively) have the same shape as the theoretically derived function in Chapter 4, section 4.1. This theoretical approximation, proposed in Eq. (5.6), estimates the position as $x, y = \frac{R}{2} \cdot \left(\frac{\Delta}{\Sigma}\right)_{H,V}$ and, therefore, from Eq. (5.8), the sensitivity as $S_{H,V} = \frac{2}{R} = 166.67\ \mathrm{m}^{-1}$ However, the slope of the experimental curves and, therefore, the measured sensitivities, are smaller than in the theoretical plot (purple trace). The numerical simulation described in subsection 5.1.3 (orange trace) estimates a sensitivity of 137 $\mathrm{m}^{-1}$, which is closer to the obtained results. Charge accumulation and impedance mismatches in the measurement setup are the most likely causes of this difference in sensitivity.

## 5.2 High-Frequency characterization

Having characterized the prototype stripline BPM with short-circuited electrodes in the low frequency regime using a thin wire, the next step is evaluating the high-frequency be-

| Vertical | | Horizontal | |
|---|---|---|---|
| **Wire position [m]** | $(\Delta/\Sigma)_V$ | **Wire position [m]** | $(\Delta/\Sigma)_H$ |
| $-6.0460 \cdot 10^{-3}$ | -0.6543 | $-6.0310 \cdot 10^{-3}$ | -0.6523 |
| $-5.0420 \cdot 10^{-3}$ | -0.5782 | $-5.0500 \cdot 10^{-3}$ | -0.5928 |
| $-4.0380 \cdot 10^{-3}$ | -0.5075 | $-4.0400 \cdot 10^{-3}$ | -0.4947 |
| $-3.0310 \cdot 10^{-3}$ | -0.3662 | $-3.0320 \cdot 10^{-3}$ | -0.3608 |
| $-2.0240 \cdot 10^{-3}$ | -0.2840 | $-2.0290 \cdot 10^{-3}$ | -0.2637 |
| $-1.0200 \cdot 10^{-3}$ | -0.1220 | $-1.0250 \cdot 10^{-3}$ | -0.1390 |
| $-0.0130 \cdot 10^{-3}$ | 0.0069 | $0.0020 \cdot 10^{-3}$ | -0.0064 |
| $0.9930 \cdot 10^{-3}$ | 0.1213 | $0.9900 \cdot 10^{-3}$ | 0.1265 |
| $1.9980 \cdot 10^{-3}$ | 0.2427 | $1.9900 \cdot 10^{-3}$ | 0.2428 |
| $3.0030 \cdot 10^{-3}$ | 0.3630 | $2.9990 \cdot 10^{-3}$ | 0.3737 |
| $4.0080 \cdot 10^{-3}$ | 0.5068 | $4.0050 \cdot 10^{-3}$ | 0.4873 |
| $5.0120 \cdot 10^{-3}$ | 0.5603 | $5.0080 \cdot 10^{-3}$ | 0.5755 |
| $6.0160 \cdot 10^{-3}$ | 0.6528 | $6.0130 \cdot 10^{-3}$ | 0.6493 |

Table 5.1: Reference and measured positions in the vertical (left) and the horizontal (right) planes.

| Parameter | Measurement | Theory | Simulation |
|---|---|---|---|
| **Vertical** | | | |
| $S_V$ [$m^{-1}$] | $115.19 \pm 2.32$ | 166.67 | 137.01 |
| $EOS_V$ [m] | $(0.03 \pm 0.08) \cdot 10^{-3}$ | 0.00 | 0.00 |
| $\sigma_V$ [m] | $251.07 \cdot 10^{-6}$ | | |
| **Horizontal** | | | |
| $S_H$ [$m^{-1}$] | $115.17 \pm 1.98$ | 166.67 | 137.01 |
| $EOS_H$ [m] | $(0.02 \pm 0.07) \cdot 10^{-3}$ | 0.00 | 0.00 |
| $\sigma_H$ [m] | $214.07 \cdot 10^{-6}$ | | |

Table 5.2: Linearity and sensitivity parameters for the vertical (top) and horizontal (bottom) planes.

havior of the stripline PU (without electronics), in particular, its filtering properties around 12 GHz. This section describes the measurement methododology that was followed for this test, the high-frequency characterization bench used and the obtained results.

### 5.2.1 Methodology

In order to evaluate the filtering properties of the prototype stripline BPM at the PETS RF interference frequency (12 GHz), its transfer response needs to be measured up to the frequency region of interest. The first step is to find a suitable method that allows to inject signal components in such a broad frequency range. This goal can be achieved using a coaxial waveguide testbench, such as the one designed at IFIC for the measurement of the frequency response of the TBL inductive BPMs [66]. The only necessary modification is to adapt the interconnecting flanges to those of the stripline BPM.

The transfer response of the DUT in our emulated system is equivalent to the forward

transmission coefficient $S_{21}$ from the upstream port of the test bench (Port 1) to one of the stripline BPM ports (Port 2). The S-Parameters are calculated as the ratio between outgoing and incident voltages from either the same or different ports of a given system. If calculated for the same port, they represent the reflection coefficient; otherwise, forward transmission coefficients between the two ports. Figure 5.17 illustrates a four-port system where the incident and outgoing voltages $V_i^+$ and $V_i^-$, respectively, $i \in \{1, 2, 3, 4\}$ are represented for each port.

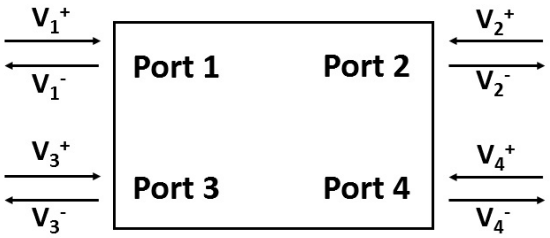


Figure 5.17: Incident and outgoing voltages in a four-port system.

Mathematically, for port $a$ and port $b$, the S-parameter from port $a$ to port $b$ is defined as:

$$S_{ba} = \frac{V_b^-}{V_a^+} \tag{5.9}$$

The S-Parameters can be measured using a Vector Network Analyzer (VNA). A variable frequency test signal, normally a sine wave, is generated internally, split and input into a test channel, connected via a precision cable to the selected port of the DUT, and into a reference channel (reference receiver). In the test channel, a directional coupler acts as signal separator and couples off the power reflected from the DUT after the injection of the test signal in the selected port, feeding it to a test receiver. The reference and the test receivers are coherent, as they are fed by the same reference oscillator, enabling them to measure the test signal's amplitude and phase at the test frequency. A sweep can then be performed over a selected frequency range (from low frequencies to 12 GHz in this case), obtaining the transfer response of our prototype stripline BPM. A generalized block diagram of a VNA is shown in Figure 5.18 [67].

### 5.2.2 Test setup

Figure 5.19 shows the high frequency test bench, consisting of a coaxial waveguide whose external conductor has the same aperture as the vacuum chamber of the CLIC DB. An internal conductor has been designed with an appropriate radius so that the characteristic impedance $Z_c$ is 50 Ω all along the waveguide. For a coaxial waveguide, the characteristic impedance is given by:

$$Z_c = \frac{c\mu_0}{2\pi\sqrt{\epsilon_r}} \ln\left(\frac{r_\mathrm{o}}{r_\mathrm{i}}\right) \tag{5.10}$$

where $c$ the speed of light in vacuum, $\mu_0$ the magnetic permeability in vacuum, $\epsilon_r$ the relative electrical permittivity of the medium connecting both conductors, and $r_\mathrm{i}$ and $r_\mathrm{o}$ are, respectively, the radii of the inner and the outer conductors. Using $r_\mathrm{o} = 12$ mm in Eq. (5.10) provides the necessary radius of the inner conductor for a constant 50 Ω characteristic impedance: $r_\mathrm{i} = 10.422$ mm. Conical transitions have been designed to

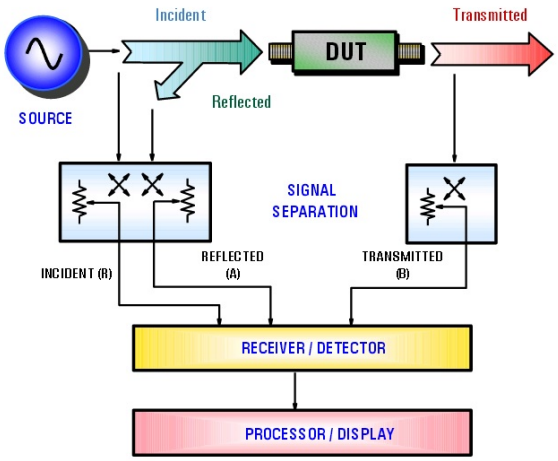


Figure 5.18: Generalized block diagram of a Vector Network Analyzer.

maintain the impedance matching from the straight section of the waveguide up to the SMA connectors placed at the extremes.

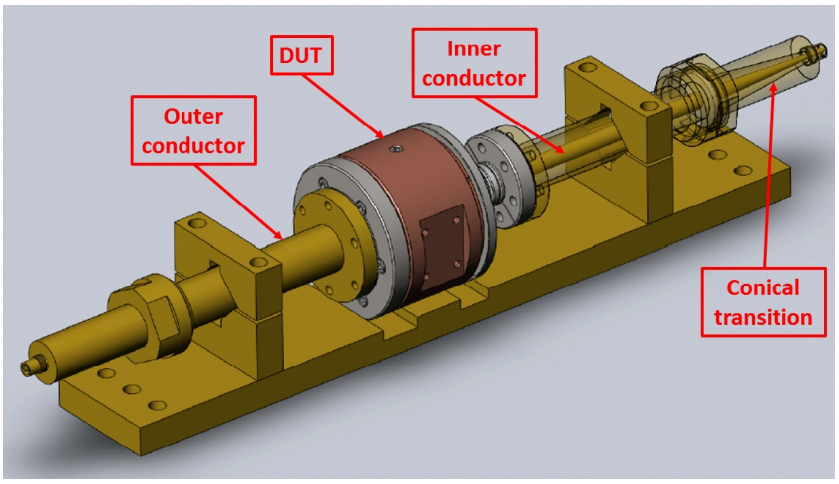


Figure 5.19: 3D view of the high frequency characterization test bench for BPMs (up to, approximately, 16 GHz).

With the previously described geometry, the cut-off frequencies of all high-order modes of the coaxial waveguide itself stay above 18 GHz, providing a wide frequency range for BPM characterization, including the range of interest for the study of the prototype stripline BPM, around 12 GHz.

The versatility of this test bench allows its use for different BPM prototypes. The external conductor is implemented in two separate movable sections, allowing to insert prototypes of different lengths. The only additional piece needed is a new internal conductor considering the length of each DUT.

This method of measurement does not consider the wake potential, as modelling the beam with a metallic rod (the inner conductor) implies forcing all emulated bunches to the

same potential. The RF Bead Pull method takes this problem into account [68]; however, the results of the coaxial waveguide setup provide a fairly accurate estimation with a significantly faster measurement process.

The prototype stripline PU was inserted in the test bench in order to evaluate its frequency response (Figure 5.20). By means of a VNA, the E5071-C model by Agilent® (Keysight Technologies®) [69], the $S_{21}$ parameter was measured between the upstream end of the coaxial waveguide and one of the ports of the PU. The downstream end of the coaxial waveguide, as well as the three remaining PU ports, was loaded with 50 Ω to maintain a matched characteristic impedance all along the test bench (Figure 5.21). A frequency sweep between 10 kHz (close to DC) and 20 GHz allowed to measure the frequency response of the PU in the range of interest.

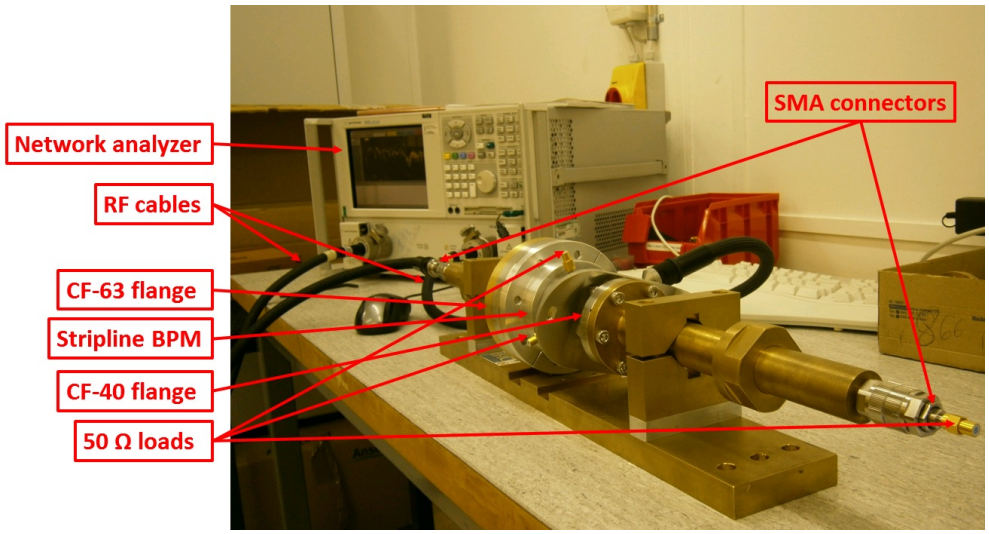


Figure 5.20: Measurement of the prototype stripline BPM frequency response.

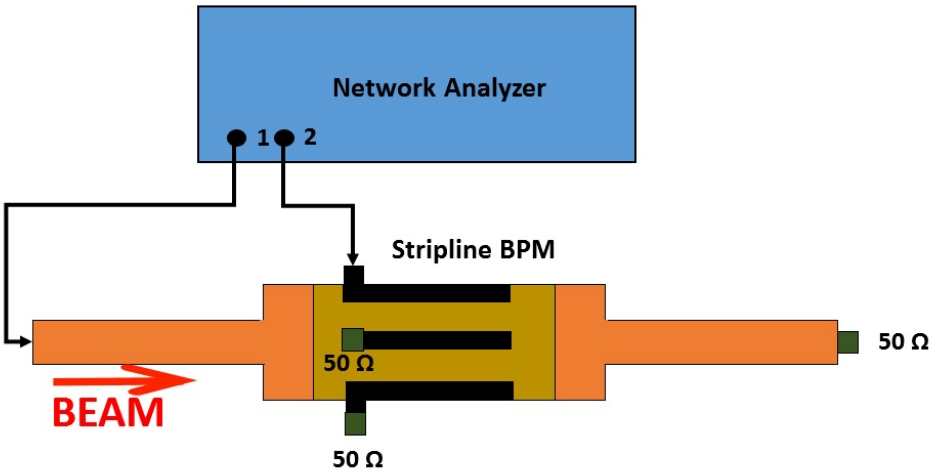


Figure 5.21: Block diagram of the test bench for high-frequency characterization of the prototype stripline BPM.

### 5.2.3 Results

Figure 5.22 represents the measured frequency response with the previously described settings (green trace) and the theoretical frequency response (blue trace) of the prototype stripline BPM. It is possible to observe that the two first minima of the transfer function, which should be located at 6 GHz and 12 GHz, as seen in Chapter 3, section 3.1, have been displaced to lower frequencies, at 4.48 GHz and 7.34 GHz, respectively. In addition, all the sine lobes of the stripline transfer function from the second one are distorted, pointing to high-order effects on the BPM. These two factors result in an extremely poor rejection of the 12 GHz frequency component, of about 4 dB (green trace), while the theoretical rejection value should be of about 40 dB (blue trace).

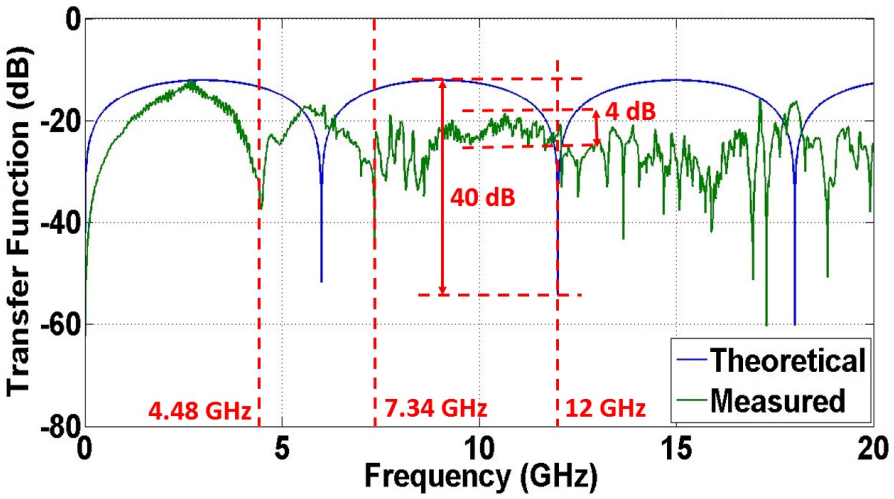


Figure 5.22: Theoretical (blue trace) and measured (green trace) transfer function of the prototype stripline BPM.

The displacement of the maxima and minima of the transfer function to lower frequencies indicates a bigger effective electrical length of the stripline electrodes, due to the insertion of the SiC ring, while the distortion of the lobes is due to unwanted resonances and high-order effects, as seen in Chapter 3, section 3.4.

An additional measurement was performed in the time domain using the low-frequency wire test bench described in section 5.1 in order to confirm the bigger effective electrical length of the electrodes observed with the coaxial testbench. The BPM was excited with a Gaussian pulse in order to measure the separation between the opposed polarity pulses in its impulse response. Instead of the expected 166.67 ps, as calculated in Chapter 3, section 3.2, the measured separation of the opposed polarity pulses was 239 ps (Figure 5.23), which hints towards an effective electrical length of 35.9 mm.

## 5.3 Conclusions

The obtained sensitivity and linearity values in the characterization tests with a thin wire are closer to the simulation results than to the theoretically expected ones using the linear approximation from Eq. (5.6), as summarized in Table 5.2. Charge accumulation

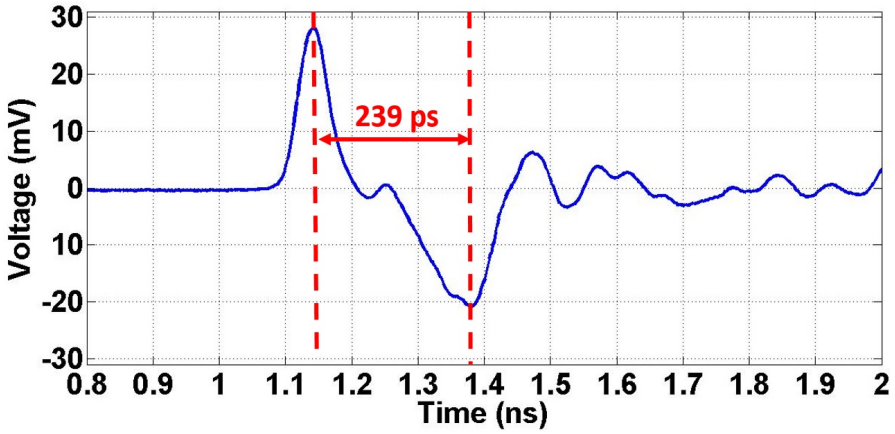


Figure 5.23: Response of the prototype stripline BPM to a Gaussian pulse excitation.

and impedance mismatches in the measurement setup are the most likely causes of this difference in sensitivity values.

The measured filtering properties of the PU at 12 GHz in the coaxial test bench are not the expected ones, as the rejection around this frequency is only of about 4 dB (Figure 5.22). In theory, this should not affect the electronic acquisition system, as the slopes of both the theoretical and the measured transfer functions tend to similar values in its operating bandwidth (0 to 40 MHz). However, the absence of high-frequency effects during the test with the thin wire does not allow to discard these effects with a real beam, as would be desirable, as no high frequency signals could be produced with this test bench. This aspect will be further studied during the tests with beam at CTF3, described in Chapter 6.

In order to improve the suppression of the 12 GHz frequency interference from the PETS, the distribution of the SiC rings and further geometrical aspects described in Chapter 3, section 3.4 should be improved in a new prototype.

# Chapter 6

# Beam Tests of the Prototype Stripline BPM System

Following the laboratory characterization of the first prototype stripline BPM, with short-circuited electrodes, detailed in Chapter 5, the system was installed in CTF3 to be tested with beam. Two types of tests have been performed: linearity/sensitivity and resolution. This chapter describes the installation of the prototype in CTF3, the beam configurations used for each test and presents the obtained results.

## 6.1 Installation in TBL at CTF3

The Test Beam Line (TBL) at CTF3, introduced in Chapter 1, section 1.3, has been designed as a scaled version (and proof of concept) of the CLIC DB decelerator, with the purpose of demonstrating the power generation technology needed for the CLIC two-beam acceleration scheme and validating all systems involved in the decelerator design, including the BPMs. Pulsed beams of 12 GHz bunching frequency, with a maximum current of 28 A and train durations between 140 and 242 ns (that of the CLIC Drive Beam) can be provided to the line. Further similarities between the TBL beam and the CLIC DB were shown in Table 1.2. TBL is, therefore, an excellent location to test the designed stripline prototype with beam.

TBL consists of 8 FODO cells, each one implemented on a girder, with two periods containing a quadrupole (alternating types focusing F and defocusing D), a BPM and a PETS. The most appropriate location for the prototype stripline BPM would be immediately adjacent to the last installed PETS at the time of the tests: the one at position 0820 in girder 8. For operation considerations, however, a quadrupole and a TBL inductive BPM needed to remain installed in between, at positions 0840 and 0850, respectively. The final installation scheme is shown in Figure 6.1, (a). The chosen location for the prototype under test is 0860, downstream of an inductive BPM (position 0850) and upstream of an F-type quadrupole (position 0900). Figure 6.1, (b), shows the installation area with the prototype stripline BPM and its upstream neighboring elements.

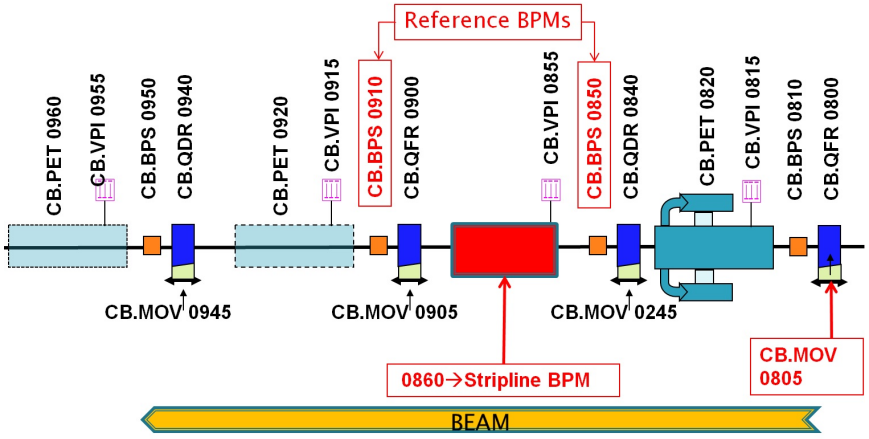


(a)

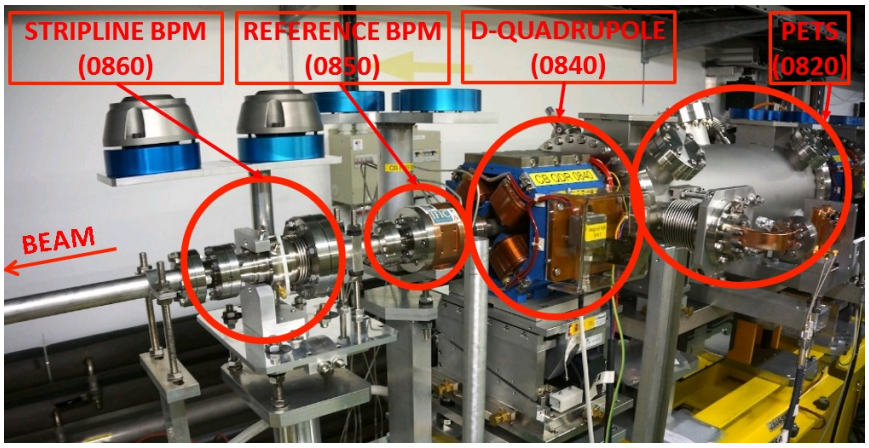


(b)

Figure 6.1: Diagram (a) and view (b) of the TBL cells around the installation location for the prototype stripline BPM.

## 6.2 Linearity and sensitivity parameters

The goal of this test is to study the behavior of the BPM and the influence of the interfering signals coming from the PETS at the beam bunching frequency (12 GHz) on the position measurement. For this purpose, the test will be conducted using two different beam configurations: high and low current, corresponding to high and low extracted PETS power values at 12 GHz, respectively.

In order to evaluate the linearity and sensitivity parameters of the prototype, the F-type quadrupole at position 0800 will be moved in both the horizontal and the vertical planes, so that the induced beam displacements can be observed at position 0860. The beam will be steered in a range of approximately ±5 mm for each plane, displacing the F-type quadrupole at position 0800, using the mover at position 0805 as actuator. The TBL inductive BPMs [7] that will provide the reference readings for the calculation of the expected positions are those located at positions 0850 and 0910.

Two different test rounds were conducted. In the first one, for mechanical considerations, it was not possible to install the stripline BPM at position 0860 so that its electrodes

would be oriented with the $x, y$ axes, but rotated by 45°. This aspect was corrected for the following CTF3 run, in which a second test was carried out with the electrodes oriented with the $x, y$ axis. The available beam current and extracted PETS power values were, however, different from those used in the first test.

### 6.2.1 Test with 45° rotated electrodes

#### 6.2.1.1 Test beams

In this test, the values used for the high and low beam current configurations were 22 A and 10 A, corresponding to 60 MW and 6 MW extracted PETS power values at 12 GHz, respectively. The length of the pulse train was 140 ns for the high current beam and 242 ns for the low current one. Figure 6.2 shows the current measurements of both test beams performed by the TBL inductive BPM at position 0850. The beam parameters for both configurations are summarized in Table 6.1.

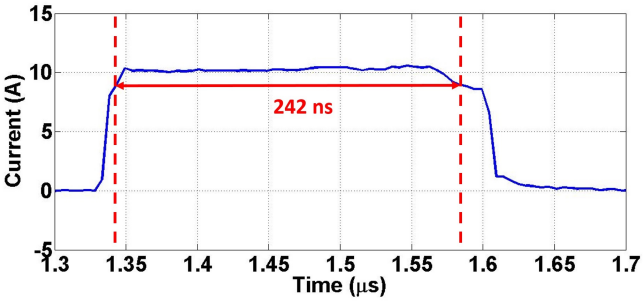


(a)

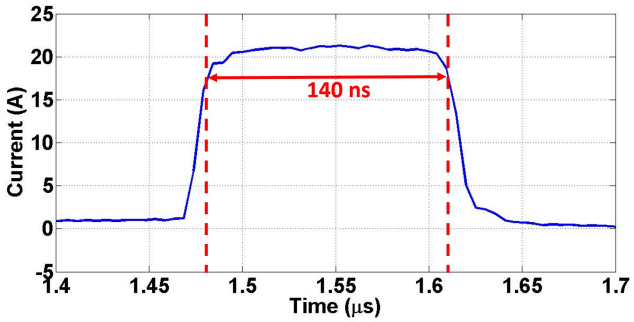


(b)

Figure 6.2: Current measurement of the test beams for the low (a) and high (b) extracted PETS power configurations used with the 45° rotated prototype.

| Parameter [unit] | Symbol | LP | HP |
|---|---|---|---|
| Extracted PETS power [MW] | $P_{\mathrm{PETS}}$ | 6 | 60 |
| Beam current [A] | $I_{\mathrm{beam}}$ | 10 | 22 |
| Pulse train duration [ns] | $t_{\mathrm{pulse}}$ | 242 | 140 |

Table 6.1: Beam properties for both low and high extracted PETS power test configurations used with the 45° rotated prototype.

#### 6.2.1.2 Simulation of the test scenario

As described in Chapter 4, section 4.1, the horizontal and the vertical positions can be estimated theoretically as:

$$x = \frac{R}{2} \cdot \left(\frac{\Delta}{\Sigma}\right)_H \qquad y = \frac{R}{2} \cdot \left(\frac{\Delta}{\Sigma}\right)_V \tag{6.1}$$

where $R$ is the vacuum pipe radius, and $(\Delta/\Sigma)_{H,V}$ are the difference-over-sum ratios of the voltage signals detected for each extreme of the horizontal and vertical axis, respectively. In the case of a BPM installation with 45° rotated electrodes, these ratios can be mathematically expressed as:

$$\left(\frac{\Delta}{\Sigma}\right)_H = \frac{(V_{UR} + V_{DR}) - (V_{UL} + V_{DL})}{V_{UR} + V_{DR} + V_{UL} + V_{DL}} \qquad \left(\frac{\Delta}{\Sigma}\right)_V = \frac{(V_{UL} + V_{UR}) - (V_{DL} + V_{DR})}{V_{UR} + V_{DR} + V_{UL} + V_{DL}} \tag{6.2}$$

The theoretical value of the sensitivity calculated for a stripline PU with axis-oriented electrodes in Chapter 5 as $S_{H,V} = \frac{2}{R}$ is 166.67 $m^{-1}$. When the PU is installed with 45° rotated electrodes (Figure 6.3), the sensitivity along the tranformed axis $x'$ can be theoretically estimated considering $x = x' \cos 45° = x'/\sqrt{2}$ and the following identities:

$$x = S_x \cdot \left(\frac{\Delta}{\Sigma}\right) \qquad x' = S'_x \cdot \left(\frac{\Delta}{\Sigma}\right) \tag{6.3}$$

which lead to $S'_x = S_x/\sqrt{2} = 117.9$ $m^{-1}$. This value will be shown in Table 6.3 for comparison.

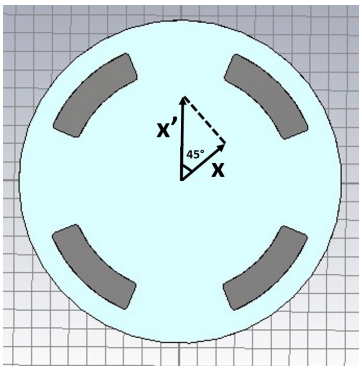


Figure 6.3: Change of coordinate axes from $x$ to $x'$ in a 45° rotated stripline PU.

This estimation is a first approximation that does not take into account several aspects of the BPM, such as the specific geometry of the electrodes. In a similar procedure as described for a PU with axis-oriented electrodes in Chapter 5, section 5.1, a 2D simulation of the 45° rotated PU geometry with the CST Studio Electrostatic Solver provides a more accurate estimation of the difference-over-sum ratio as the beam moves off the center in one or both coordinate planes.

Firstly, the cross-section of the PU geometry is modeled and one of the electrodes, for example, the up-left one, is set to a normalized potential of 1 V, leaving the other three ones at 0 V, as shown in Figure 6.4. The result of this simulation is the distribution of the potential in both the vertical and the horizontal directions along the cross-section. This is represented in Figure 6.5, (a). As the geometry of the prototype stripline PU is symmetric with respect to the $x$ and $y$ axes, the result data matrix from the simulation corresponding to the upper-left electrode can be rotated 90°, 180° and 270° with mathematical software (in our case MATLAB®), obtaining the distribution of the potential for the down-left, down-right and up-right electrodes, respectively, without repeating the simulation. Figure 6.5, (b), illustrates the distribution of the potential for the down-left electrode.

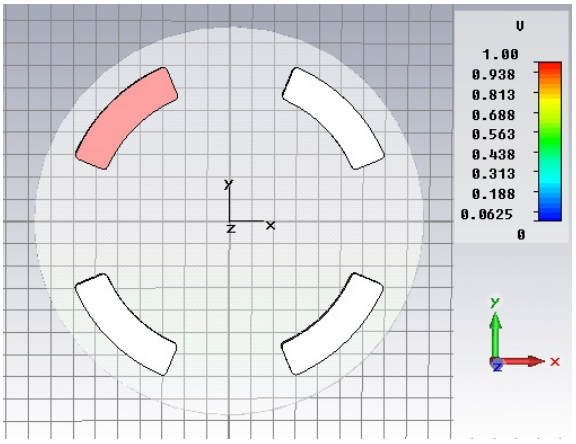


Figure 6.4: Simulation model with the potential in the up-left electrode set to 1 V.

Using Eqs. (6.2) with the four potential data matrices, it is possible to obtain the difference-over-sum ratio in the whole cross-section ($XY$ plane, $\vec{z}$ being the propagation direction of the beam). The results are plotted in Figure 6.6.

At this point, it is possible to extract the curves for $x = 0$ and $y = 0$ (dashed lines in Figure 6.6), obtaining the simulated difference-over-sum signal values for the intended movement directions of the beam. The results are shown in Figure 6.7. The curve is the same for the horizontal and the vertical axis. The value of the slope at the origin is 101.8 $\mathrm{m}^{-1}$, which is also about $\sqrt{2}$ times smaller than the simulated sensitivity in Chapter 5 for a stripline PU without rotation (137.01 $\mathrm{m}^{-1}$). This result will also be shown in Table 6.3 for comparison.

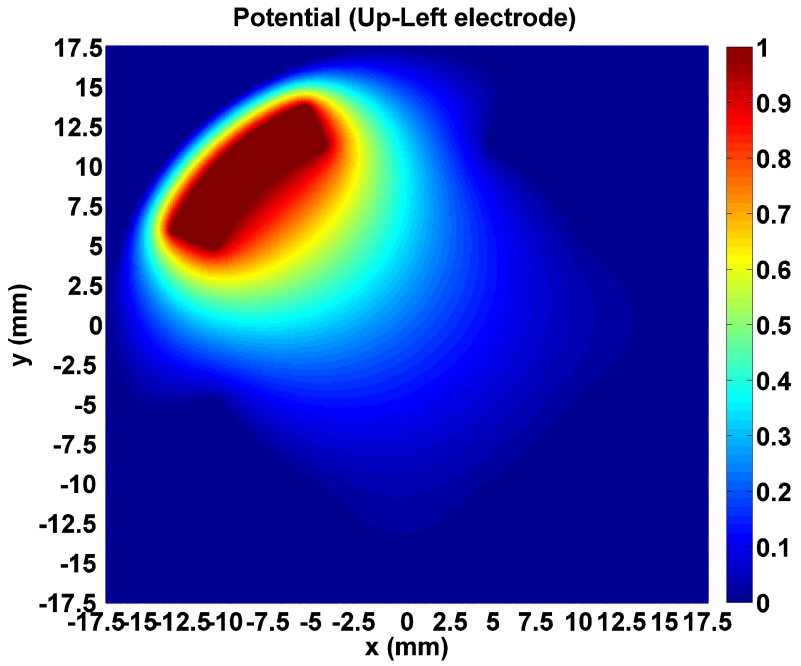


(a)

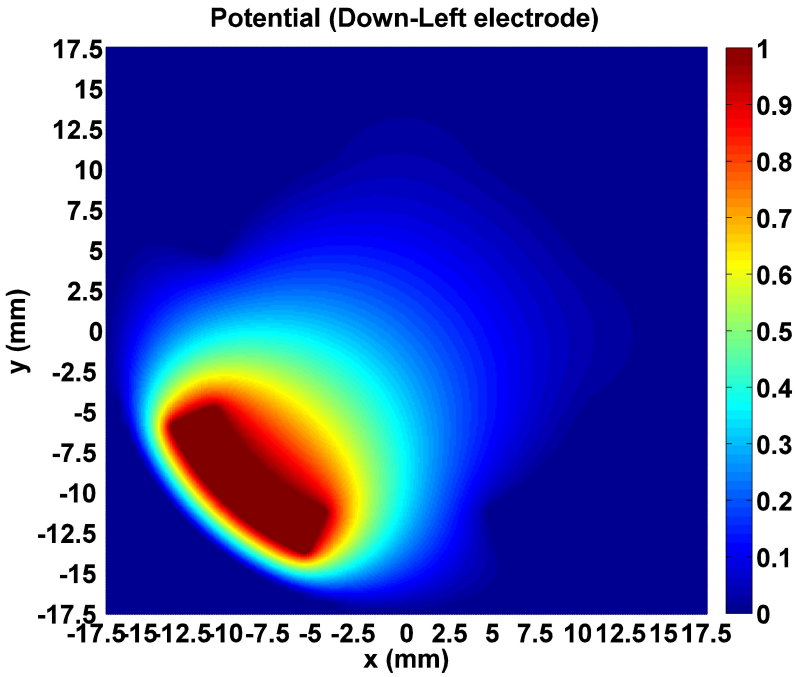


(b)

Figure 6.5: Distribution of the potential in both directions of the cross-section of the stripline PU due to the up-left (a) and down-left (b) electrode being set to 1 V.

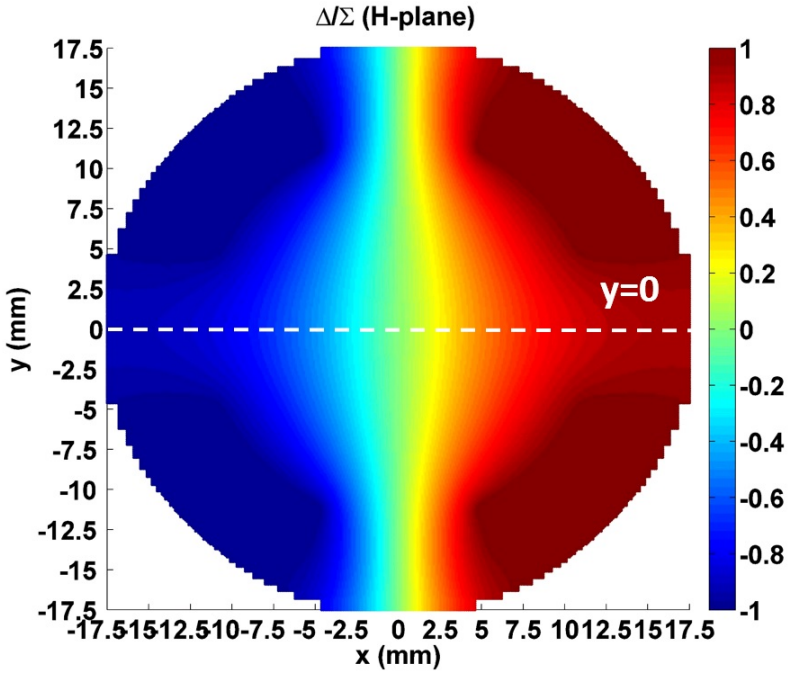


(a)

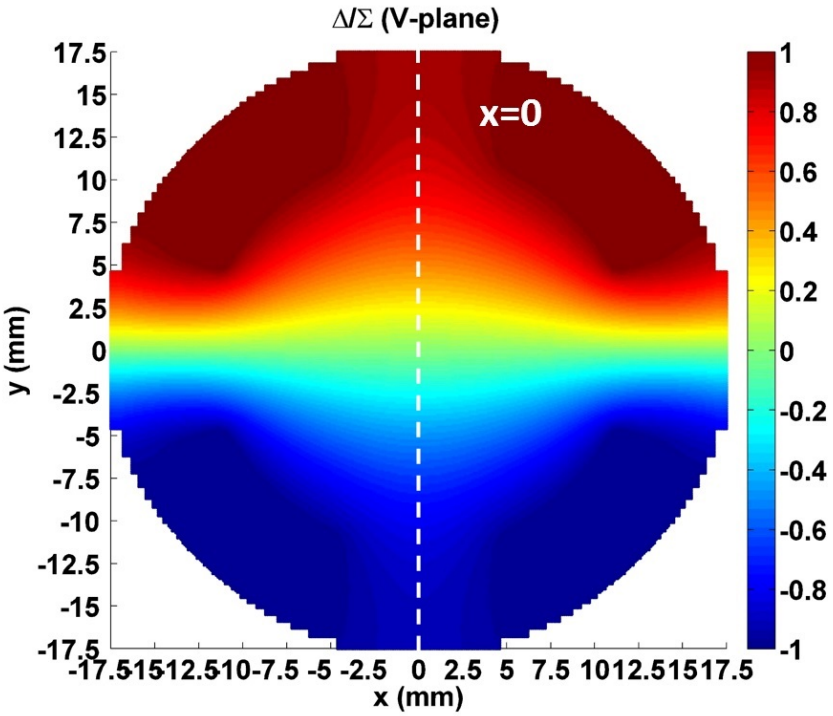


(b)

Figure 6.6: Difference-over-sum ratio in the BPM cross-section for the horizontal (a) and the vertical (b) plane.

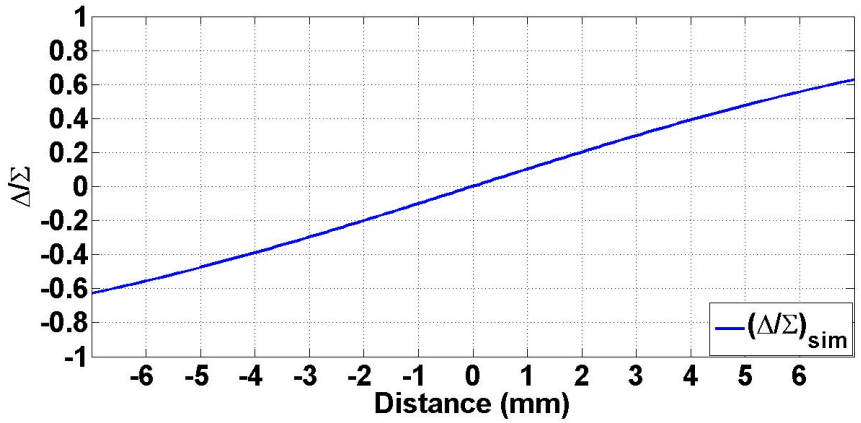


Figure 6.7: Simulated difference-over-sum signal curve for beam displacements along the $x$ ($y = 0$) and $y$ ($x = 0$) axes.

#### 6.2.1.3 Results

The passage of the beams described in subsection 6.2.1.1 of this chapter produces the output signals shown in Figure 6.8 for the low and high extracted PETS power configurations, when the beams are centered. These signals have the same shape as the simulated ones in Chapter 4, section 4.2, for a wide variety of beam configurations (Figure 4.10), coinciding also with the obtained ones in the characterization tests with wire (detailed in Chapter 5). In the high extracted PETS power test configuration, the 26 dB attenuator described in Chapter 4, section 4.2, was switched on during the acquisition of the signals to prevent the saturation of the ADC.

In order to test the sensitivity and linearity parameters of the prototype, the beam was steered in both axes, $x$ and $y$, for different position settings of the quadrupole at position 0800 and the mover at position 0805, within a range of, approximately, -6 to 4 mm. As expected, the shape of the output signals is maintained for all tested positions, the amplitude for each channel depending only on the distance from its corresponding electrode, demonstrating the correct performance of the designed acquisition scheme. Figures 6.9 and 6.10 show the output signals for all four positions on the coordinate axes at a distance of 4 mm from the center in the low extracted PETS power test configuration and of 3 mm from the center in the high extracted PETS configuration, respectively. The amplitude variation is of about 0.7 dB/mm in the first and of about 0.9 dB/mm in the second case.

The measured position by the stripline BPM is extracted using Δ/Σ processing, following the same procedure explained in Chapter 5, section 5.1. Combining Eqs. (6.1) and (6.2), it is possible to estimate the position in an installation with 45° rotated electrodes as:

$$x = \frac{R}{2} \cdot \left(\frac{\Delta}{\Sigma}\right)_H = \frac{(S_{UR} + S_{DR}) - (S_{UL} + S_{DL})}{S_{UR} + S_{DR} + S_{UL} + S_{DL}}$$
$$y = \frac{R}{2} \cdot \left(\frac{\Delta}{\Sigma}\right)_V = \frac{(S_{UL} + S_{UR}) - (S_{DL} + S_{DR})}{S_{UR} + S_{DR} + S_{UL} + S_{DL}} \tag{6.4}$$

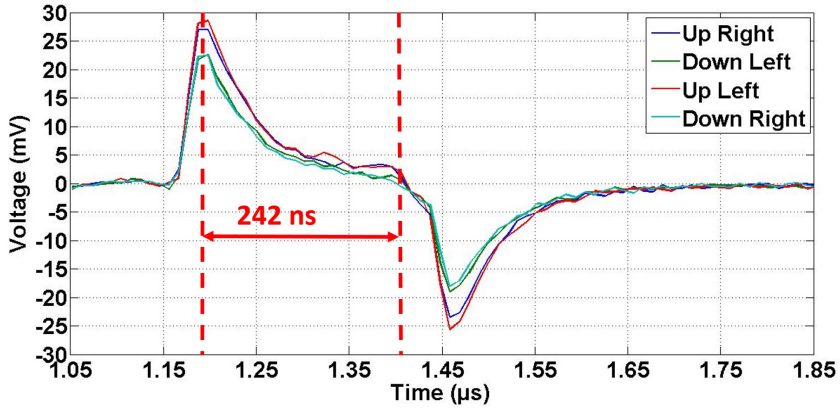


(a)

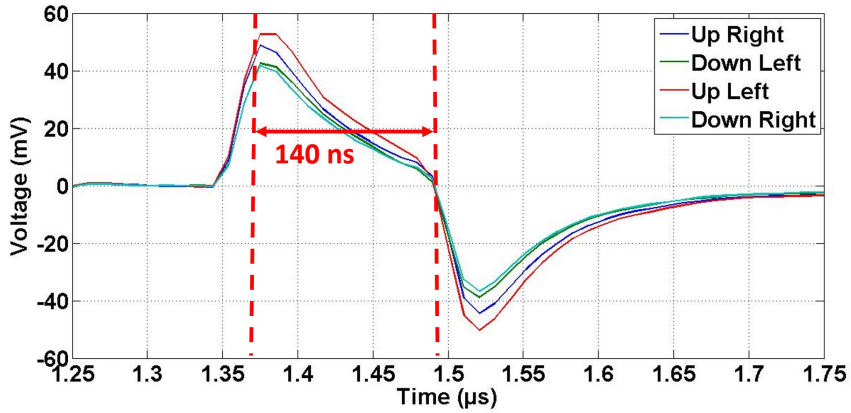


(b)

Figure 6.8: Output waveforms of the electronics produced by the passage of a centered beam in the low (a) and high (b) extracted PETS power test configuration in the prototype installation with 45° rotated electrodes.

where $R$ is the beam pipe radius, $\left(\frac{\Delta}{\Sigma}\right)_{H,V}$ is the difference-over-sum ratio of the signals detected in the extremes of the horizontal and vertical planes, respectively, and $S_i$, $i = (UR, UL, DL, DR)$ is the metrics from the $i^{th}$ electrode used for the position calculation. Similarly as in the wire tests described in Chapter 5, the area under the positive semi-pulse of the waveforms is chosen as metrics, considering 5% of the peak voltage value as threshold (Figure 5.14), and input in Eq. (6.4). As the BPM output signals have been already digitized with $f_{\text{sample}}$ as sampling rate, the area $S_i$ under each signal $v_i[n]$ can be calculated as:

$$S_i = \sum_{n=N_{\text{start}}}^{N_{\text{end}}} v_i[n] \cdot T_{\text{sample}} \tag{6.5}$$

where $N_{\text{start}}$, $N_{\text{end}}$ are the extremes of the integration interval and $T_{\text{sample}} = 1/f_{\text{sample}}$ is the sampling period.

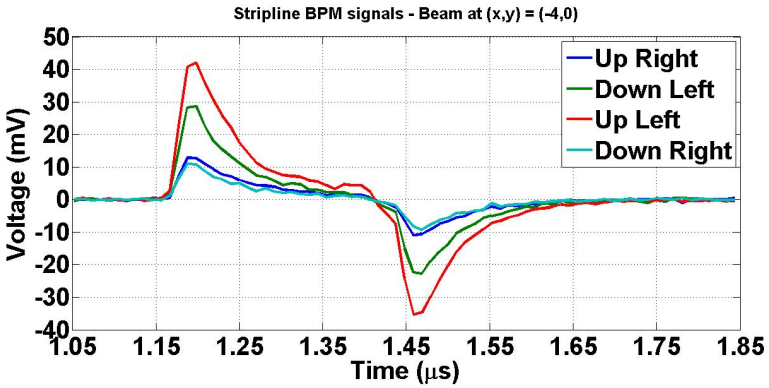


(a) (x,y) = (-4,0)

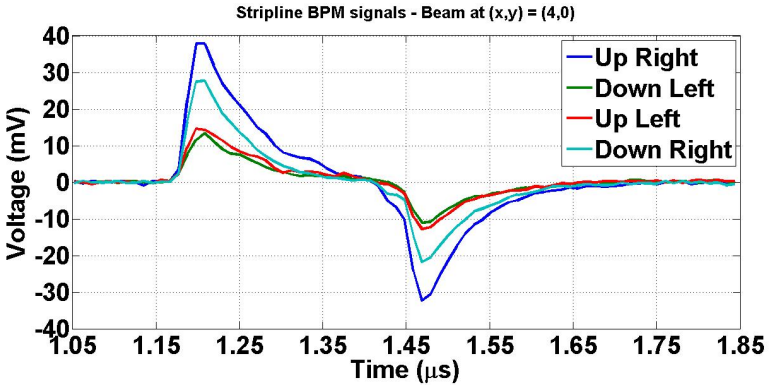


(b) (x,y) = (4,0)

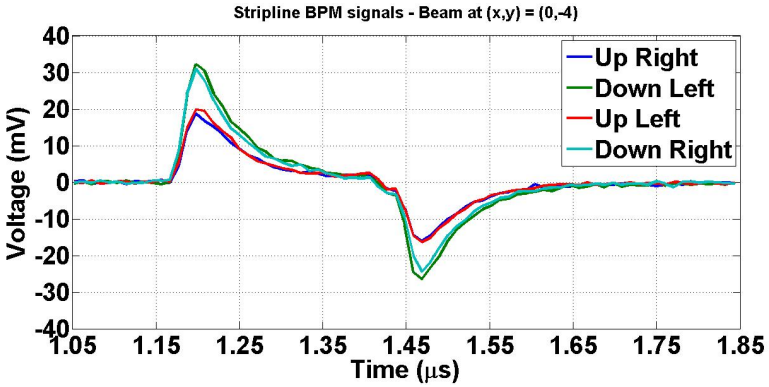


(c) (x,y) = (0,-4)

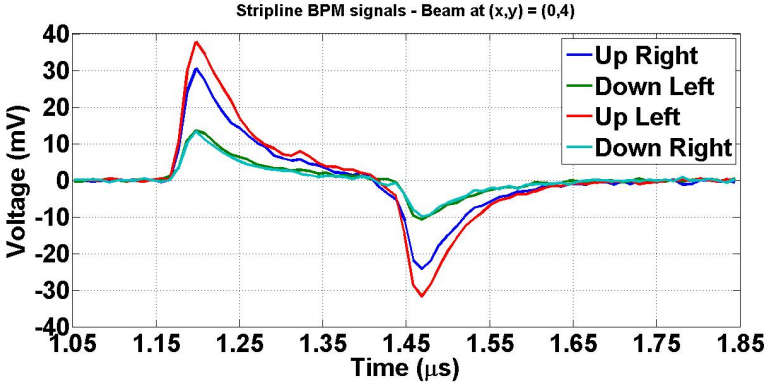


(d) (x,y) = (0,4)

Figure 6.9: Output waveforms of the electronics produced by the low current test beam at a distance of 4 mm off the center in the 45° rotated prototype.

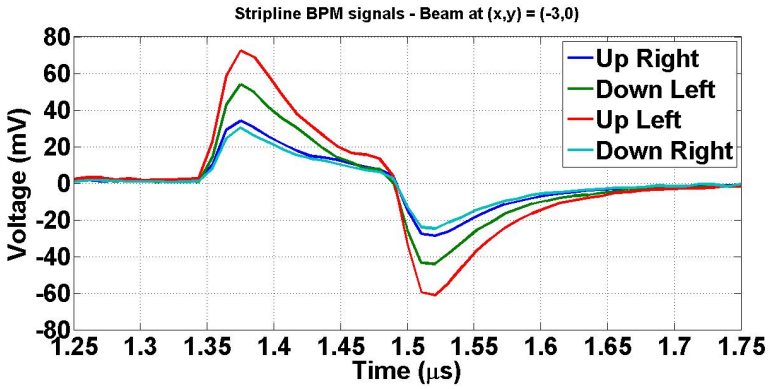


(a) (x,y) = (-3,0)

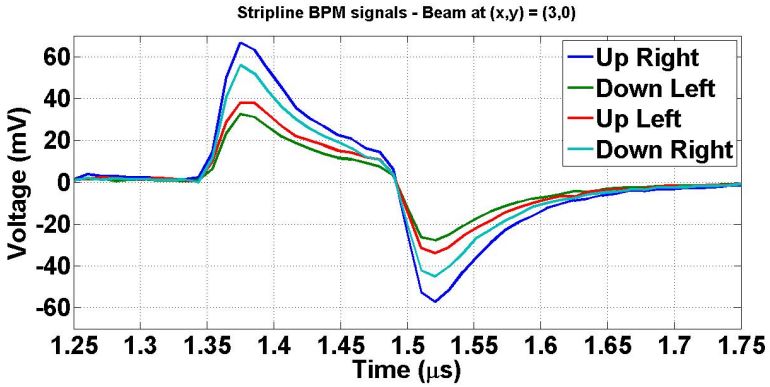


(b) (x,y) = (3,0)

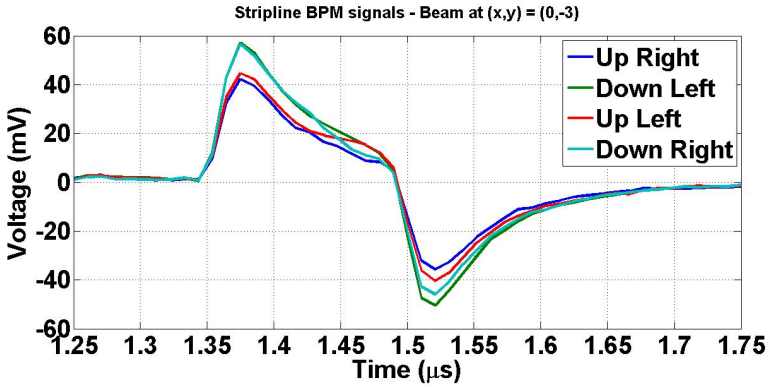


(c) (x,y) = (0,-3)

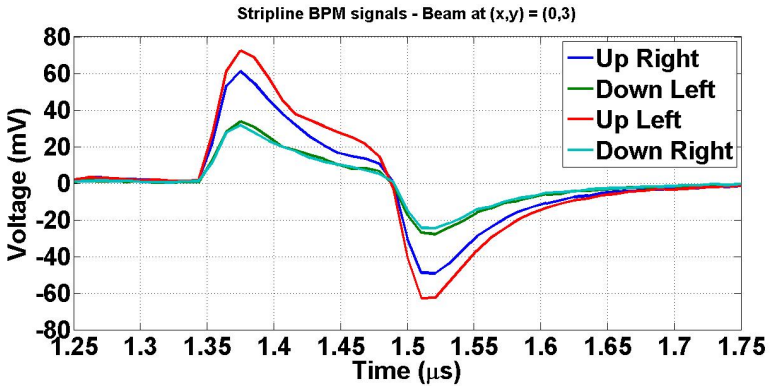


(d) (x,y) = (0,3)

Figure 6.10: Output waveforms of the electronics produced by the high current test beam at a distance of 3 mm off the center in the 45° rotated prototype.

The linearity and sensitivity parameters are given by:

$$x, y \;=\; (S_{H,V}^{-1}) \cdot \left(\frac{\Delta}{\Sigma}\right)_{H,V} + EOS_{H,V} \tag{6.6}$$

where $S_{H,V}$ is the sensitivity and $EOS_{H,V}$ is the electrical offset. Another important parameter is $\sigma_{H,V}$, the contribution, for each plane, of the nonlinearity to the overall precision, giving the uncertainty in the position measurements. The sensitivity and the electrical offset are obtained from the linear fit between the reference beam positions, calculated from the measured positions by the TBL inductive BPMs at locations 0850 and 0910, and the values of $\left(\frac{\Delta}{\Sigma}\right)_{H,V}$ measured by the stripline BPM. The contribution of the nonlinearity to the overall precision is calculated as the r.m.s. value of the linearity error, that is, the difference between the reference positions and the measured positions by the stripline BPM. The measured sensitivity curves for both low and high extracted PETS power configurations are represented in Figure 6.11 for the vertical and the horizontal planes. The values of the reference positions and the measured $\Delta/\Sigma$ for the vertical and the horizontal planes are shown in Table 6.2 for the low and the high extracted PETS power configurations. The parameters of the linear fit for both planes as expressed in Eq. (6.6) are shown in Table 6.3 for both low and high extracted PETS power configurations.

#### 6.2.1.4 Discussion

The measured sensitivities for each plane (Table 6.3) experience a ±4% variation upon the increase of the extracted PETS RF power from 6 to 60 MW. The measured horizontal sensitivity values (98.1 $m^{-1}$ and 94.2 $m^{-1}$ for 6 and 60 MW, respectively) remain close to the simulated value of 101.8 $m^{-1}$, while the vertical sensitivity was found systematically lower (72.4 $m^{-1}$ and 75.3 $m^{-1}$ for 6 and 60 MW, respectively). A possible reason for this result could be the presence of an active F-type quadrupole at position 0900, between the two reference BPMs used for this test, located at positions 0850 and 0910. F-type quadrupoles focus the beam in the horizontal plane, defocussing it in the vertical one. This could affect the vertical position reading of the downstream reference BPM (0910), and therefore the calculated value of the expected vertical position. In order to avoid this effect, another test was attempted switching off the quadrupole, not being possible to operate in these conditions without losing the beam.

Finally, a decrease in the electrical offset was observed in the high-power test configuration for the coordinate not being swept (Figure 6.11). In addition, for this coordinate in both the high- and low-power test configurations, a tilt was observed, of 5 mrad for the horizontal plane and 7 mrad for the vertical one.

### 6.2.2 Test with axis-oriented electrodes

#### 6.2.2.1 Test beams

In this test, the values used for the high and low beam current configurations were 12 A and 3.5 A, corresponding to 27 MW and 3.5 MW extracted PETS power values at 12 GHz, respectively. The length of the pulse train was of about 242 ns for both configurations. Figure 6.12 shows the current measurement of both test beams performed by the TBL inductive BPM at position 0850. It is possible to observe in Figure 6.12, (a) that the

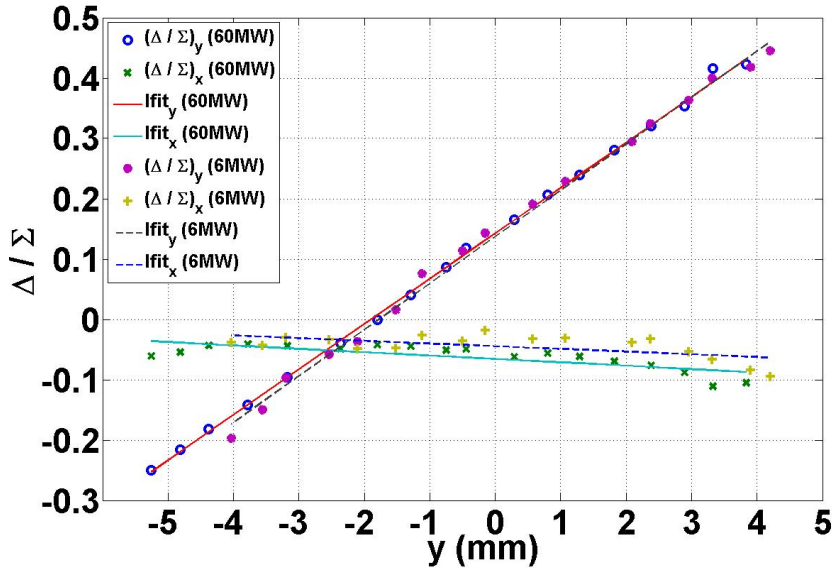


(a)

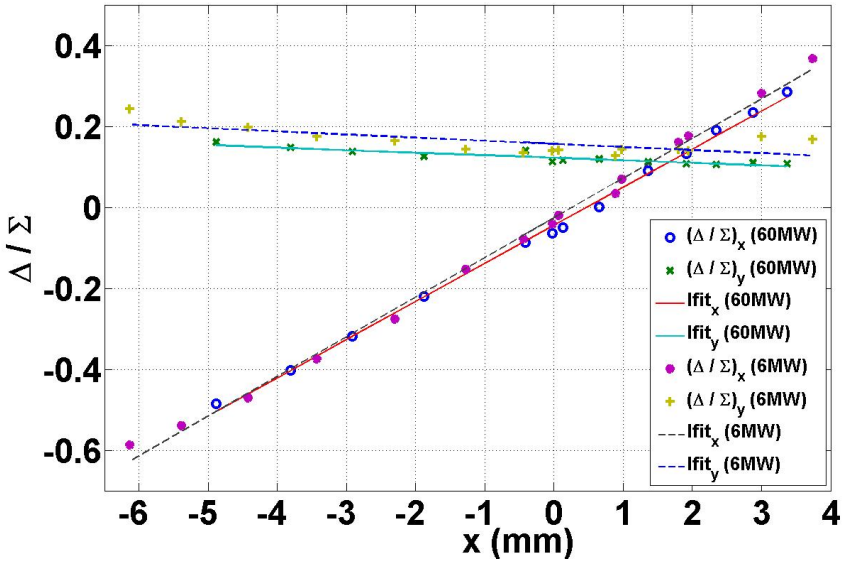


(b)

Figure 6.11: Dependency of the difference-over-sum ratio on the beam displacement in the vertical (a) and horizontal (b) planes for extracted PETS RF power values of 6 MW (dashed lines) and 60 MW (solid lines) for the stripline BPM installation with 45° rotated electrodes.

| **Reference beam position [m]** | $(\Delta/\Sigma)_V$ | **Reference beam position [m]** | $(\Delta/\Sigma)_H$ |
|---|---|---|---|
| **Vertical LP** | | **Horizontal LP** | |
| -4.0325 $\cdot 10^{-3}$ | -0.1972 | -6.1328 $\cdot 10^{-3}$ | -0.5869 |
| -3.5522 $\cdot 10^{-3}$ | -0.1496 | -5.3830 $\cdot 10^{-3}$ | -0.5384 |
| -3.1949 $\cdot 10^{-3}$ | -0.0968 | -4.4201 $\cdot 10^{-3}$ | -0.4699 |
| -2.5426 $\cdot 10^{-3}$ | -0.0580 | -3.4331 $\cdot 10^{-3}$ | -0.3742 |
| -2.1073 $\cdot 10^{-3}$ | -0.0367 | -2.3013 $\cdot 10^{-3}$ | -0.2755 |
| -1.5169 $\cdot 10^{-3}$ | 0.0155 | -1.2797 $\cdot 10^{-3}$ | -0.1525 |
| -1.1231 $\cdot 10^{-3}$ | 0.0758 | -0.4399 $\cdot 10^{-3}$ | -0.0779 |
| -0.5046 $\cdot 10^{-3}$ | 0.1136 | -0.0235 $\cdot 10^{-3}$ | -0.0403 |
| -0.1539 $\cdot 10^{-3}$ | 0.1431 | 0.0626 $\cdot 10^{-3}$ | -0.0184 |
| 0.5698 $\cdot 10^{-3}$ | 0.1906 | 0.8896 $\cdot 10^{-3}$ | 0.0347 |
| 1.0737 $\cdot 10^{-3}$ | 0.2284 | 0.9800 $\cdot 10^{-3}$ | 0.0710 |
| 2.0921 $\cdot 10^{-3}$ | 0.2653 | 1.8002 $\cdot 10^{-3}$ | 0.1619 |
| 2.3713 $\cdot 10^{-3}$ | 0.2943 | 1.9431 $\cdot 10^{-3}$ | 0.1775 |
| 2.9548 $\cdot 10^{-3}$ | 0.3246 | 3.0009 $\cdot 10^{-3}$ | 0.2830 |
| 3.3139 $\cdot 10^{-3}$ | 0.3630 | 3.7433 $\cdot 10^{-3}$ | 0.3687 |
| 3.9048 $\cdot 10^{-3}$ | 0.3996 | | |
| 4.2030 $\cdot 10^{-3}$ | 0.4185 | | |
| **Vertical HP** | | **Horizontal HP** | |
| -5.2540 $\cdot 10^{-3}$ | -0.2521 | -4.8804 $\cdot 10^{-3}$ | -0.4852 |
| -4.8095 $\cdot 10^{-3}$ | -0.2154 | -3.8135 $\cdot 10^{-3}$ | -0.4021 |
| -4.3750 $\cdot 10^{-3}$ | -0.1812 | -2.9129 $\cdot 10^{-3}$ | -0.3175 |
| -3.7788 $\cdot 10^{-3}$ | -0.1422 | -1.8825 $\cdot 10^{-3}$ | -0.2203 |
| -3.1738 $\cdot 10^{-3}$ | -0.0955 | -0.4094 $\cdot 10^{-3}$ | -0.0853 |
| -2.3606 $\cdot 10^{-3}$ | -0.0393 | -0.0228 $\cdot 10^{-3}$ | -0.0630 |
| -1.8010 $\cdot 10^{-3}$ | -0.0001 | 0.1289 $\cdot 10^{-3}$ | -0.0488 |
| -1.2865 $\cdot 10^{-3}$ | 0.0406 | 0.6556 $\cdot 10^{-3}$ | 0.0019 |
| -0.7538 $\cdot 10^{-3}$ | 0.0860 | 1.3644 $\cdot 10^{-3}$ | 0.0909 |
| -0.4421 $\cdot 10^{-3}$ | 0.1178 | 1.9103 $\cdot 10^{-3}$ | 0.1341 |
| 0.2871 $\cdot 10^{-3}$ | 0.1653 | 2.3490 $\cdot 10^{-3}$ | 0.1911 |
| 0.8048 $\cdot 10^{-3}$ | 0.2064 | 2.8735 $\cdot 10^{-3}$ | 0.2352 |
| 1.2930 $\cdot 10^{-3}$ | 0.2398 | 3.3722 $\cdot 10^{-3}$ | 0.2873 |
| 1.8214 $\cdot 10^{-3}$ | 0.2800 | | |
| 2.3822 $\cdot 10^{-3}$ | 0.3202 | | |
| 2.8970 $\cdot 10^{-3}$ | 0.3535 | | |
| 3.3309 $\cdot 10^{-3}$ | 0.4164 | | |
| 3.8399 $\cdot 10^{-3}$ | 0.4232 | | |

Table 6.2: Reference and measured positions in the vertical (left) and horizontal (right) planes for the low (top) and high (bottom) extracted PETS power test configuration for the 45° rotated prototype.

| Parameter | Measurement LP | Measurement HP | Theory | Simulation |
|---|---|---|---|---|
| **Vertical** | | | | |
| $S_V$ [m$^{-1}$] | $72.4 \pm 1.8$ | $75.3 \pm 0.6$ | 117.9 | 101.8 |
| $EOS_V$ [m] | $(-1.76 \pm 0.07) \cdot 10^{-3}$ | $(-1.91 \pm 0.02) \cdot 10^{-3}$ | 0.00 | 0.00 |
| $\sigma_V$ [m] | $250.42 \cdot 10^{-6}$ | $92.73 \cdot 10^{-6}$ | | |
| **Horizontal** | | | | |
| $S_H$ [m$^{-1}$] | $98.1 \pm 1.7$ | $94.2 \pm 1.4$ | 117.9 | 101.8 |
| $EOS_H$ [m] | $(0.24 \pm 0.05) \cdot 10^{-3}$ | $(-0.46 \pm 0.04) \cdot 10^{-3}$ | 0.00 | 0.00 |
| $\sigma_H$ [m] | $182.87 \cdot 10^{-6}$ | $120.00 \cdot 10^{-6}$ | | |

Table 6.3: Measured linearity and sensitivity parameters of the prototype stripline BPM for both high- and low-power test configurations in the installation with 45° rotated electrodes.

beam available for the low extracted PETS power configuration during this test round was unstable, particularly in the first half of the pulse. The beam parameters for both configurations are summarized in Table 6.4.

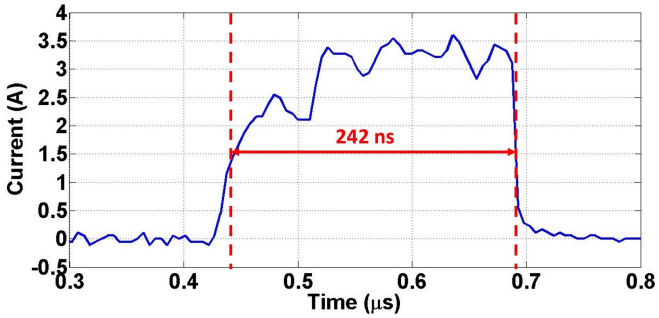


(a)

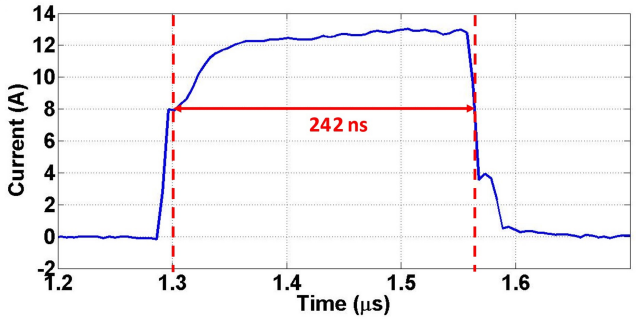


(b)

Figure 6.12: Current measurement of the test beam for the low (a) and high (b) extracted PETS power configuration used with the axis-oriented installation of the prototype.

#### 6.2.2.2 Test scenario

As for this second test the stripline PU was installed with axis-oriented electrodes, the scenario is the same as for the laboratory characterization tests described and simulated in Chapter 5, section 5.1. Therefore, theoretical and simulated sensitivity values of 166.67 m$^{-1}$

| Parameter [unit] | Symbol | LP | HP |
|---|---|---|---|
| Extracted PETS power [MW] | $P_{\mathrm{PETS}}$ | 2.4 | 27 |
| Beam current [A] | $I_{\mathrm{beam}}$ | 3.5 | 12 |
| Pulse train duration [ns] | $t_{\mathrm{pulse}}$ | 242 | 242 |

Table 6.4: Beam properties for both low power test configurations used with the axis-oriented installation of the prototype.

and 137.01 $\mathrm{m}^{-1}$, respectively, are expected. These values are shown in Table 6.6 for comparison.

#### 6.2.2.3 Results

The passage of the beams described in subsection 6.2.2.1 of this chapter produces the output signals shown in Figure 6.13 for the low and high extracted PETS power configurations, when the beams are centered. These signals have the same shape as the simulated ones in Chapter 4, section 4.2, for a wide variety of beam configurations (Figure 4.10), coinciding also with the obtained ones in the characterization tests with wire (detailed in Chapter 5). It is, however, possible to observe certain instabilities in the first semi-pulse of the output signals for the low extracted PETS power configuration (Figure 6.13), (a). These are caused by the observed instabilities in the test beam (Figure 6.12,(a)) and the ability of the electronic acquisition system to follow any beam deviation longer than 10 ns, its required time resolution. Similarly as in the tests for the installation with 45° rotated electrodes, in the high extracted PETS power test configuration the 26 dB attenuator described in Chapter 4, section 4.2, was switched on during the acquisition of the signals to prevent the saturation of the ADC.

In order to test the sensitivity and linearity parameters of the prototype in this installation, the beam was steered in both axes, $x$ and $y$, for different position settings of the quadrupole at position 0800 and the mover at position 0805, within a range of, approximately, -4 to 6 mm. As expected, the shape of the output signals is maintained for all tested positions, the amplitude for each channel depending only on the distance from its corresponding electrode, demonstrating the correct performance of the designed acquisition scheme. Figures 6.14 and 6.15 show the output signals for all four positions on the coordinate axes at a distance of 3 mm from the center in both low and high extracted PETS power configurations. The amplitude variation is of about 1.1 dB/mm in the first and of about 1.2 dB/mm in the second case.

The measured position by the stripline BPM is extracted using $\Delta/\Sigma$ processing. Similarly as in the characterization tests with wire described in Chapter 5, the position can be estimated as a function of the difference-over-sum ratio of the electrodes at the extreme of each axis as:

$$x = \frac{R}{2} \cdot \left(\frac{\Delta}{\Sigma}\right)_H = \frac{R}{2} \cdot \frac{S_{\mathrm{right}} - S_{\mathrm{left}}}{S_{\mathrm{right}} + S_{\mathrm{left}}}$$
$$y = \frac{R}{2} \cdot \left(\frac{\Delta}{\Sigma}\right)_V = \frac{R}{2} \cdot \frac{S_{\mathrm{up}} - S_{\mathrm{down}}}{S_{\mathrm{up}} + S_{\mathrm{down}}} \tag{6.7}$$

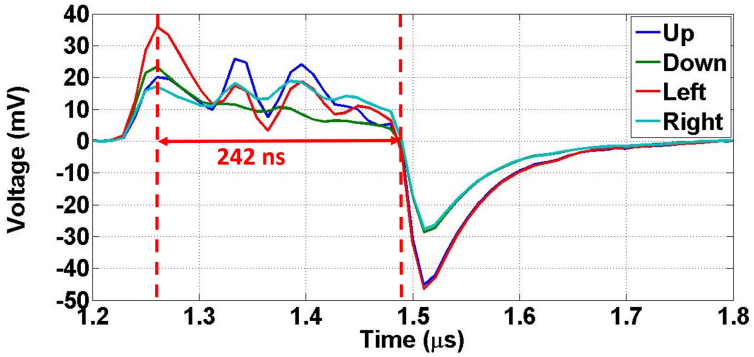


(a)

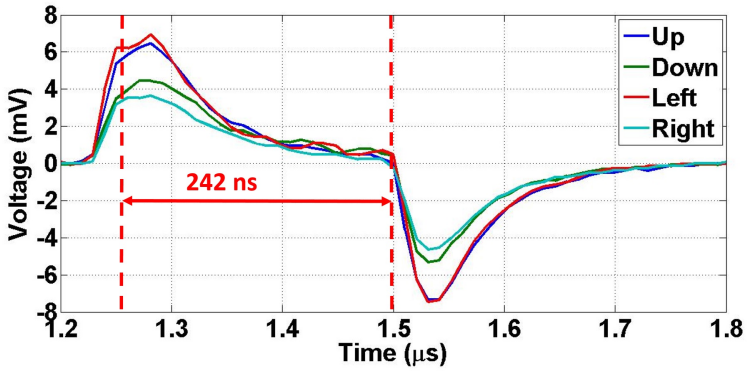


(b)

Figure 6.13: Output waveforms of the electronics produced by the passage of a centered beam in the low (a) and high (b) extracted PETS power test configuration in the prototype installation with axis-oriented electrodes.

where R is the beam pipe radius, $\left(\frac{\Delta}{\Sigma}\right)_{H,V}$ is the difference-over-sum ratio in the horizontal and vertical plane, respectively, and $S_i$, $i = (R, L, U, D)$ is the metrics from the $i^{th}$ electrode used for the position calculation. In this case, the area under the negative semi-pulse of the waveforms is computed as metrics, to prevent any effect of the instabilities observed in Figure 6.13, (a), on the position reading for the low extracted PETS power test configuration. A 5% of the peak voltage value $Vp$ is again taken as threshold.

The linearity and sensitivity parameters are given by:

$$x, y \;=\; (S^{-1}_{H,V}) \cdot \left(\frac{\Delta}{\Sigma}\right)_{H,V} + EOS_{H,V} \tag{6.8}$$

where $S_{H,V}$ is the sensitivity and $EOS_{H,V}$ is the electrical offset. Another important parameter is $\sigma_{H,V}$, the contribution, for each plane, of the nonlinearity to the overall precision, giving the uncertainty in the position measurements. The sensitivity and the electrical offset are obtained from the linear fit between the reference beam positions, calculated from the measured positions by the TBL inductive BPMs at locations 0850 and 0910, and the values of $\left(\frac{\Delta}{\Sigma}\right)_{H,V}$ measured by the stripline BPM. The contribution of the nonlinearity to the overall precision is calculated as the r.m.s. value of the linearity error, that is, the difference between the reference positions and the measured positions by the stripline

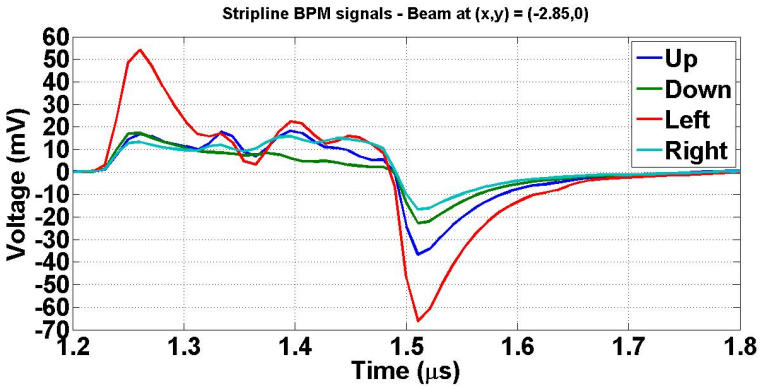


(a) (x,y) = (-3,0)

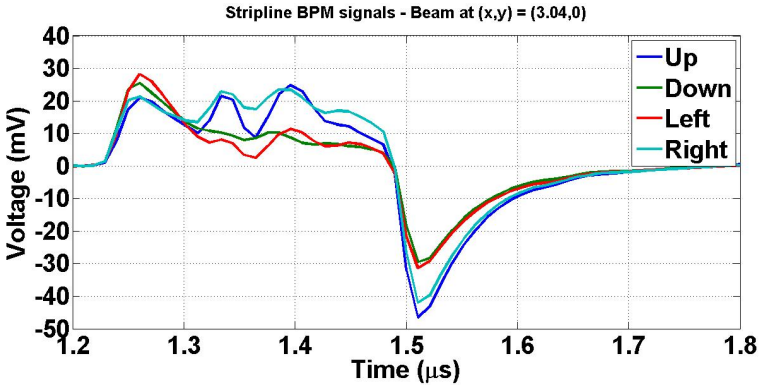


(b) (x,y) = (3,0)

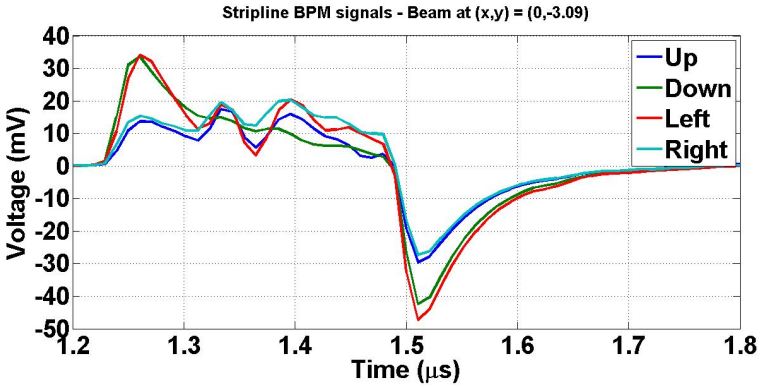


(c) (x,y) = (0,-3)

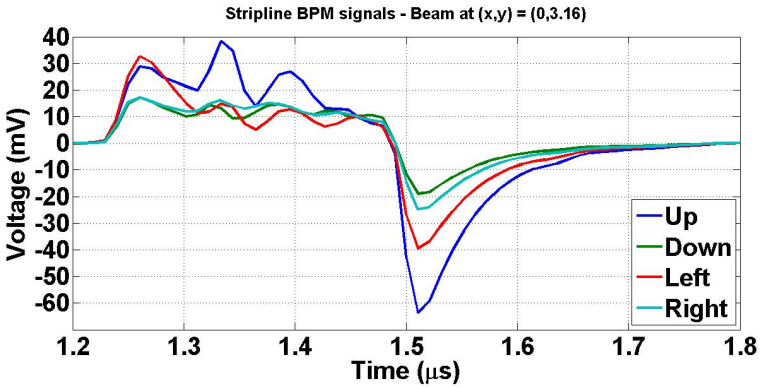


(d) (x,y) = (0,3)

Figure 6.14: Output waveforms of the electronics produced by the low current test beam at a distance of 3 mm off the center in the prototype installation with axis-oriented electrodes.

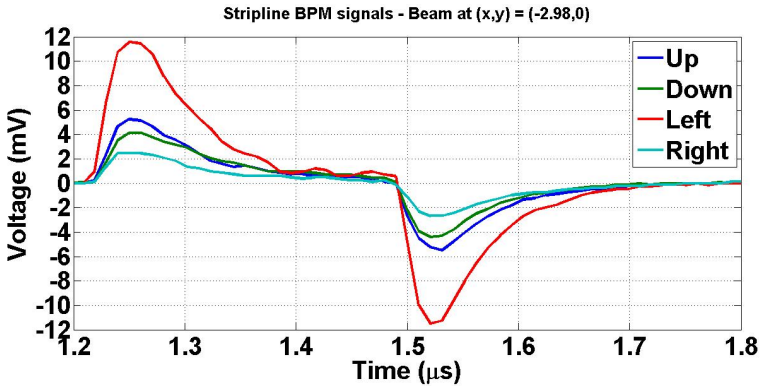


(a) (x,y) = (-3,0)

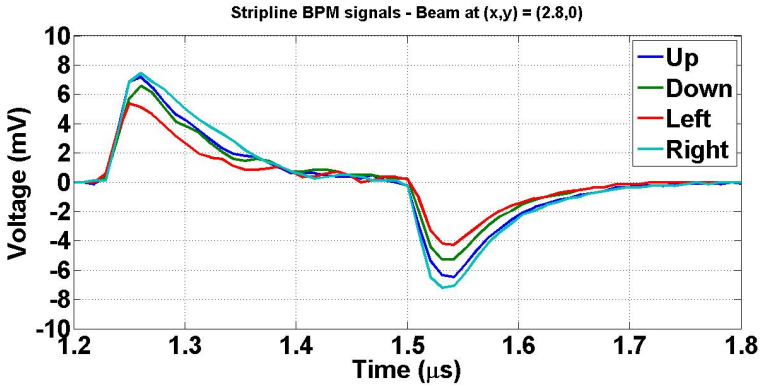


(b) (x,y) = (3,0)

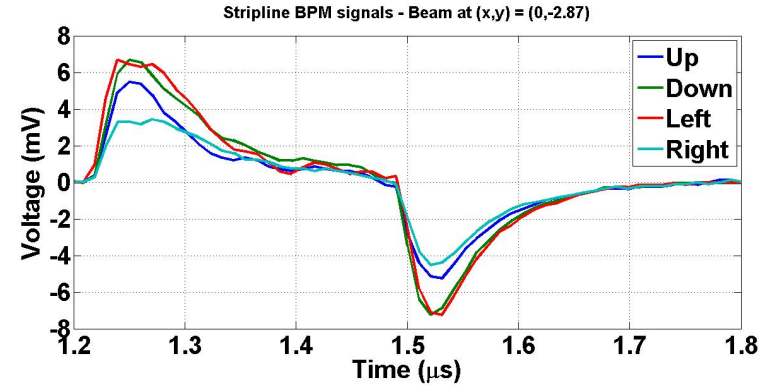


(c) (x,y) = (0,-3)

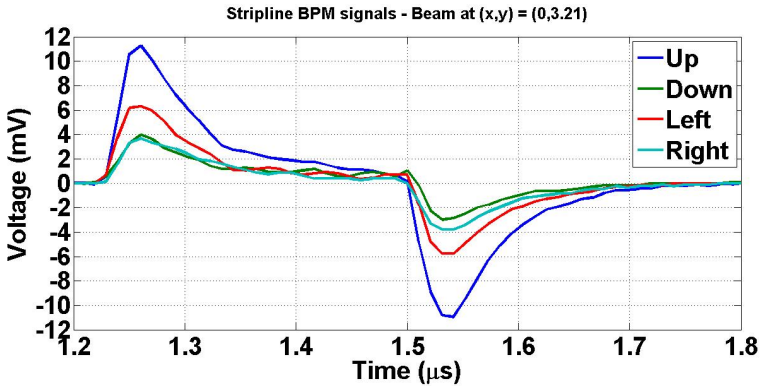


(d) (x,y) = (0,3)

Figure 6.15: Output waveforms of the electronics produced by the high current test beam at a distance of 3 mm off the center in the prototype installation with axis-oriented electrodes.

BPM. The measured sensitivity curves for both low and high extracted PETS power configurations are represented in Figure 6.16 for the vertical and the horizontal planes. The values of the reference positions and the measured $\Delta/\Sigma$ for the vertical and the horizontal planes are shown in Table 6.5 for the low and the high extracted PETS power configurations. The parameters of the linear fit for both planes as expressed in Eq. (6.8) are shown in Table 6.6 for both low and high extracted PETS power configurations.

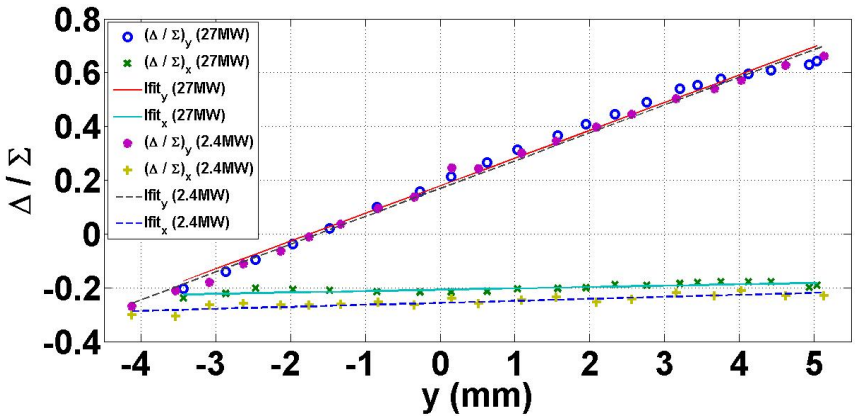


(a)

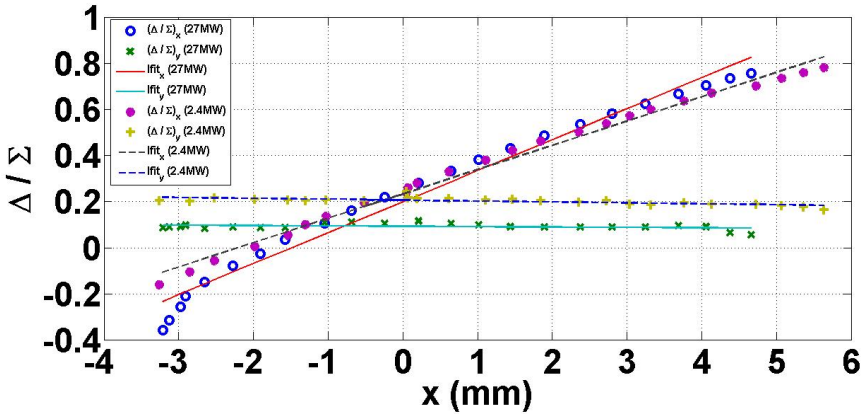


(b)

Figure 6.16: Dependency of the difference-over-sum ratio on the beam displacement in the vertical (a) and horizontal (b) planes for extracted PETS RF power values of 6 MW (dashed lines) and 60 MW (solid lines) for the stripline BPM installation with axis-oriented electrodes.

#### 6.2.2.4 Discussion

As in the test of the installation with 45° rotated electrodes, the measured vertical sensitivity has been found lower than the simulated value, 103.3 $m^{-1}$ instead of 137.01 $m^{-1}$. The F-type quadrupole at position 0900, between the two TBL inductive BPMs used as reference, is again thought to have an influence in the reference vertical positions read by the inductive BPM at position 0910. There are no further remarkable effects of the increase of the extracted PETS RF power on this parameter.

| **Reference beam position [m]** | $(\Delta/\Sigma)_V$ | **Reference beam position [m]** | $(\Delta/\Sigma)_H$ |
|---|---|---|---|
| **Vertical LP** | | **Horizontal LP** | |
| $-4.1271 \cdot 10^{-3}$ | -0.2704 | $-3.2590 \cdot 10^{-3}$ | -0.1612 |
| $-3.5373 \cdot 10^{-3}$ | -0.2104 | $-2.8483 \cdot 10^{-3}$ | -0.1059 |
| $-3.0881 \cdot 10^{-3}$ | -0.1799 | $-2.5219 \cdot 10^{-3}$ | -0.0564 |
| $-2.6308 \cdot 10^{-3}$ | -0.1117 | $-1.9800 \cdot 10^{-3}$ | 0.0059 |
| $-2.1358 \cdot 10^{-3}$ | -0.0647 | $-1.5375 \cdot 10^{-3}$ | 0.0551 |
| $-1.7532 \cdot 10^{-3}$ | -0.0112 | $-1.3037 \cdot 10^{-3}$ | 0.1003 |
| $-1.3323 \cdot 10^{-3}$ | 0.0364 | $-1.0251 \cdot 10^{-3}$ | 0.1359 |
| $-0.8289 \cdot 10^{-3}$ | 0.0955 | $-0.5139 \cdot 10^{-3}$ | 0.1960 |
| $-0.3420 \cdot 10^{-3}$ | 0.1377 | $0.0498 \cdot 10^{-3}$ | 0.2405 |
| $0.1565 \cdot 10^{-3}$ | 0.2456 | $0.0721 \cdot 10^{-3}$ | 0.2604 |
| $0.5115 \cdot 10^{-3}$ | 0.2428 | $0.1887 \cdot 10^{-3}$ | 0.2808 |
| $1.0867 \cdot 10^{-3}$ | 0.3007 | $0.6169 \cdot 10^{-3}$ | 0.3304 |
| $1.5499 \cdot 10^{-3}$ | 0.3445 | $1.1116 \cdot 10^{-3}$ | 0.3814 |
| $2.0907 \cdot 10^{-3}$ | 0.3966 | $1.4683 \cdot 10^{-3}$ | 0.4222 |
| $2.5697 \cdot 10^{-3}$ | 0.4443 | $1.8482 \cdot 10^{-3}$ | 0.4637 |
| $3.1585 \cdot 10^{-3}$ | 0.5026 | $2.3575 \cdot 10^{-3}$ | 0.5030 |
| $3.6748 \cdot 10^{-3}$ | 0.5396 | $2.7215 \cdot 10^{-3}$ | 0.5391 |
| $4.0262 \cdot 10^{-3}$ | 0.5708 | $3.0381 \cdot 10^{-3}$ | 0.5734 |
| $4.6228 \cdot 10^{-3}$ | 0.6281 | $3.3204 \cdot 10^{-3}$ | 0.6002 |
| $5.1390 \cdot 10^{-3}$ | 0.6619 | $3.7680 \cdot 10^{-3}$ | 0.6375 |
| | | $4.1346 \cdot 10^{-3}$ | 0.6729 |
| | | $4.7270 \cdot 10^{-3}$ | 0.7044 |
| | | $5.0716 \cdot 10^{-3}$ | 0.7370 |
| | | $5.3636 \cdot 10^{-3}$ | 0.7625 |
| | | $5.6369 \cdot 10^{-3}$ | 0.7835 |
| **Vertical HP** | | **Horizontal HP** | |
| $-3.4376 \cdot 10^{-3}$ | -0.2032 | $-3.2135 \cdot 10^{-3}$ | -0.3586 |
| $-2.8736 \cdot 10^{-3}$ | -0.1393 | $-3.1265 \cdot 10^{-3}$ | -0.3167 |
| $-2.4714 \cdot 10^{-3}$ | -0.0961 | $-2.9788 \cdot 10^{-3}$ | -0.2557 |
| $-1.9727 \cdot 10^{-3}$ | -0.0373 | $-2.9083 \cdot 10^{-3}$ | -0.2122 |
| $-1.4830 \cdot 10^{-3}$ | 0.0200 | $-2.6505 \cdot 10^{-3}$ | -0.1497 |
| $-0.8474 \cdot 10^{-3}$ | 0.0992 | $-2.2718 \cdot 10^{-3}$ | -0.0796 |
| $-0.2739 \cdot 10^{-3}$ | 0.1574 | $-1.9025 \cdot 10^{-3}$ | -0.0249 |
| $0.1471 \cdot 10^{-3}$ | 0.2122 | $-1.5760 \cdot 10^{-3}$ | 0.0340 |
| $0.6301 \cdot 10^{-3}$ | 0.2670 | $-1.0485 \cdot 10^{-3}$ | 0.1054 |
| $1.0334 \cdot 10^{-3}$ | 0.3130 | $-0.6864 \cdot 10^{-3}$ | 0.1611 |
| $1.5764 \cdot 10^{-3}$ | 0.3651 | $-0.2475 \cdot 10^{-3}$ | 0.2195 |
| $1.9552 \cdot 10^{-3}$ | 0.4088 | $0.2107 \cdot 10^{-3}$ | 0.2803 |
| $2.3358 \cdot 10^{-3}$ | 0.4448 | $0.6450 \cdot 10^{-3}$ | 0.3344 |
| $2.7650 \cdot 10^{-3}$ | 0.4894 | $1.0155 \cdot 10^{-3}$ | 0.3824 |
| $3.2047 \cdot 10^{-3}$ | 0.5392 | $1.4375 \cdot 10^{-3}$ | 0.4333 |
| $3.4400 \cdot 10^{-3}$ | 0.5546 | $1.8951 \cdot 10^{-3}$ | 0.4862 |
| $3.7520 \cdot 10^{-3}$ | 0.5776 | $2.3722 \cdot 10^{-3}$ | 0.5362 |
| $4.1204 \cdot 10^{-3}$ | 0.5963 | $2.7993 \cdot 10^{-3}$ | 0.5836 |
| $4.4242 \cdot 10^{-3}$ | 0.6089 | $3.2454 \cdot 10^{-3}$ | 0.6257 |
| $4.9387 \cdot 10^{-3}$ | 0.6300 | $3.6890 \cdot 10^{-3}$ | 0.6681 |
| $5.0420 \cdot 10^{-3}$ | 0.6438 | $4.0578 \cdot 10^{-3}$ | 0.7063 |
| | | $4.3775 \cdot 10^{-3}$ | 0.7371 |
| | | $4.6593 \cdot 10^{-3}$ | 0.7579 |

Table 6.5: Reference and measured positions in the vertical (left) and horizontal (right) planes for the low (top) and high (bottom) extracted PETS power test configurations in the installation with axis-oriented electrodes.

| Parameter | Measurement LP | Measurement HP | Theory | Simulation |
|---|---|---|---|---|
| **Vertical** | | | | |
| $S_V$ [m$^{-1}$] | 103.3 ± 1.8 | 103.0 ± 2.3 | 166.67 | 137.01 |
| $EOS_V$ [m] | $(-1.64 \pm 0.05) \cdot 10^{-3}$ | $(-1.74 \pm 0.07) \cdot 10^{-3}$ | 0.00 | 0.00 |
| $\sigma_V$ [m] | $164.25 \cdot 10^{-6}$ | $141.88 \cdot 10^{-6}$ | | |
| **Horizontal** | | | | |
| $S_H$ [m$^{-1}$] | 105.8 ± 2.1 | 134.8 ± 4.3 | 166.67 | 137.01 |
| $EOS_H$ [m] | $(-2.21 \pm 0.06) \cdot 10^{-3}$ | $(-1.49 \pm 0.08) \cdot 10^{-3}$ | 0.00 | 0.00 |
| $\sigma_H$ [m] | $85.22 \cdot 10^{-6}$ | $181.36 \cdot 10^{-6}$ | | |

Table 6.6: Measured linearity and sensitivity parameters of the prototype stripline BPM for both high and low power test configurations in the installation with axis-oriented electrodes.

The measured horizontal sensitivity, however, starts with a lower value than expected in the low extracted PETS power test configuration, 105.8 m$^{-1}$, becoming closer, 134.8 m$^{-1}$, to the simulated value of 137.01 m$^{-1}$ in the high extracted PETS power test configuration. The instability of the available beam in the low extracted PETS power configuration may have resulted in non-negligible differences between the test beams used for different positions, affecting also the measured positions by the reference BPMs 0850 and 0910.

For operational aspects, it is possible to increase these sensitivities in both low and high extracted PETS power test configurations by estimating the position as a polynomial function of the difference-over-sum ratio instead of a linear one. A fifth degree polynomial fit of the simulated curve for a stripline PU with axis-oriented electrodes (Figure 5.11) increases all sensitivity values in Table 6.6 by 30 m$^{-1}$. However, this does not eliminate the observed effects of the extracted PETS power increase in the horizontal sensitivity and provides a too high value for this parameter in the high extracted PETS power configuration.

Finally, a variation in the electrical offset was observed for the coordinate not being swept (Figure 6.16). In addition, for this coordinate in both the high- and low-power test configurations, a tilt was observed, of 5 mrad for the horizontal plane and 4 mrad for the vertical one.

## 6.3 Resolution

Following the sensitivity and linearity tests of the stripline BPM prototype with short-circuited electrodes, a preliminary resolution test was performed using Singular Value Decomposition (SVD) analysis. The SVD method decomposes the data, allowing to identify and separate systematic beam effects (modes) like, for instance, betatron motion, cavity phase/energy errors, RF jitter, etc. from uncorrelated statistical noise of the BPMs (BPM noise floor) and thus provide an estimate of the resolution of each BPM on the line. The use of this technique for the analysis of BPM data was first proposed in [70]. Further successful examples of its application can be found in [71] and [72].

The objective of this analysis is to estimate the resolution of the CLIC DB stripline BPM with short-circuited electrodes, based on shot-to-shot position data collected from all the 17 TBL BPMs. For this purpose, position data from 966 consecutive, synchronous

shots from a 3 A beam were acquired and analysed in the stripline BPM installation with axis-oriented electrodes. Table 6.7 shows the assigned number, location and type of all TBL BPMs considered in this study, including the stripline BPM prototype.

| BPM number | TBL location | BPM type |
|---|---|---|
| 1 | 0210 | Inductive |
| 2 | 0250 | Inductive |
| 3 | 0310 | Inductive |
| 4 | 0350 | Inductive |
| 5 | 0410 | Inductive |
| 6 | 0450 | Inductive |
| 7 | 0510 | Inductive |
| 8 | 0550 | Inductive |
| 9 | 0610 | Inductive |
| 10 | 0650 | Inductive |
| 11 | 0710 | Inductive |
| 12 | 0750 | Inductive |
| 13 | 0810 | Inductive |
| 14 | 0850 | Inductive |
| **15** | **0860** | **Stripline** |
| 16 | 0910 | Inductive |
| 17 | 0950 | Inductive |

Table 6.7: TBL BPM locations, type and assigned numbers for the SVD analysis.

The procedure starts by considering a $B$ matrix of dimensions $P \times M$, where $P$ is the number of shots and $M$ the number of BPMs, containing the position data from all TBL BPMs, having substracted their mean values per column (orbit). This matrix can be factorized in the form:

$$B = U \cdot S \cdot V^T \tag{6.9}$$

where:

$$B_{P\times M} = \begin{pmatrix} b_{11} & b_{12} & \cdots & b_{1M} \\ b_{21} & b_{22} & \cdots & b_{2M} \\ b_{31} & b_{32} & \cdots & b_{3M} \\ b_{41} & b_{42} & \cdots & b_{4M} \\ \vdots & \vdots & \vdots & \vdots \\ b_{P1} & b_{P2} & \cdots & b_{PM} \end{pmatrix} \qquad U_{P\times P} = \begin{pmatrix} u_{11} & u_{12} & \cdots & u_{1P} \\ u_{21} & u_{22} & \cdots & u_{2P} \\ \vdots & \vdots & \ddots & \vdots \\ u_{P1} & u_{P2} & \cdots & u_{PP} \end{pmatrix}$$

$$S_{P\times M} = \begin{pmatrix} s_{11} & 0 & \cdots & 0 \\ 0 & s_{22} & \cdots & 0 \\ 0 & 0 & \cdots & 0 \\ 0 & 0 & \cdots & s_{MM} \\ \vdots & \vdots & \vdots & \vdots \\ 0 & 0 & \cdots & 0 \end{pmatrix} \qquad V_{M\times M} = \begin{pmatrix} v_{11} & v_{12} & \cdots & v_{1M} \\ v_{21} & v_{22} & \cdots & v_{2M} \\ \vdots & \vdots & \ddots & \vdots \\ v_{M1} & v_{M2} & \cdots & v_{MM} \end{pmatrix} \tag{6.10}$$

$U$ is a $P \times P$ matrix containing the temporal eigenvectors and $V$ is a $M \times M$ matrix containig the spatial eigenvectors. Both are orthogonal matrices. $S$ is a $P \times M$ diagonal matrix containing non-negative values (eigenvalues or modes).

The diagonal elements of S, $s_{ii}, 1 \leq i \leq M, i \in \mathbb{N}$, normalized by $\sqrt{MP}$, give the correlation level between the U and V matrices: the larger their value, the higher the correlation. They are shown in Figure 6.17 for both the horizontal and the vertical planes. It is possible to observe that the first eight elements of $S$ have large values, accounting for correlated beam motion, while elements 9 to 17 are due to the uncorrelated BPM noise floor.

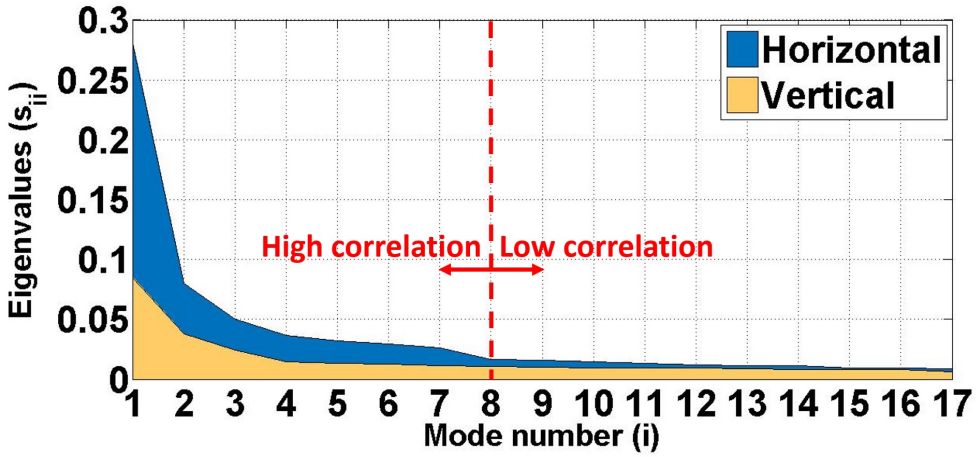


Figure 6.17: Normalized diagonal elements $s_{ii}$ of the $S$ matrix. The first eight elements define the high correlation region due to beam motion, while the elements 9 to 17 belong to the low correlation region due to the BPM noise floor

Setting modes 1 to 8 to zero, we obtain a new diagonal matrix $S'$, from which it is possible to reconstruct the data matrix $B'$ where only uncorrelated BPM noise floor is present:

$$B' = U \cdot S' \cdot V^T \tag{6.11}$$

The standard deviation values $\sigma_i, i \in [1, 17], i \in \mathbb{N}$, of the columns of $B'$ provide the resolution for all 17 BPMs. The result is plotted in Figure 6.18.

The preliminary estimated resolution values for the stripline prototype with short-circuited electrodes, BPM#15, are 11 $\mu$m in the horizontal plane and 7.4 $\mu$m in the vertical plane.

## 6.4 Conclusions

In the linearity and sensitivity tests of the installation with 45°-rotated electrodes, the measured sensitivities for each plane (Table 6.3) experience a ±4% variation upon the increase of the extracted PETS RF power from 6 to 60 MW. The measured horizontal sensitivity values (98.1 $m^{-1}$ and 94.2 $m^{-1}$ for 6 and 60 MW, respectively) remain close to the simulated value of 101.8 $m^{-1}$, while the vertical sensitivity was found systematically lower (72.4 $m^{-1}$ and 75.3 $m^{-1}$ for 6 and 60 MW, respectively). The same effect has been observed for the vertical sensitivity for both low and high (2.4 and 27 MW) extracted

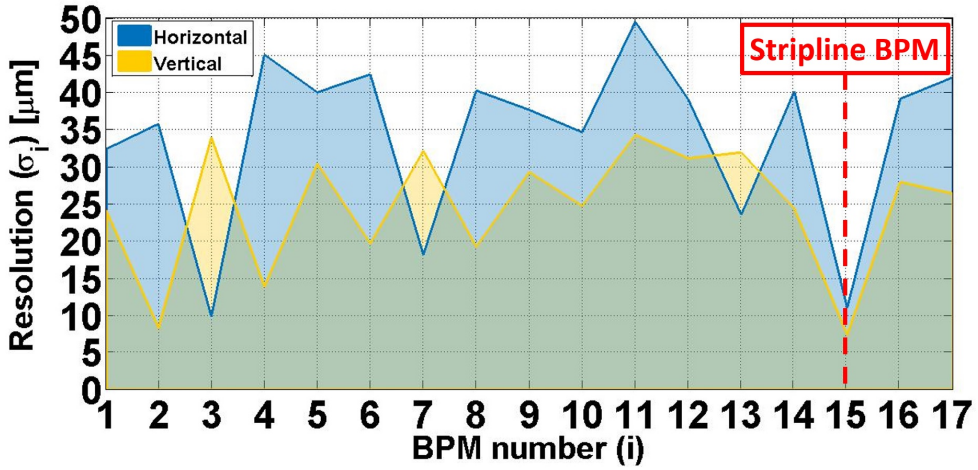


Figure 6.18: Standard deviation per columns of the $B'$ matrix, indicating the resolution of each BPM in TBL.

PETS power test configurations for the installation with axis-oriented electrodes. The non-linear effects can be mitigated by correcting the position characteristic of the pick-up using a higher-order polynomial or a look-up table.

The acquisition electronics have performed satisfactorily during the beam tests at CTF3, providing the expected output signals and levels and the foreseen radiation-hardness. In the presence of high power RF interferences from the PETS, a small effect in the offset was observed, which may be caused by insufficient suppression of 12 GHz CLIC RF fields. This problem can be addressed by the development of a new stripline prototype with improved notch filter effect at 12 GHz.

During the beam studies of the first prototype stripline BPM, the position data of all the TBL BPMs was analyzed applying a Singular Value Decomposition (SVD) method. In this way it was possible to separate the correlated beam motion effects from the uncorrelated BPM noise, finding an upper resolution boundary of 11 $\mu$m for the horizontal plane and 7.4 $\mu$m for the vertical one (Figure 6.18). These values already improve the average inductive BPM resolution boundaries of 35.5 $\mu$m for the horizontal plane and 25.7 $\mu$m for the vertical plane. Further improvements can be expected, however, at higher beam currents in the TBL line of CTF3.

# Chapter 7

# Conclusions

This thesis has covered the design, development, laboratory characterization and beam tests of the first prototype stripline BPM for the CLIC Drive Beam decelerator. The main constraints have been set by the need for a simple and economic design, given the large amount of units required for the full-scale CLIC collider project, and the requirement to suppress the RF interference caused by the PETS at 12 GHz and to provide sufficient spatial and temporal resolution.

Among the BPM technologies revised in Chapter 2, the only one to present a suitable frequency response for this purpose is the stripline. By choosing an appropriate length of the electrodes, one of its periodic notches can be tuned to 12 GHz to filter out the PETS interference. The original design of such a pick-up was described in Chapter 3. A post-design study revealed additional problems, such as the modification of the intended frequency response due to the inclusion of the SiC ring as damping material, and some inherent geometry issues: the lobe distortion of the stripline pick-up frequency response increasing with the electrode angular coverage and unwanted resonances that appear when dimensions of electrode length and vacuum pipe aperture become similar. This study suggests that further stripline pick-up developments should have narrower and longer electrodes. A decision was made, however, to test this design both in laboratory and with beam.

Chapter 4 described the design of a suitable electronic acquisition system to process the pick-up signals fulfilling the requirements of the project in terms of resolution (2 $\mu$m), accuracy (20 $\mu$m) and time resolution (10 ns). Due to the high number of units to be produced, the number of analog electronic components has been minimized. As the designed signal processing scheme is based on charge integration, it can be adapted to different stripline pick-ups by simply modifying the attenuator settings according to the required output signal levels.

The laboratory characterization tests of the first prototype stripline BPM, both in the low and high frequency ranges, with thin wire and coaxial waveguide test bench, respectively, have been described in Chapter 5. The measured horizontal and vertical sensitivity values in the characterization tests with a thin wire (Table 5.2), both around 115.2 $m^{-1}$, are closer to the simulated value (137 $m^{-1}$) than to the theoretically expected one using the linear approximation derived in Chapter 4 (166.67 $m^{-1}$). Charge accumulation and impedance mismatches in the measurement setup are the most likely causes of this difference in sensitivity values. The measured filtering properties of the pick-up at 12 GHz in the coaxial test bench are not as they were expected from the basic theory, and the

rejection around this frequency is only about 4 dB (Figure 5.22). This problem can be addressed by the development of a new stripline prototype with improved notch filter effect at 12 GHz, using the recommendations of the study performed in Chapter 3: longer and narrower electrodes. Additionally, using terminated electrodes instead of downstream short-circuited ones is expected to increase the tunability of the stripline frequency response notches to a given frequency, and to add a calibration functionality via the downstream port.

The influence of these observations on the performance of the BPM was further studied during the tests with beam at CTF3, described in Chapter 6. In the linearity and sensitivity tests of the installation with 45° rotated electrodes, the measured sensitivities for each plane (Table 6.3) experience a ±4% variation upon the increase of the extracted PETS RF power from 6 to 60 MW. The measured horizontal sensitivity values (98.1 $m^{-1}$ and 94.2 $m^{-1}$ for 6 and 60 MW, respectively) remain close to the simulated value of 101.8 $m^{-1}$, while the vertical sensitivity was found systematically lower (72.4 $m^{-1}$ and 75.3 $m^{-1}$ for 6 and 60 MW, respectively). The same effect has been observed for the vertical sensitivity for both low and high (2.4 and 27 MW) extracted PETS power test configurations for the installation with axis-oriented electrodes. The non-linear effects can be mitigated by correcting the position characteristic of the pick-up using a higher-order polynomial or a look-up table.

During the beam studies of the first prototype stripline BPM, the position data of all the TBL BPMs was analyzed applying a Singular Value Decomposition (SVD) method. In this way it was possible to separate the correlated beam motion effects from the uncorrelated BPM noise, finding an upper resolution boundary of 11 $\mu$m for the horizontal plane and 7.4 $\mu$m for the vertical one (Figure 6.18). An improvement can be expected, however, at higher beam currents in the TBL line of CTF3.

# Bibliography


[1] The European Strategy for Particle Physics, CERN-Council-S/106, 2013.

[2] International Linear Collider Reference Design Report (RDR). ILC Global Design Effort and World Wide Study Groups. ILC-REPORT-2007-1, https://www.linearcollider.org/ILC/Publications/Reference-Design-Report, 2007.

[3] International Linear Collider Technical Design Report (TDR), http://www.linearcollider.org/ILC/Publications/Technical-Design-Report, 2013.

[4] CLIC Conceptual Design Report (CDR), http://project-clic-cdr.web.cern.ch/project-clic-cdr/CDR_Volume1.pdf, 2012.

[5] M. Jonker, private communications.

[6] G. Geschonke, A. Ghigo et al., *CTF3 Design Report*, CERN/PS 2002-008 (RF), LNF-02/008, 2002, CTF3 Note 047, 2002.

[7] J.J. García-Garrigós, *Development of the Beam Position Monitors for the Diagnostics of the Test Beam Line in the CTF3 at CERN*, PhD. Thesis, Universidad Politécnica de Valencia, Valencia, Spain, 2013.

[8] S. Döbert, D. Schulte, I. Syratchev, *Status Report of the CTF3 Test Beam Line*, CTF3 Note 076, 2006.

[9] P. Forck, *Lecture Notes on Beam Instrumentation and Diagnostics*. Gesellschaft für Schwerionenforschung (GSI), Joint Universities Accelerator School (JUAS), Archamps, France, 2011.

[10] P. Strehl, *Beam Instrumentation and Diagnostics*, Springer-Verlag, Berlin, Germany, 2006.

[11] A. Hofmann, *Dynamics of Beam Diagnostics*, Beam Diagnostics for Accelerators, Proceedings of CERN Accelerator School (CAS), CERN-2009-005, Dourdan, France, 2009, pp. 65-139.

[12] I.S. Grant and W.R. Phillips, *Electromagnetism*, 2nd Ed., John Wiley & Sons, Chichester, UK, 2013, pp. 464-469.

[13] M. Wendt, *Overview of Recent Trends and Developments for BPM Systems*, DIPAC2011, Hamburg, Germany, 2011.

[14] P. Forck, P. Kowina, D. Liakin, *Beam Position Monitors*, Beam Diagnostics for Accelerators, Proceedings of CERN Accelerator School (CAS), CERN-2009-005, Dourdan, France, 2009, pp. 187-228.

[15] R.E. Shafer, *Beam Position Monitoring*, AIP Conference Proceedings, Vol. 212, 1989.

[16] P. Kowina, W. Kaufmann, J. Schölles, *Optimisation of Linear-Cut Beam Position Monitors Using Finite Element Methods*, DIPAC'07, Venice, Italy, 2007.

[17] P. Kowina, P. Forck, W. Kaufmann, P. Moritz, F. Wolfheimer, T. Weiland, *FEM Simulations - A Powerful Tool for BPM Design*, DIPAC'09, Basel, Switzerland, 2009.

[18] F. Marcellini, M. Serio, M. Zobov, *DaΦne Broad-Band Button Electrodes*, INFN-LNF CD-6, Frascati, Italy, 2006.

[19] C. Boccard, *Design Choices for the Cold LHC BPMs*, CARE-N3-HHH-ABI Workshop, Lüneburg, Germany, 2006.

[20] J. Lund-Nielsen, N. Baboi, W. Riesch, *Button Beam Position Monitors for FLASH*, DIPAC'07, Venice, Italy, 2007.

[21] D. Nölle, N. Baboi, K. Knaack, D. Lipka, J. Lund-Nielsen, N. Mildner, R. Neumann, F. Schmidt-Föhre, M. Siemens, T. Traber, S. Vilcins, *BPMs for the XFEL Cryo Module*, DIPAC'07, Venice, Italy, 2007.

[22] A. Lunin, N. Eddy, T.N. Khabiboulline, V.A. Lebedev, V.P. Yakovlev, *Development of a Low-Beta Button BPM for PXIE Project*, IBIC'13, Oxford, UK, 2013.

[23] W.X. Cheng, B. Bacha, B.N. Kosciuk, S. Krinsky, O. Singh, *Performance of NSLS2 Button BPMs*, IBIC'13, Oxford, UK, 2013.

[24] H. Hassanzadegan, A. Jansson, D. Lipka, C.A. Thomas, M. Werner, A. Young, *System Overview and Current Status of the ESS Beam Position Monitors*, IPAC'14, Dresden, Germany, 2014.

[25] D.M. Pozar, *Microwave Engineering*, John Wiley & Sons, Hoboken, USA, 2012.

[26] C. Magne, M. Wendt, *Beam Position Monitors for the TESLA Accelerator Complex*, Deutsches Elektronen-Synchrotron (DESY), 2000.

[27] A. Benot-Morell, J.M. Nappa, S.R. Smith, L. Søby, J. Tassan-Viol, S. Vilalte, M. Wendt, *Design and Characterization of a Prototype Stripline Beam Position Monitor for the CLIC Drive Beam*, IBIC'12, Tsukuba, Japan, 2012.

[28] S. Varnasseri, I. Arredondo, D. Belver, F.J. Bermejo, V. Etxebarria, J. Feuchtwanger, N. Garmendia, P.J. González, J. Jugo, L. Muguira, J. Portilla, *Design and Fabrication of the Stripline BPM at ESS-Bilbao*, IBIC'12, Tsukuba, Japan, 2012.

[29] T. Suwada, *Signal Transmission Characteristics in Stripline-Type Beam Position Monitor*, IBIC'12, Tsukuba, Japan, 2012.

[30] A. Benot-Morell, A. Faus-Golfe, J.M. Nappa, S.R. Smith, L. Søby, S. Vilalte, M. Wendt, *Status of the Stripline Beam Position Monitor Development for the CLIC Drive Beam*, IBIC'13, Oxford, UK, 2013.

[31] S. De Santis, M.J. Chin, D. Filippetto, W.E. Norum, Z. Paret, G.J. Portmann, F. Sannibale, R.P. Wells, *Design of the Stripline BPM for the Advanced Photoinjector Experiment*, IBIC'13, Oxford, UK, 2013.

[32] M. Gasior, *A Current Mode Inductive Pick-Up for Beam Position and Current Measurement*, DIPAC'05, Lyon, France, 2005.

[33] S. Walston et al., *Performance of a High Resolution Cavity Beam Position Monitor System*, Stanford Linear Accelerator Center (SLAC) Report No. SLAC-PUB-12492, 2007.

[34] M. Wendt, *Cold Cavity BPM R&D for the ILC*, CARE-N3-HHH-ABI Workshop, Lüneburg, Germany, 2006.

[35] F.J. Cullinan, D. Bastard, S.T. Boogert, E. Calvo, N. Chritin, F. Guillot-Vignot, N.Y. Joshi, T. Lefèvre, A. Lunin, A. Lyapin, S. Smith, L. Søby, M. Wendt, V.P. Yakovlev, *A Prototype Cavity Beam Position Monitor for the CLIC Main Beam*, IBIC'12, Tsukuba, Japan, 2012.

[36] J.R. Towler, S.T. Boogert, F.J. Cullinan, T. Lefèvre, A. Lyapin, L. Søby, M. Wendt, *Technologies and R&D for a High Resolution Cavity BPM for the CLIC Main Beam*, IBIC'13, Oxford, UK, 2013.

[37] S.T. Boogert, F.J. Cullinan, Y.I. Kim, A. Lyapin, J. Snuverink, T. Tauchi, N. Terunuma, J. Urakawa, G.R. White, *Cavity Beam Position Monitor System for ATF2*, IBIC'13, Oxford, UK, 2013.

[38] A. Lunin, G. Romanov, N. Solyak, M. Wendt, *Design of a Submicron Resolution Cavity BPM for the ILC Main Linac*, DIPAC'07, Venice, Italy, 2007.

[39] S.R. Smith, A. Cappelletti, D. Gudkov, L. Søby, I. Syratchev, *CLIC Drive Beam Position Monitor*, DIPAC'11, Hamburg, Germany, 2011.

[40] A. Benot-Morell, A. Faus-Golfe, J.J. García-Garrigós, J.M. Nappa, L. Søby, J. Tassan-Viol, S. Vilalte, *Characterization Tests of a Stripline Beam Position Monitor for the CLIC Drive Beam*, IPAC'12, New Orleans, USA, 2012.

[41] M. Wendt, private communications.

[42] R. E. Collin, *Field Theory of Guided Waves*, 2nd Ed., Wiley-IEEE Press, New York, USA, 1991, pp. 247-249.

[43] CST Studio Suite®, `https://www.cst.com/Products/CSTS2`.

[44] R.M. Jones, *Higher-Order Mode (HOM) Mitigation*. University of Manchester-Cockroft Institute, UK, CERN Accelerator School (CAS) 2010 Lecture Series "RF for Accelerators", Ebeltoft, Denmark, 2010.

[45] P.B. Wilson, *Introduction to Wakefields and Wake Potentials*, Stanford Linear Accelerator Center (SLAC) Report No. SLAC-PUB-4547, 1987.

[46] W. Bruns, *The GdfidL® Electromagnetic Field Simulator*, `http://www.gdfidl.de`.

[47] Ceramtec®, *Coaxial Connectors Catalog*, http://shop.ceramtec.us/pdf/hermetic/Coaxial_Connectors.pdf

[48] Mersen-Boostec®, *Mersen Boostec Silicon Carbide*, https://www.mersen.com/uploads/tx_mersen/21-silicon-carbide-sic-boostec-mersen.pdf

[49] P. Moreira et al., *The GBT Project*, Topical Workshop on Electronics for Particle Physics, Paris, France, 21 - 25 Sep 2009, pp.342-346, 2009.

[50] S. Mallows, T. Otto. *Estimates of Radiation Levels in the Main Linac Tunnel and Beam Dump Caverns for the CLIC Design Study*, $10^{th}$ Meeting of the Task-Force on Shielding Aspects of Accelerators, Targets and Irradiation Facilities, SATIF'10, Geneva, Switzerland, 2010.

[51] Altera®, *High Speed Mezzanine Card (HSMC) Specification*, http://www.altera.com/literature/ds/hsmc_spec.pdf, 2009.

[52] C. Pearson, *High-Speed, Analog-to-Digital Converter Basics*, Texas Instruments® Application Report SLAA510, http://www.ti.com/lit/an/slaa510/slaa510.pdf, 2011.

[53] Linear Technology®, *LTC2175-14/LTC2174-14/LTC2173-14 Datasheet*, http://cds.linear.com/docs/en/datasheet/21754314fa.pdf, 2009.

[54] Linear Technology®, *LTC6406 Datasheet*, http://cds.linear.com/docs/en/datasheet/6406fc.pdf, 2007

[55] J. Tan, M. Sordet, L. Søby, *Beam Position Monitor System for the CERN LINAC4*, DIPAC'11, Hamburg, Germany, 2011.

[56] F. Guillot-Vignot, private communications.

[57] Mitutoyo®, *ST422 Linear Scale Datasheet*, http://www.mitutoyo.com/wp-content/uploads/2013/11/E13005_LinerScaleSystem.pdf, 2013.

[58] J. Tassan-Viol, private communications.

[59] Aim & Thurlby Thandar Instruments®, *TTI TSX-P Series Specifications*, http://www.tti-test.com/products-tti/text-pages/psu-tsxp-series.htm, 2015.

[60] ELC®, *ELC AL-936N Datasheet*, http://elc.fr/media/al936n_gb__058803200_1124_23062014.pdf, 2011.

[61] Tektronix®, *Arbitrary Function Generators AFG 3011 / 3021B / 3022B / 3101 / 3102 / 3251 / 3252 Datasheet*, http://www.tek.com/sites/tek.com/files/media/media/resources/AFG3000_Series_Arbitrary-Function_Generators_Datasheet_76W-18656-5.pdf, 2012.

[62] SRS - Stanford Research Systems®, *CG635 Synthesized Clock Generator Datasheet*, http://www.thinksrs.com/downloads/PDFs/Catalog/CG635c.pdf, 2012.

[63] J.M. Nappa, private communications.

[64] Omron®, *EE-SX1107 Datasheet*, https://www.components.omron.com/components/web/pdflib.nsf/0/C2BE87D3C3F80D7E85257201007DD5E7/\$file/EE_SX1107_1010.pdf, 2010.

[65] Mitutoyo®, *ABSOLUTE Digimatic Indicator ID-C Series 543-Standard Type*, http://ecatalog.mitutoyo.com/ABSOLUTE-Digimatic-Indicator-ID-C-Series-543-Standard-Type-C1198.aspx

[66] J.J. García-Garrigós, C. Blanch-Gutierrez, J.V. Civera-Navarrete, A. Faus-Golfe, B. Gimeno-Martínez, *High Frequency Measurements of the Beam Position Monitors for the TBL Line of the CTF3 at CERN*, DIPAC'11, Hamburg, Germany, 2011.

[67] Keysight Technologies®, *Network Analyzer Basics*, http://www.keysight.com/upload/cmc_upload/All/BTB_Network_2005-1.pdf?&cc=CH&lc=ger, 2011.

[68] J.P. Sikora, R.M. Schwartz, K.G. Sonnad, *TE Wave Measurement and Modeling*, ECLOUD'12, Biodola, Italy, 2012.

[69] Keysight Technologies®, *E5071C ENA Network Analyzer Datasheet*, http://literature.cdn.keysight.com/litweb/pdf/5989-5479EN.pdf, 2013.

[70] C.X. Wang, *Model Independent Analysis of Beam Centroid Dynamics in Accelerators*, PhD. Thesis, Stanford University, USA, 1999.

[71] C.X. Wang, M. Borland, K.J. Kim, V. Sajaev, *BPM System Evaluation Using Model-Independent Analysis*, PAC'01, Chicago, USA, 2001.

[72] J. Tan, M. Ludwig, M. Sordet, L. Søby, M. Wendt, *Commissioning of the CERN LINAC4 BPM System With 50 MeV Proton Beams*, IPAC'13, Shanghai, China, 2013.